NOVEL MAGNETIC RESONANCE PROBES

by

Zohreh Hashami

THE UNIVERSITY OF TEXAS AT DALLAS

APPROVED BY SUPERVISORY COMMITTEE:

Zoltan Kovacs, Co-Chair

John W. Sibert, Co-Chair

Warren J. Goux

Paul Pantano

To my loving family

NOVEL MAGNETIC RESONANCE PROBES

by

Zohreh Hashami, BS, MS

DISSERTATION

Presented to the Faculty of

The University of Texas at Dallas

in Partial Fulfillment

of the Requirements

for the Degree of

DOCTOR OF PHILOSOPHY IN

CHEMISTRY

THE UNIVERSITY OF TEXAS AT DALLAS

May 2018

ACKNOWLEDGMENTS

I would like to acknowledge my research advisor, Dr. Zoltan Kovacs, for his constant support, training and encouragement during my research. Without his help I could not have made it this far. I would like to thank Dr. John W. Sibert, my Co-Chair, for all his support and advice. Thanks to my committee members, Dr. Paul Pantano and Dr. Warren Goux, for their helpful suggestions and advice. It has been an honor to have you all on my committee.

I also thank Dr. Andre Martins, for sharing his NIR lanthanides expertise with me and for his enlightening discussions and advice. Also, I want to thank Dr. Alex Funk and Dr. Veronica Clavijo Jordan for their help with MR imaging. Thanks to Dr. Charlie Khemtong and Nesmine Maptue for their assistance with hyperpolarization experiments.

I would also like to acknowledge our collaborators Dr. Svetlana Eliseeva and Stephane Petoud at the Centre de Biophysique Moléculaire, France for their contribution involving the optical characterization of the lanthanide complexes. A special thank you goes out to Dr. Dean Sherry for giving me the opportunity to work the AIRC.

Most importantly, I would like to thank my family for the encouragement, love and constant support.

"*So that in all things God may be glorified*."

January 2018

NOVEL MAGNETIC RESONANCE PROBES

Zohreh Hashami, PhD
The University of Texas at Dallas, 2018

Supervising Professors: Zoltan Kovacs, Co-Chair
John W. Sibert, Co-Chair

The goal of my first project was the synthesis and characterization of novel DOTA (1,4,7,10-tetraazacyclododecane-1,4,7,10-tetraacetic acid) based ligands with one and two chromophoric tropone coordinating sidearms for the construction of lanthanide based magnetic resonance/optical imaging probes. Lanthanide ions have nearly identical coordination chemistry properties and therefore, the same ligand can be applied to the entire lanthanide series. The development of dual magnetic resonance/optical imaging probes is an exciting current trend in the research area of lanthanide based imaging agents because these probes could combine the high spatial resolution of MRI with the high sensitivity of optical detection. The challenge in the design of these agents is that the requirements for an efficient MR agent (presence of an inner sphere water molecule) are seemingly incompatible with those of optical agents (absence of inner sphere water molecules). Three ligands were synthesized: 1,4,7,10-tetraazacyclododecane-1,4,7-tris(acetic acid)-10-(2-tropone) (**1**), 1,4,7,10-tetraazacyclododecane-1,7-bis(acetic acid)-4,10-bis(2-tropone), (**2**) and 1,4,7,10-tetraazacyclododecane-1,4,7-tris(aceticacid)-10-[2-(4-isopropyl)-tropone) (**3**) . Ln^{3+}complexes of these ligands were found to have one inner-sphere

water molecule. The r_1 relaxivity of Gd^{3+} complexes was found to be similar to that of the commercial Gd-based MRI agents. Relaxivity measurements in the presence of human serum albumin (HSA) showed that the Gd^{3+} complexes weakly bind to HSA. Variable temperature ^{17}O NMR measurements revealed that the neutral O-donor atom of the tropone moiety slows down the water exchange rate of the Gd^{3+} complexes compared to that for GdDOTA. *In vivo* MR imaging experiments with Gd**1** and Gd**3** in mice revealed that the agents were excreted by the kidneys and the liver. The complexes did not show any toxicity at the injected doses (0.1 mmol/kg). The photophysical properties of the Gd^{3+}, Nd^{3+} and Yb^{3+} complexes of ligand **1** and **2** were studied by recording the absorption, excitation and emission spectra. The Nd^{3+} and Yb^{3+} complexes were found to exhibit bright NIR emission even in aqueous solutions, which indicates that the tropone unit is an efficient sensitizer for these Ln^{3+}ions. The favorable relaxivity of the Gd^{3+} complexes and the bright NIR luminescence of the Nd^{3+} and Yb^{3+} complexes demonstrate that the tropone chromophore combined with the DOTA framework offers a useful platform for the design of lanthanide-based dual MR/optical imaging agents for *in vivo* applications.

My second project is related to hyperpolarized ^{13}C magnetic resonance spectroscopy/imaging. The goal of this project was the synthesis of monoethyl [4-^{13}C]-oxaloacetate and its evaluation in dissolution dynamic nuclear polarization NMR experiments as a metabolic probe. Monoethyl [4-^{13}C]-oxaloacetate disodium salt was successfully synthesized. Perfused liver experiments revealed that the compound was taken up by the liver, and metabolized to maleate, citrate and aspartate. Dynamic nuclear polarization to enhance the ^{13}C spin polarization was successfully performed, however, the T_1 relaxation time of the ^{13}C label at the C4 position was very short (about 14 s), which precluded its *in vivo* application as a hyperpolarized ^{13}C metabolic probe.

TABLE OF CONTENTS

CHAPTER 3 HYPERPOLARIZED ^{13}C LABELED OXALOACETATE DERIVATIVES AS POTENTIAL MR PROBE FOR METABOLIS 76

CURRICULUM VITAE

LIST OF FIGURES

LIST OF TABLES

LIST OF SCHEMES

CHAPTER 1

INTRODUCTION

In this introductory chapter a brief overview of the basic principles of nuclear magnetic resonance (NMR) and magnetic resonance imaging (MRI) is given to aid further discussions. Spin is an intrinsic property of all particles. According to the classic picture, spin is associated with the intrinsic spin of the particle. The intrinsic spin is related to an intrinsic angular momentum ($\vec{\mu} = \gamma \vec{J}$). The magnitude of magnetic momentum μ is directly proportional to the gyromagnetic ratio γ and its spin angular momentum J which can be define in a terms of dimensionless spin I (J= $\hbar$I).

$$\mu = \gamma\hbar I \qquad (1.1)$$

where $\hbar$ is the reduced Plank's constant (h/2π), (6.626×10^{-34} Js) and γ is gyromagnetic ratio. Spin is quantized, and therefore, it can have values I= 0,1/2, 3/2,… In the absence of an external magnetic field, degenerate spins occupy the same energy level. However, in the presence of an external B_0 magnetic field the degeneracy is broken giving rise to (2I+1) energy levels varying from –I to +I. This phenomenon known as the Zeeman effect. For a spin ½ nucleus I_z = -1/2, +1/2. Thus, in the presence of an external B_0 magnetic field, the Zeeman splitting gives rise to two energy levels ($E_{1,2} = \pm\frac{1}{2}\mu B_0$).[1] Since energy is a scalar quantity, it is defined by the dot or scalar product of the magnetic moment and the B_0 field,

$$\text{Energy} = \mu\cdot B_0 = \gamma\hbar I\, B_0 \qquad (1.2)$$

where (I =$I_x + I_y + I_z$) and since there are no x and y components, the energy can be written as

$$\text{Energy} = \gamma\hbar I_z\, B_0 \qquad (1.3)$$

The magnetic energy is highest when the magnetic moment is opposite to the B_0 field. The difference between the two levels is then given as:

$$\Delta E = E_2 - E_1 = \tfrac{1}{2}\gamma\hbar B_0 - (-\tfrac{1}{2}\gamma\hbar B_0) = \gamma\hbar B_0 \qquad (1.4)$$

where γ is the gyromagnetic ratio. This energy difference corresponds to the energy of a photon with frequency ν:

$$\gamma\hbar B_0 = h\nu = \hbar 2\pi\nu = \hbar\omega \qquad (1.5)$$

from this, the basic equation of nuclear magnetic resonance can be written as:

$$\omega = \gamma B_0 \qquad (1.6)$$

where ω is the resonance or Larmor frequency. According to the classical description, B_0 exerts a torque on the μ magnetic moment ($\mu \times B_0$) and ω is the angular frequency by which the magnetic moment precesses around the B_0 external magnetic field (Figure 1.1). Thus, the precession frequency of a nucleus is proportional to the strength of the magnetic field.

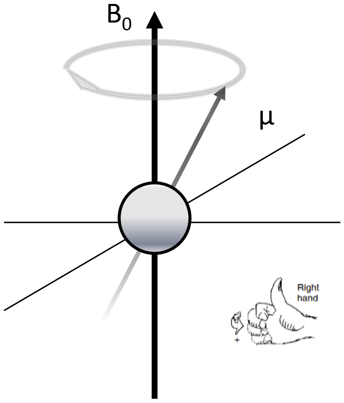

Figure 1.1. The Larmor precession. The direction of the precession is determined by the right hand rule ($\omega = -\gamma B_0$).

The phenomenon of nuclear magnetic resonance (NMR) was observed for the first time by Purcell and Bloch in 1945.[2,3] Experimentally, NMR involves the alignment of nuclear spins in an external magnetic field (B_0) followed by the perturbation of the spin ensemble by a B_1 rotating magnetic field (radiofrequency pulse) perpendicular to B_0 .The B_1 field is generated by a radiofrequency coil positioned in the xy plane and an electric signal is detected by the same coil (receiver coil) in the same direction. In the absence of external magnetic field, all nuclear spins are randomly oriented and no net magnetization will be observed in the sample. In presence of an external magnetic field (B_0), the ensemble of nuclear spins gives rise to a bulk magnetization (M_z) in the sample parallel to the external magnetic field. The B_1 magnetic field (radiofrequency pulse) applied perpendicular to the B_0 field rotates the M_z magnetization towards the xy plane when its frequency matches the Larmor frequency. This process generates a rotating M_{xy} component that induces a current in the receiver coil (free induction decay). The degree by which the magnetization is tipped towards the xy plane depends on the duration of B_1. A 90° radiofrequency pulse will tip the magnetization entirely into the xy plane ($M_z = 0$) .When B_1 is turned off, the magnetization returns to its equilibrium state in B_0 field. The time constant characterizing the return of M_z component to its equilibrium value is called the spin-lattice or longitudinal (T_1) relaxation time. This process relies on energy exchange between the nuclear spin system and its environment (lattice) hence the name spin-lattice relaxation. The inverse of T_1 is the relaxation rate (R_1). After applying the radiofrequency pulse, all nuclear spins will precess in phase in the xy plane.

However, due to spin-spin interactions there are small differences in Larmor frequency of the spins and they will precess individually with slightly different angular velocity in the *xy* plane. This causes the loss of their phase coherency over time. This process is known as spin-

spin or transverse relaxation and it is characterized by the transverse relaxation time (T_2). There is no energy loss during dephasing.

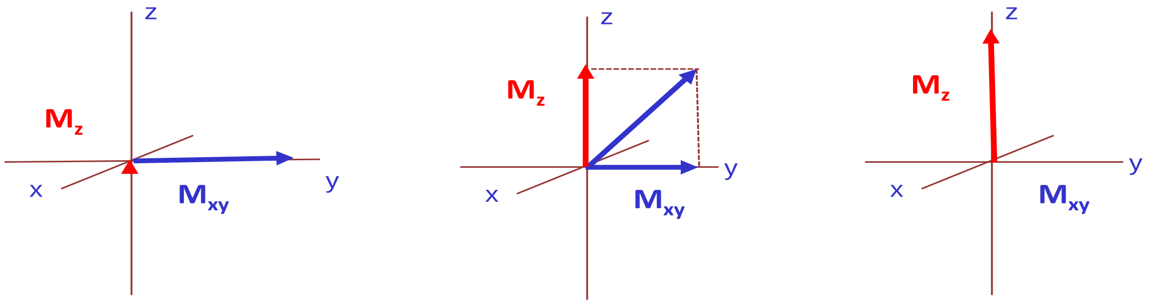

After a 90° pulse

T_1 relaxation

$$M_z = M_0(1-e^{-t/T1})$$

Figure 1.2. The spin-lattice or longitudinal (T_1) relaxation time.

Local field inhomogeneity also significantly contributes to dephasing and the measured relaxation time T_2^* is usually much shorter than T_2. It should be mentioned that the electric signal (free induction decay, FID) generated by the M_{xy} component of magnetization decays according to the T_2^*. An interesting feature of dephasing is that it can be reversed multiple times before complete decay by applying a 180 degree pulse, which will lead to refocusing (spin-echo). This has special importance for imaging.[4] NMR forms the basis of magnetic resonance imaging (MRI), which has become one of the most important medical imaging modalities.[1,5] Magnetic resonance imaging (MRI) is a non-invasive diagnostic tool widely used in clinical medicine that can provide high-resolution images of soft tissues. A conventional MR image is a map of ^1H

NMR signal intensities, which primarily depends on the proton density, the longitudinal (spin-lattice or T_1) and transversal (spin-spin or T_2) relaxation times in tissues.

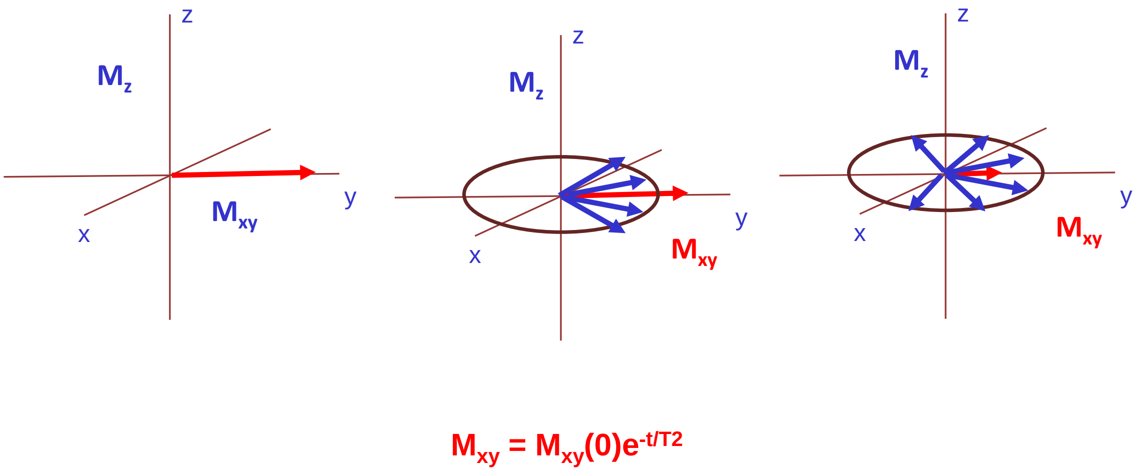

Figure 1.3. The spin-spin or transverse relaxation time (T_2).

Image contrast originates from differences in these parameters as shown in the following equation:

$$\text{Signal intensity} \sim \text{p}\ (1 - e^{-T_R/T_1})\ e^{-T_E/T_2} \qquad (1.7)$$

Where p is proton density, T_1 and T_2 are the longitudinal and transverse relaxation times respectively, T_R is the repetition time (the interval between two successive excitations of the same slice) and T_E is the echo time (the interval between application of the initial excitation radiofrequency pulse and the maximum of the spin echo). Very briefly, short T_1 regions have high intensity (bright) when short T_R and short T_E is used (T_1 weighted image), while short T_2 regions have low intensity (dark) when long T_R and long T_E is used (T_2 weighted image). About 3/4 of the human body consist of water; therefore, the major contribution to the MRI signal comes from water protons in tissues. Image contrast arises from variations of water density and proton relaxation times in tissues. There are large differences in relaxation times between different tissues and more importantly, between normal and diseased tissues. It has been known since 1971 that malignant tissues have longer T_1 and T_2 than normal tissues.[4] Any agent or process that affects the p, T_1 and T_2 will also alter image contrast. For example, paramagnetic species such as metal ions and free radicals enhance contrast by shortening the relaxation times.[6] To obtain 3D MRI images that are used in the clinical practice, MR scanners are equipped with gradient coils that generate magnetic field gradients in x,y and z directions. The gradient fields superimpose on the B_0 field and are applied to change the frequency and phase of the nuclear spins. The gradient along the z-axis is used for slice selection. The other two gradients separate signals within the slice, by frequency encoding along the x-axis and phase encoding along the y- axis.[1]

The Hahn spin echo sequence forms the basis for the most commonly used MRI pulse sequences. The spin system is exited with a 90° rf pulse and then one or more 180° pulses are applied to refocus the spins to achieve spin echoes. These refocus the spins and recover transverse magnetization. For slice selection, the z-gradiens (G_z) are turned on for the duration of the rf pulses. Before readout (signal acquisition), the Gy gradients are turned on to generate phase shifts (phase encoding). The G_x gradients are applied during acquisition to achieve frequency encoding by varying the resonance frequency in the direction of the frequency-encoding gradient G_x. The spin coherence can also be reformed by gradient echo, in this case, one rf pulse is applied followed by gradient reversal, which refocuses the spins (gradient echo).The main advantage of gradient echo (GRE) over spin echo (SE) sequences is that the use of only one rf pulse leads to shorter TE echo time, which facilitates faster signal acquisition.

However, conventional NMR suffers from low sensitivity which can be problematic for nuclei with low natural abundance and/or small gyromagnetic ratio. This is the main reason why magnetic resonance spectroscopy/imaging of nuclei other than ^{1}H is not performed in the clinical practice despite the fact that observing ^{13}C, for example, would be potentially very informative.

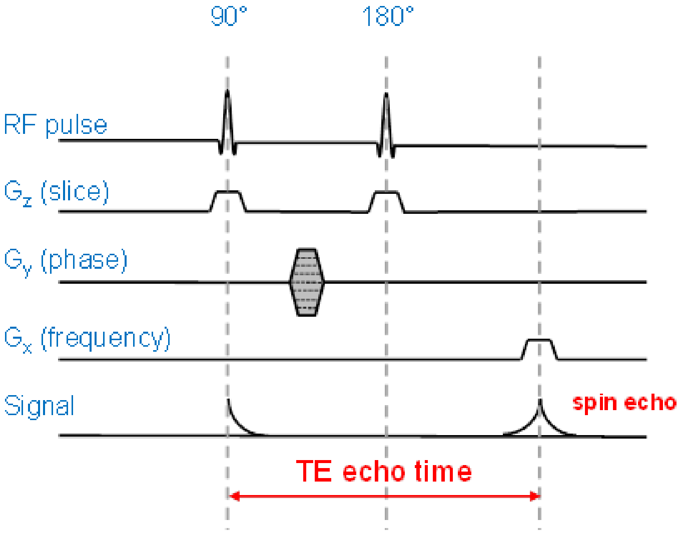

Figure 1.4. Basic spin echo (SE) pulse sequence for MR imaging.

The low sensitivity of NMR originates from the low nuclear polarization at currently used magnetic fields (around 3T) and physiological temperatures (37 ºC). The nuclear spins populate the Zeeman levels according to the Boltzmann distribution as given by

$$\frac{N^-}{N^+} = e^{-\Delta E/k_B T} \tag{1.8}$$

where ΔE is energy difference between two states ($\gamma\hbar B_0$), k_B is Boltzmann constant and T is temperature in Kelvin. Since at room temperature ΔE is much smaller than the thermal energy (k_B), the population difference is very small. This fact has major implications in NMR because the detectable NMR signal is proportional to the relative population difference (polarization, P) between the two states. The polarization can be expressed using the Brillouine fuction:

$$P = (N^+ - N^-)/(N^+ + N^-) = \tanh(\mu B_0/k_B T) \qquad (1.9)$$

Because at or near room temperature the thermal equilibrium polarization is quite low (only about 50 ppm at 7 T for ^{13}C), NMR has an inherently low sensitivity.

Obviously, the low sensitivity problem could be overcome by creating a non-equilibrium spin distribution on the Zeeman levels. Increasing the nuclear spin polarization can be achieved by several approaches; these are usually referred to as hyperpolarization techniques.[7,8] The most versatile method to enhance NMR sensitivity is based on dynamic nuclear polarization (DNP). Fast dissolution DNP technology, invented in 2003, [9] is capable of producing solutions of highly hyperpolarized ^{13}C substrates than can be directly administered (i. v.) for diagnostic purpose. [10,11] Commercial dissolution DNP polarizers are now available and the technology has advanced into clinical trials.[12]

Figure 1.5. The SPINLab DNP polarizer at the UT Southwestern Medical Center for clinical applications. The DNP polarizer is shown on the left while the computer and quality control unit is on the right.

CHAPTER 2

EFFICIENT DUAL MAGNETIC RESONANCE /NEAR INFRARED IMAGING PROBES IN AQUEOUS MEDIUM

2.1 INTRODUCTION

Most MRI contrast agents are paramagnetic species that shorten the longitudinal and transverse relaxation processes.[6] Agents which shorten the longitudinal relaxation time (T_1) increase the intensity of water signal and generate positive contrast. On the other hand, agents that decrease transverse relaxation time (T_2) cause darkening the image (negative contrast).

Among the paramagnetic transition metal and lanthanide ions Gd^{3+} has the most favorable properties for shortening the T_1 longitudinal relaxation time of water protons. It has seven unpaired f electrons and a symmetric electronic ground state ($^8S_{7/2}$), which leads to slow electronic relaxation rate. Gadolinium is a heavy metal and free Gd^{3+} is toxic, therefore, it has to be complex by an organic ligand to eliminate toxicity. Being a lanthanide, the preferred coordination number of Gd^{3+} is 8 or 9. Ligands that are used for the construction of Gd-based MRI contrast agents are usually octa- or heptadentate, and the resulting complexes have one or two inner sphere water molecules bound to the Gd^{3+} ion.[13,14]

The ^1H NMR relaxation rate (R) of the water protons in a solution of a Gd-complex has two components: the diamagnetic and paramagnetic contribution. [15]

$$R_i = \frac{1}{T_i} = \frac{1}{T_{i\ dia}} + \frac{1}{T_{i\ para}} \qquad i = 1,2 \qquad (2.1)$$

Where $\frac{1}{T_{i\ dia}}$, is the relaxation rate of the solvent (water) nuclei and $\frac{1}{T_{i\ para}}$ is relaxation rate of paramagnetic component which is proportional to the concentration of the paramagnetic species.

$$\frac{1}{T_{i\,para}} = R_{i\,para}=r_i[M] \qquad i = 1,2 \qquad (2.2)$$

Where r_i is the relaxivity. In the following sections the discussions will be restricted to r_1 as it is more relevant to Gd-based complex agents.

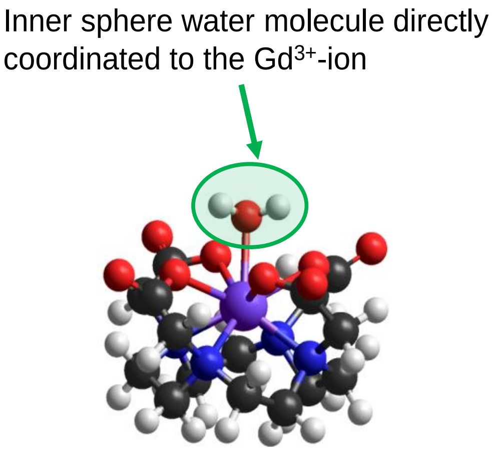

Figure 2.1. Structure of Gd-DOTA showing the inner sphere water molecule, (DOTA = 1,4,7,10-tetraazacyclododecane-1,4,7,10-tetraacetic acid).

However, similar considerations are valid for r_2. The r_1 relaxivity expresses how efficiently a complex enhances the R_1 relaxation rate and is defined and measured as the slope of the observed relaxation rate of the water protons (R_{1obs}) in solution of the Gd-complex versus the Gd-L concentration, equation (2.3):

$$r_1 = \frac{\Delta R_1}{[concentration]}$$

Thus, the observed paramagnetic relaxation enhancement of the bulk water is a composite of three effects: the inner sphere, the second sphere and the outer sphere contribution:

$$r_{1para} = r_{1inner} + r_{1second} + r_{1outer} \tag{2.4}$$

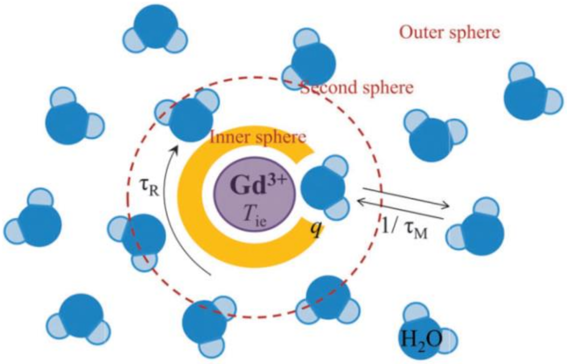

Figure 2.2. Physical parameters influencing the relaxation efficiency of MRI contrast agents at the molecular level. Reprinted with permission from Ref. 16.

The paramagnetic relaxation enhancement involves magnetic dipole-dipole interactions between the unpaired electrons of the metal ion and the ^1H nuclear spins of the water molecules. Since the strength of these interactions has very strong distance dependence (with r^{-6}) the Gd^{3+} has a very strong relaxation effect on the bound water protons. The effect on water molecules in the second sphere (not directly bound to the metal but interacting with the complex, for example by H-bonding) is much weaker. The outer sphere contribution originates from the interaction of the unpaired electrons with water molecules that diffuse in the vicinity of the complex. It is often not possible to clearly separate the second sphere and outer sphere relaxivities.[15,17] The second sphere and outer sphere contribution together can add up to about 40 % of the overall relaxivity.

As already mentioned, the exchange of the inner sphere water molecule with the bulk water molecules transfers the paramagnetic relaxation enhancement felt by the bound water protons into the bulk of the solvent. Thus, the observed paramagnetic relaxation rate ($\frac{1}{\mathrm{T}_1^{\mathrm{IS}}}$) can be expressed (Equation 2.5) ,with the relaxation time of the metal bound water protons (T_{1m}) and the average time, the water molecule stays bound to the metal ion(τ_m) and P_m (the mole fraction of the bound water):

$$\frac{1}{\mathrm{T}_1^{\mathrm{IS}}} = \frac{\mathrm{qP_m}}{\mathrm{T_{1m}+\tau_m}} \tag{2.5}$$

where q is number of inner sphere water. The paramagnetic relaxation effect can have several mechanisms such as dipole-dipole interactions, scalar coupling between the electrons of the metal ion and the ^{1}H nuclear spins and the Curie relaxation. However, for Gd-chelates at the currently used magnetic fields (1.5 - 3 Tesla) the dipole-dipole relaxation is dominant. A complete theoretical description of relaxivity originating from dipole-dipole interactions between the unpaired electrons of the Gd^{3+} and the ^{1}H nuclear spins is given by the Solomon Bloembergen Morgan theory.[18] Without going into details, the Equations (2.6) and (2.7) describing the T_{1m} relaxation time of the metal bound water protons due to dipole-dipole interactions with the unpaired electrons of a Gd^{3+} are:

$$\frac{1}{T_{1m}} = \frac{2}{15}\frac{\gamma_H^2 g_e^2 \mu_B^2 S(S+1)}{r_{GdH}^6}\left[\frac{7\tau_{c^2}}{1+\omega_S^2\tau_{c_2}^2} + \frac{3\tau_{c_1}}{1+\omega_H^2\tau_{C_1}^2}\right] \tag{2.6}$$

$$\frac{1}{\tau_{c_i}} = \frac{1}{\tau_m} + \frac{1}{\tau_R} + \frac{1}{T_{ie}} \quad ; \qquad i=1,2 \tag{2.7}$$

Where γ is gyromagnetic ratio, the isotopic Landé g factor, μ_B represents Bohr magneton, r_{GdH} is electron spin –proton distance, correlation times (τ_{ci}) and ω is chemical shift. These equations express the effect of fluctuating magnetic fields that induce nuclear spin transitions and therefore, are responsible for nuclear spin relaxation. These fluctuating fields are generated by several processes such as the rotation of the paramagnetic complex, the movement of the ^{1}H spins in and out of the vicinity of the paramagnetic center (water exchange) and the electronic relaxation of the unpaired electrons.[19] The contribution of each of these processes to the overall paramagnetic relaxation enhancement is strongly fielded dependent. These fluctuating fields are characterized by the composite correlation timesτ_{ci}, as shown in equation 2.7.

However, as a practical guideline for the design of new ligand systems for Gd-based contrast agents, the predictions of the Solomon Bloembergen Morgan theory can be summarized as follows. The relaxivity of an agent is determined by four factors: the number of bound water molecules (q), the bound water lifetime (τ_m = 1/$k_{ex,}$ where k_{ex} is the water exchange rate in s^{-1}), the rotational correlation time (τ_R) of the complex and the electronic relaxation times (T_{ie}) of the unpaired electrons at a given external magnetic field.[20] However, out of these factors, only the number of bound water molecules (q), the bound water lifetime (τ_M = 1/k_{ex}), the rotational correlation time (τ_R) can be influenced by the ligand structure. Most of the clinically used contrast agents have low relaxivity ranging from 4 to10 $mM^{-1}s^{-1}$, which is much lower than the theoretically calculated maximum value (~100 $mM^{-1}s^{-1}$ at clinically relevant magnetic fields) as predicted by the Solomon, Bloembergen, and Morgan (SBM) theory.[21] Therefore, these contrast agents must be administrated to the body in high doses, which poses a health risk. This dose could significantly be reduced if the relaxivity of the agent could be increased. The development of high relaxivity agents is an active field of research. The relaxivity is usually improved by optimizing the above mentioned key parameters as discussed in the following sections. [17]

2.1.1 Predictions of the Solomon Bloembergen Morgan Theory

According to the Solomon Bloembergen Morgan theory at the clinically relevant fields (1.5- 3 T), the relaxivity will essentially be determined by τ_M and τ_R .

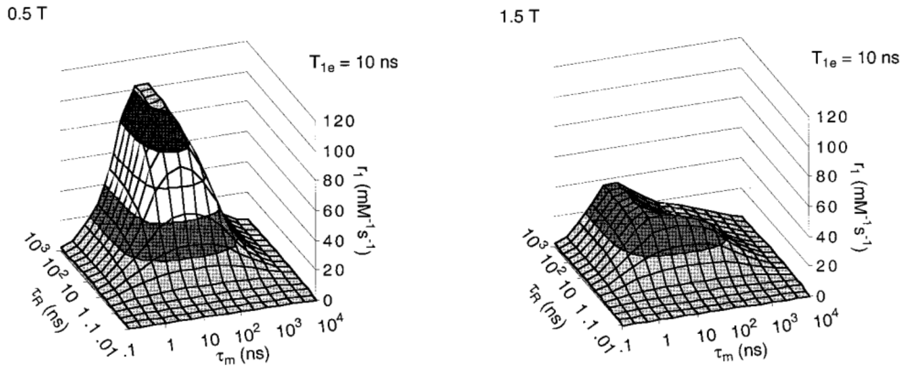

Figure 2.3. The dependence of r_1 relaxivity on by τ_M and τ_R at 1.5 T and assuming an electronic relaxation time (T_{1e}) of 10 ns of the Gd^{3+}. Reproduced with permission from Ref. 6.

As seen in Figure 2.3, increasing τ_R has a strongly field-dependent effect on the inner sphere relaxivity. At around 1.5 T, there is a significant relaxivity improvement even when τ_M is not optimal. However, the effect levels off at higher field. The optimal value of τ_M is also field-dependent and is between 10 to 50 ns for a q = 1 gadolinium complex to attain maximum inner-sphere relaxivity at clinically relevant fields. It is important to note that in case of rapidly tumbling small molecular weight complexes like Gd^{3+}-DOTA or Gd^{3+}-DTPA (τ_R < 100 ps),the relaxivity is limited by τ_R and slower than optimal water exchange rate (τ_M values up to about 1 μs) would not affect the relaxivity unless the tumbling rate of the complex is slowed down.[6,22]

Optimizing the rotational correlation time, τ_R

For spherical molecules, rotational correlation time is given by the Debye-Stokes equation:

$$\tau_R = \frac{4\pi\eta a^3}{3k_bT} \tag{2.8}$$

where η is viscosity and "a" is molecular radius. Commercially available contrast agents have τ_R value of around 0.1 ns. Increasing τ_R can easily be achieved by covalently or non-covalently binding the complex to macromolecules (polymers, dendrimers, proteins, viral capsids, various nanoparticles). Another approach involves incorporating the chelates into self-assembling systems. The most important of these strategies is the non-covalent binding to proteins. The increase in relaxivity is known as receptor-induced magnetization enhancement (RIME). Relaxation enhancement occurs only upon binding to the target protein and the effect is localized to areas where the receptor is present. The most important implementation of this concept involves binding to human serum albumin (HSA). Albumin binding agents such as the clinically approved Ablavar (gadofosveset) is used to generate high quality angiographic images of the vasculature.[4,23]

Optimizing the residence time of water molecule, τ_M

The residence life time of the bound water molecule, τ_M, is of the most important parameters that influences the relaxivity. It is the inverse of the water exchange rate. The optimal value of

τ_M at clinically relevant fields is around 20 ns and at higher magnetic field, even smaller. To reach maximum relaxivity, the value of both τ_M and τ_R must be optimized. The τ_M of usual polyaminopolycarboxylate-based monohydrated (q = 1) Gd^{3+}-complexes is longer than optimal (around 200 ns) and the design and synthesis of Gd-chelates that have faster water exchange rate has been the focus of intensive research. As a result of these efforts the steric and electronic factors that influence the water exchange rate in lanthanide complexes are well known. The water exchange of monohydrated Gd^{3+}-chelates (q = 1) proceed by a dissociative mechanism in which the bound water leaves before the incoming one can bind. In these complexes, the exchange rate can be accelerated by increasing the steric compression around the exchange site. This is usually accomplished by inserting an extra methylene group into the polyamine backbone or the sidearm of the ligand. The steric compression around the water coordination site can be significantly different in coordination isomers. Lanthanide chelates of DOTA and related ligands exist in two diastereomeric coordination isomers, SAP (square antiprism with a N_4/O_4 twist angle of approximately 39°) and TSAP (twisted square antiprism with a twist angle of around -29°). The N_4 and O_4 squares are closer to one other in the SAP isomer than in the TSAP. The inner sphere water molecule is in a capping position above the O_4 square and experiences higher steric compression in the less compact TSAP isomer. Consequently, the water exchange rate τ_M is nearly two orders of magnitude faster in this isomer than in the SAP one. These two coordination isomers are interconverting into each other, forming an equilibrium mixture but the rate of interconversion is usually slow on the NMR timescale. They can easily distinguished from each other by ^1H NMR spectroscopy since the SAP isomer has much larger lanthanide-induced ^1H NMR shifts of the ligand proton signals. Since the interaction between the Ln^{3+} ion and the bound water molecule is mainly ionic, the water exchange rate can be influenced by the electron deficiency around the central lanthanide ion. [24,25] Electronic factors provide a convenient way to fine-tune the water exchange rate. Neutral donor atoms are less capable of electron donation to the lanthanide ion and therefore, they slow down the water exchange compared to the negatively charged carboxylate oxygen. It was shown that the water exchange rate of the Gd^{3+}-DOTA derivatives in which only one coordinating sidearm was varied decreased in the following order: phosphonate > acetate > amide. In general, negatively charged complexes have faster water exchange than neutral or positively charged ones. [26]

Hydration number, q

The relaxivity linearly depends on the number of water molecules directly bound to the paramagnetic center; therefore, an increase in the number of inner sphere water molecules will increase the relaxivity. However, this will also decrease the thermodynamic stability and the kinetic inertness of complex. Another issue is that in q=2 complexes the water molecules can be displaced with bioligands such as phosphate, bicarbonate or citrate. These will bind to the chelate as bidentate ligands and the resulting ternary complex will not have a bound water molecule, which will result in a substantial decrease in relaxivity. Therefore, currently all commercially available contrast agents have only one inner sphere water molecules. In general, increasing q is not a viable way to increase the relaxivity.[15]

Gadolinium–water distance

Another parameter which can alter the relaxivity is the distance (r_H) between protons of the metal bound water molecule and paramagnetic center. This distance is around 0.30 nm for Gd(III) complexes. Since the inner sphere relaxivity is dependent on the inverse of the 6th power of this distance, small differences in r_H can lead to large changes in the relaxivity. To increase the relaxivity, distance between bound water and paramagnetic metal center should be decreased. On the other hand, there are indications that speeding up the water exchange by increasing the steric compression can lead to longer r_H thereby limiting the gain in relaxivity.[15]

2.1.2 Paramagnetic chemical exchange saturation transfer (PARACEST) agents

Another approach to enhance MR contrast is based on the transfer of saturated spins between two exchanging pools of ^1H nuclear spins. The technique is known as chemical exchange saturation transfer. The transfer of saturated spins from a small pool of proton spins to the bulk will result in the decrease of net magnetization, which generates negative contrast in the MR image. The saturation of the small pool is achieved by applying a presaturation pulse covering the resonance frequency of the small pool proton spins. [27] The condition for CEST to be observed is that the exchange rate (k_{ex}) must be smaller or equal than the frequency difference between two pools, $\Delta\omega$.

$$\Delta\omega \geq k_{ex} \tag{2.9}$$

Originally, the exchange of -OH and -NH protons of various biomolecues with bulk water was used for generating CEST (diamagnetic CEST, DIACEST).[28] However, it is difficult to selectively saturate the small pool because of the small chemical shift difference between the two pools. This problem can be overcome by using paramagnetic lanthanide complexes in which the bound water protons or some exchangeable ligand protons represent the small pool (PARACEST). In this case, the $\Delta\omega$ can be as large as several hundred ppm because these protons experience the dipolar field of the lanthanide ion, which results in large pseudocontact shifts of the ^{1}H NMR signal. The most commonly used PARACEST agents are Eu^{3+} complexes of DOTA-tetraamides largely because they have slow water exchange rate that satisfies the slow to intermediate requirement for CEST.[29]

2.1.3 Safety of lanthanide based contrast agents

In recent years, the safety of metal based MR agents has become a major concern due to nephrogenic systemic fibrosis, a devastating disease associated with the *in vivo* dissociation of Gd^{3+}-based MR agents in patients with kidney failure.[30] Furthermore, there is mounting evidence that Gd^{3+}-deposition occurs in the brain and bones of patients who have normal kidney function after multiple injections of Gd^{3+}-agents. Therefore, *in vivo* toxicity must be considered in the design new contrast agents. Toxicity in general is caused by the release of free metal from the complex. *In vivo st*ability of a metal complex is dependent on the thermodynamic stability constant as well as the kinetic rate constant that characterizes the dissociation of the complex into its components.[31] Thermodynamic stability is given by the equilibrium constant of the complex formation:

$$K_{st} = \frac{[GdL]}{[Gd^{3+}][L]} \tag{2.10}$$

The kinetic inertness is usually given as the half-life of the complex under certain conditions, e.g. at a given pH and/or in the presence of certain metal ions (Zn^{2+} or Cu^{2+}). *In vivo* dissociation or macrocyclic Gd^{3+}-complexes occurs by acid catalyzed dissociation. This process is extremely slow at pH 7, thus, these complexes have high kinetic inertness under biological conditions. On the other hand, linear Gd-chelates such as Gd-DTPA dissociate in transmetallation reactions with endogenous metal ions (Zn^{2+} and Cu^{2+}). This process is relatively fast and therefore, linear contrast agents have significantly lower kinetic inertness than the macrocyclic ones. *In vivo* toxicity data clearly indicate that open chain agents (diethylenetriaminepentaacetic acid (DTPA) derivatives) have much lower stability *in vivo* than the macrocyclic chelates (DOTA derivatives). Therefore, future development of MR agents should be based solely on macrocyclic design platform (DOTA). As of April, 2017, the European Medicine Agency's Pharmacovigilance and Risk Assessment Committee (PRAC) has recommended the withdrawal of four linear gadolinium contrast agents from the market due to *in vivo* release of Gd^{3+}.[31]

2.1.4 Luminescence

The chemical properties of the lanthanide ions are very similar due to the effective shielding of the f-orbitals by the $5s^2 5p^6$ shell. As a consequence, the ligand field effects in lanthanide complexes are very small and the f-f transitions are similar to those in the free metal ion. These transitions, however, are Laporte-forbidden, and therefore, their intensity is very low and direct excitation generally requires a very intense light source (laser). The intensity of lanthanide emission depends on how well the excited states can be populated and how much the non-radiative deactivation can be suppressed. The first objective can be achieved by sensitization with an organic chromophore. [32] The non-radiative deactivation is the deactivation of the luminescence by vibrational energy transfer usually involving high-energy vibrations of solvent molecules. The efficiency of this process basically depends on the energy difference between the lowest lying excited state and the highest sublevel of the ground state of the lanthanide ion. If this energy gap is small then it is easy to quench it by the solvent vibrational modes. O-H oscillators present in the inner sphere water molecules have the strongest deactivating effect because quenching through coupling with oscillators is strongly distance dependent (with r^{-6}). Therefore, Gd^{3+} would be the best choice in this respect, followed by Tb^{3+} and Eu^{3+} because the energy differences are 32,200 cm^{-1} ($^6P_{7/2} \rightarrow {}^8S_{7/2}$), 14,800 cm^{-1} ($^5D_4 \rightarrow {}^7F_0$) and 12,300 cm^{-1} ($^5D_0 \rightarrow {}^7F_6$), respectively. However, the $^6P_{7/2} \rightarrow {}^8S_{7/2}$ emission of Gd^{3+} is in the UV range so Gd^{3+} luminescence is not useful for biological applications.[32,33]

Generally, the energy levels of lanthanide (III) can be defined by Russell-Saunders coupling scheme, $^{(2s+1)}L_J$, where s=total spin, L= total orbital angular momentum and J = total angular momentum. The electronic energy levels are split by electron- electron repulsion, and then divided to energy levels by spin orbit coupling and these J states further split by crystal field (ligand field) effect.

Sensitizing lanthanide ions by chromophores (the antenna effect)

The conventional description of sensitizing a lanthanide ion by an organic chromophore located in the vicinity of the metal ion is outlined in Figure 2.4. It is generally assumed that the chromophore absorbs a photon and then the short lived single state is converted to triplet state by intersystem crossing, which has a longer lifetime. The energy transfer occurs from the triplet state to the metal ion. While the chromophore may be directly coordinated to the lanthanide ion, this is not an absolute requirement. [34]

The energy transfer can happen by two main mechanisms. The Forster mechanism, also known as fluorescence resonance energy transfer (FRET) involves electric dipole-dipole interactions between the donor (chromophore) and the acceptor (Ln^{3+}). The Forster energy transfer occurs through space and depends on the r^{-6} where r is the distance between the chromophore and the Ln^{3+} ion.

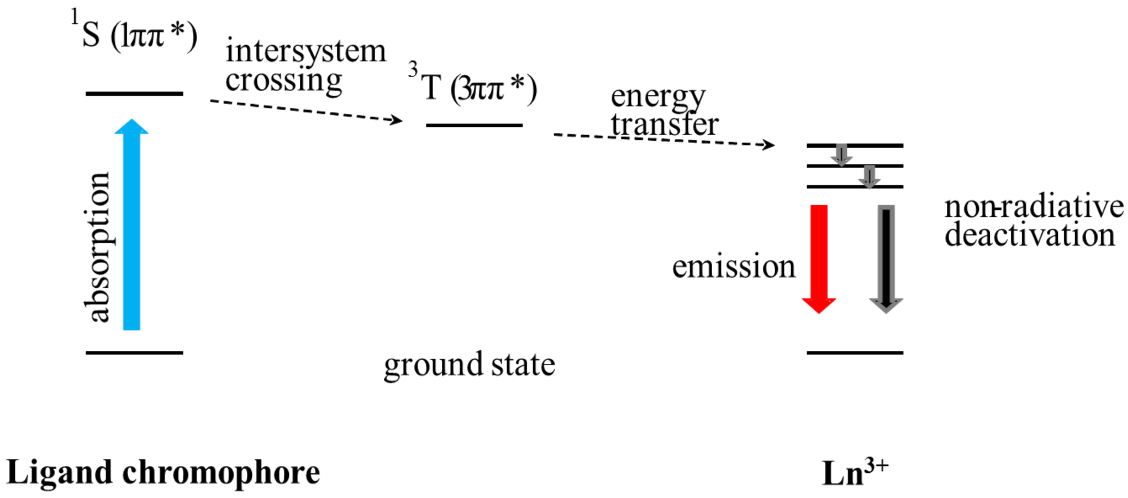

Figure 2.4. Sensitizing lanthanide ions by an organic chromophore (Antenna effect).

The Dexter mechanism involves electron exchange between the donor and acceptor, in which the excited electron moves from the donor to the acceptor.[35] The mechanism requires orbital overlap between the chromophore and the Ln^{3+}. Its efficiency is proportional to e^{-r}. It is therefore, obvious that for efficient sensitization of luminescent lanthanide ions, the ligand must have a chromophore in the close vicinity of the metal ion and triplet state energy level of the chromophore should match the excited state energy level of the lanthanide ion.

In addition, the ligand should also shield the lanthanide ion from solvent O-H oscillators to prevent non-radiative deactivation.[36] However, there are exceptions to this last requirement as will be discussed later.

Table 2.1. Luminescent transitions of lanthanide aqua ions.[33]

Ln^{3+}	**Configuration**	**Emissive transition**	**Wavelength (nm)**	**Color**
Pr^{3+}	$4f^2$	$^1G_4 \rightarrow {}^3H_J$ $^1D_2 \rightarrow {}^3F_J$ $^3P_0 \rightarrow {}^3H_J$	1300 890, 1060 525-680	NIR NIR Orange
Nd^{3+}	$4f^3$	$^4F_{3/2} \rightarrow {}^4I_J$	880, 1060, 1340	NIR
Sm^{3+}	$4f^5$	$^4G_{5/2} \rightarrow {}^6H_J$	590	Orange
Eu^{3+}	$4f^6$	$^5D_0 \rightarrow {}^7F_J$	615	Red
Gd^{3+}	$4f^7$	$^6P_{7/2} \rightarrow {}^8S_{7/2}$	312	UV
Tb^{3+}	$4f^8$	$^5D_4 \rightarrow {}^7F_J$	545	Green
Dy^{3+}	$4f^9$	$^4F_{9/2} \rightarrow {}^6H_J$	570	Yellow
Ho^{3+}	$4f^{10}$	$^5F_5 \rightarrow {}^5I_J$ $^5S_2 \rightarrow {}^5I_J$	970, 1050 540	NIR Green
Er^{3+}	$4f^{11}$	$^4S_{3/2} \rightarrow {}^4I_J$ $^4I_{13/2} \rightarrow {}^4I_{15/2}$	1530	NIR
Tm^{3+}	$4f^{12}$	$^1G_4 \rightarrow {}^3H_J$ $^3F_4 \rightarrow {}^3H_6$	480, 810	Blue NIR
Yb^{3+}	$4f^{13}$	$^2F_{5/2} \rightarrow {}^2F_{7/2}$	980	NIR

Lanthanide chelates as luminescent probes

Visible light (400–700 nm) can only penetrate about 5 mm deep in tissue before being completely absorbed by physiological chromophores such as hemoglobin and melanin. However, near infrared light (700-2500 nm) has much better tissue penetration, up to several cm, enabling *in vivo* optical imaging in this range. NIR photons have minimum absorption by blood and water in the 650 to 1350 nm wavelength range, and therefore, luminescent probes that emit in this range are potentially very useful for biological detection. While there are a large number of organic fluorophores that work reasonably well in the visible or NIR range, luminescent lanthanide chelates can offer some advantages over organic fluorophores. The favorable optical properties of lanthanide complexes include the narrow emission bands, large Stokes shifts, the lack of photobleaching, and long excited state lifetimes. This last property is particularly useful since it allows the use of time gated luminescence techniques to eliminate background autofluorescence from biological tissue. However, there are several obstacles that have to be overcome before lanthanide based luminescent complexes can make a successful transition from *in vitro* to *in vivo*. For example, the excitation and/or emission wavelengths for most complexes fall into a range where tissue penetration is weak. The quantum yield has to be improved to achieve better sensitivity, especially in aqueous media. Finally, for *in vivo* applications, the complexes must have satisfactory *in vivo* stability. Some of these issues will be addressed in this present work. It is worth mentioning that several lanthanide ions have emissions in the NIR domain and multiphoton excitation techniques now make it possible to excite Ln-complexes in or close to the NIR range.[37]

2.1.5 Magnetic Resonance / Optical Bimodal Imaging

Bimodal imaging is an emerging field within biomedical imaging. Bimodal imaging combines two different imaging modalities to take advantage of their strengths and eliminate their weaknesses.[38] The most common bimodal imaging modality is PET / CT in which anatomical images recorded by the computed tomography (CT) scanner are combined with the positron emission tomography (PET) images that contain metabolic or other functional information (for example, glucose uptake). These images then can be co-registered (superimposed) so that the functional imaging data can be precisely localized with regard to the anatomy (skeletal structure). Commercially available PET / CT scanners allow the recording of these images in one imaging session. Bimodal imaging techniques in which one of the modalities is MRI are still in the developmental stage and largely considered as a research tool rather than a clinical imaging method. Nevertheless, bimodal techniques such as MRI / PET and MRI / optical combine MRI, which can provide high resolution anatomical images of soft tissues, with an imaging modality that yields functional or molecular imaging data .This, however, poses special technical problems. MRI is inherently a 3D imaging technique as the spatial position of the voxel from which the signal originates is encoded in the frequency and phase of the signal. Optical imaging, however, is essentially a projection type imaging.

Contrast agents intended for MRI / optical bimodal imaging also have to meet special criteria. First of all, they must be able to be detected by both modalities. The same (or very similar) chemical entity should be used as bimodal contrast agent to ensure co-localization. This is very difficult, if not impossible, to achieve with a purely organic dye as no organic paramagnetic species (free radicals such as nitroxides) can match the efficiency of Gd-chelates as relaxation agents. Therefore, Gd-complexes conjugated to organic fluorescent dyes are sometimes used as MRI /optical bimodal contrast agents.[39,40] However, lanthanides provide an easy solution to this problem. The Ln^{3+} ions have nearly identical chemical properties and thus, the biodistribution is determined by the ligand, so a mixture of Gd^{3+} and another, luminescent lanthanide complex with the same ligand will have identical biodistribution and pharmacokinetics.

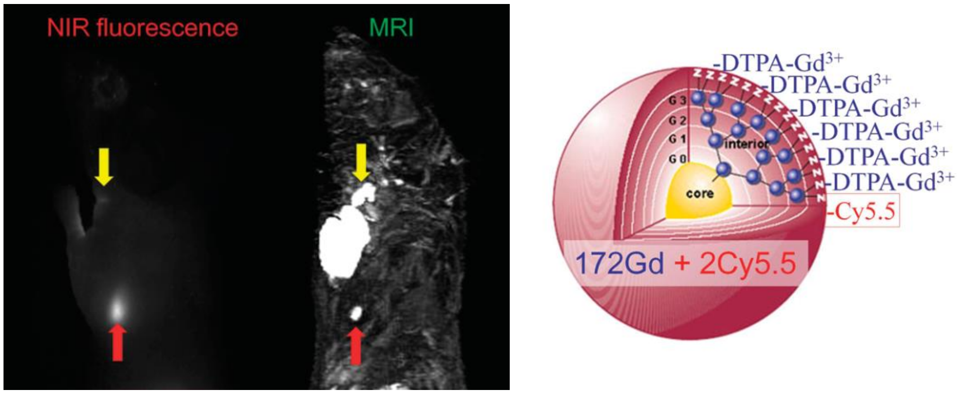

Figure 2.5. MR and NIR optical sentinel lymph node imaging of breast cancer in a mouse are shown. As depicted in this schema, generation-6 PAMAM dendrimer-based dual labeled contrast agents of approximately 10 nm in diameter containing 172 Gd ions and 2 Cy5.5 fluorophores. Reprinted with permission from Ref. 39.

Another major problem is the several orders of magnitude difference between the sensitivity of MRI and optical detection. This difference can be at least partially compensated by adjusting the ratio of Gd^{3+} / luminescent Ln^{3+} to match the sensitivity difference of the two imaging modality. Because of the much lower sensitivity of MRI, the complexes are often conjugated to Nano sized carriers in order to improve the relaxivity of the Gd-chelate component.

2.2 PROJECT GOAL

Lanthanide ions have found widespread applications as components of magnetic resonance and optical imaging agents as a result of their distinctive magnetic and optical properties.[41,42] Gadolinium complexes are well established as the preferred MR imaging contrast agents[13] while several other lanthanide ions have been explored for their luminescent emission properties in the visible or near infra-red (NIR) range. [32] Lanthanide based luminescent probes have several favorable properties including narrow emission bands, large Stokes shifts and long excited state lifetimes, which allows the use of time gated luminescence techniques to eliminate background autofluorescence from biological tissue.[32] Lanthanide ions share similar coordination chemistry properties, thus one can explore the lanthanide series with the same chelating ligand. This versatility makes it possible to construct bimodal MR/optical agents that contain Gd^{3+} for MRI and another lanthanide, such as Nd^{3+} or Yb^{3+} for NIR optical detection. Recent reports show that the similarity of the lanthanide chelates allows perfect co-localization of the MR and optical images due to identical biodistributions.[43] MR/optical bimodal imaging is particularly advantageous because it combines the high spatial resolution of MRI with the high sensitivity of optical detection.[43,44] The ligand in these bimodal agents plays multiple roles: it eliminates the toxicity associated with the free metal ion, provides a mechanism for the efficient paramagnetic relaxation enhancement of the bulk water and sensitizes the lanthanide ion emission (antenna effect). This last point is particularly important since the Laporte-forbidden f-f transitions of Ln^{3+} ions are otherwise difficult to directly excite. However, if the ligand has an appropriately positioned chromophore with compatible excited energy levels that match the excited state of the lanthanide, then efficient energy transfer can easily occur upon indirect excitation.[32,43]

The goal of this project was to develop a novel class of ligands in which one or two tropone (cyclohepta-2,4,6-trien-1-one) sidearms are appended on a DO3A (1,4,7,10-tetraazacyclodoecane-1,4,7-triacetic acid) or DO2A (1,4,7,10-tetraazacyclodoecane-1,4,7-bisacetic acid) unit (Figure 2.6). Tropolone (2-hydroxytropone) is a seven membered, non-benzenoid aromatic compound.[45,46] Its protonation constant ($pK_a = -\log K_a$) is around 7 and the tropolonate anion can act as a bidentate ligand capable of forming complexes with several alkaline earth, transition metal and lanthanide ions.[45,47] In addition, the favorable energy level of the tropolonate ion's triplet state makes it an efficient sensitizer for near infrared emitting lanthanide ions.[37] However, the stability of lanthanide tropolonate complexes is not high enough for *in vivo* applications.[47] In order to develop Ln^{3+}-based MRI and optical agents for *in vivo* use, it is important to understand the ligand's role in determining the thermodynamic stability and kinetic inertness of the complex. It is well documented that lanthanide chelates of DOTA (1,4,7,10-tetraazacyclododecane-1,4,7,10-tetraacetic acid) and related ligands have high thermodynamic stability as well as kinetic inertness (slow dissociation) and are frequently selected for various biomedical applications.[31,44] In this project, the advantageous photophysical properties of the tropone coordinating unit is combined with the favorable *in vivo* stability of the DOTA framework. Furthermore, based on structural analogies it was anticipated that the lanthanide complexes of these ligands would have one inner sphere (metal ion bound) water molecule.[126] The presence of at least one rapidly exchanging inner sphere water molecule in the Gd^{3+} complex is necessary for efficient relaxation of bulk water protons by Gd^{3+} but it is seemingly incompatible with the design of optical agents because the O-H vibrators in the metal bound water molecule can efficiently quench the lanthanide excited state by non-radiative deactivation.[43]

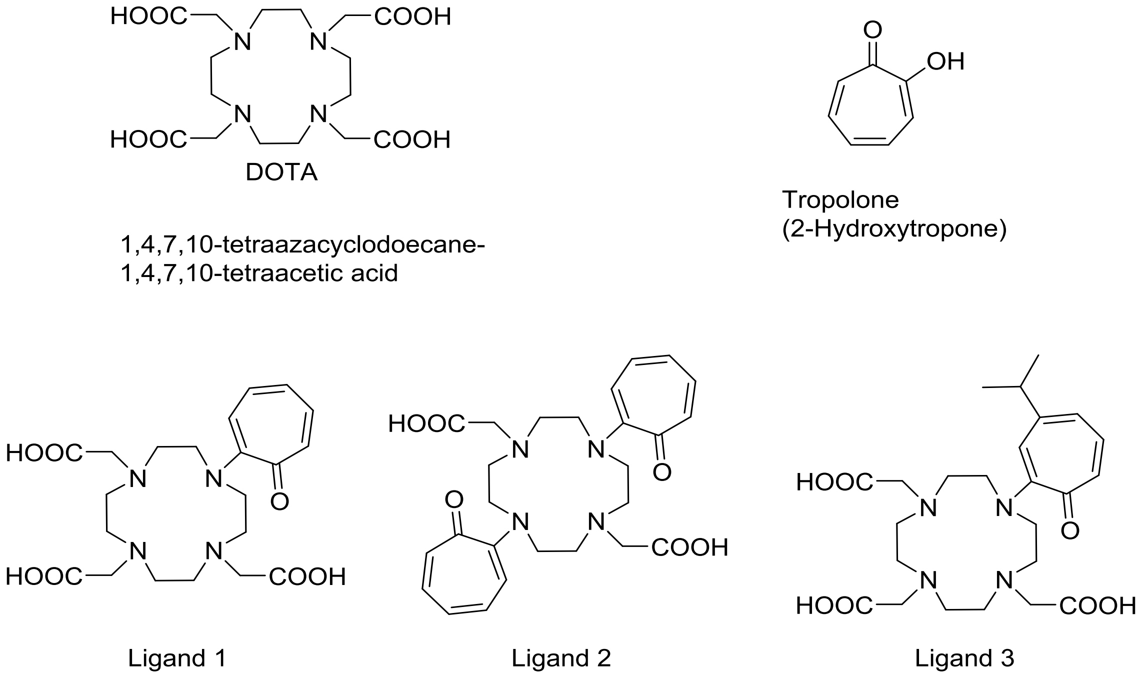

Figure2.6. Structure of DOTA, tropolone, and the DOTA-tropone derivatives discussed in this work.

The O-H oscillators present in the inner sphere water molecules have stronger deactivating effect than the solvent because quenching through coupling with the O-H oscillators is strongly distance dependent (with r^{-6}).[48] It was shown previously that pyridine based chromophores can sensitize the lanthanide to such an extent that it can overpower the non-radiative deactivation by inner sphere water molecules.[49] Nevertheless, there are only a very few reported examples of such probes that emit in the NIR region.[43,49] In this work we demonstrate that certain Ln^{3+} chelates of these DOTA-tropone derivatives display bright luminescence in the NIR domain despite the presence of one inner sphere water molecule.

2.3 EXPERIMENTAL

2.3.1 Synthesis

General Remarks. All solvents and reagents were purchased from commercial sources and used as received unless otherwise stated. ^{1}H, ^{13}C and ^{17}O NMR spectra were recorded on a Varian INOVA VNMRS direct drive Varian console spectrometer operating at 9.4 T. NMR spectra were processed in ACD/HNMR Viewer ACD/Labs 6.00.

Synthesis and characterization of ligand 1 and the Ln^{+3} complexes

1, 4, 7, 10-Tetraazacyclododecane-1,4,7-tris(acetic acid tert-butyl ester) , DO3A (t-Bu)$_3$.[50] A solution of tert-butyl bromoacetate (34.0 g) in N,N-dimethylacetamide (50 mL) was added dropwise to a solution of 1,4,7,10-tetraazacyclododecane (cyclen) (10.0g) and sodium acetate (NaOAc) (14.4 g) in N,N-dimethylacetamide (133 mL) at 0°C over 25 min. The resulting mixture was allowed to warm up to room temperature and stirred for 5 days. The white slurry was poured into water (660ml) to give clear yellow solution. The pH was adjusted to 9 by adding sodium bicarbonate ($NaHCO_3$). Potassium bromide (KBr) (10 g) was added while was stirring and after dissolution, ether (10ml) was added. After 1 hour white precipitation was formed. The precipitate was filtered off and dried in vacuum to give the 28.9 g of 1,4,7,10-tetraazacyclododecane-1,4,7-tris(acetic acid) tert-butyl ester hydrobromide as a white solid. This product was dissolved in acetonitrile (200 mL) and potassium carbonate (16 g) was added**.** The mixture was heated to 50°C and stirred overnight. The temperature was raised to 60°C and the mixture was stirred for 4 more hours. The inorganic solids were filtered and the solvent was removed by rotary evaporation. The resultant compound was dissolved in ether and washed with water 8 times and dried over sodium sulfate. The solution was filtered and solvent was removed and the residue was dried in vacuum. ^{1}H NMR (400 MHz, $CDCl_3$), δ, ppm = 3.21 (s, 6H, NCH_2CO), 2.63 (s, 4H, ringCH_2), 2.44 (s, 6H, ring CH_2), 1.34 (s, 27H, CH_3).^{13}C NMR (100 MHz, $CDCl_3$), δ, ppm = 171.09 ($COOCH_2$), 80.47(CO $(CH)_3$), 56.90(NCH_2CO), 52.2 (ring CH_2), 50.51 (ring CH_2), 47.41 (ring CH_2), 28.0 (CH_3).

1, 4, 7, 10-Tetraazacyclododecane-1,4,7-tris(acetic acid tert-butyl ester)-10-(2-tropone) 1a. To the solution of 1, 4, 7, 10-tetraazacyclododecane-1, 4, 7-tris (acetic acid tert-butyl ester) [(DO3A(t-Bu)$_3$] (1.0 g) in N,N-dimethylformamide (5ml), potassium carbonate (K_2CO_3) (550 mg) and tropolone tosylate (550 mg) were added. The reaction mixture was stirred at 60°C for 2 days. The solvent was removed in a stream of dry nitrogen gas. The yellow residue was dissolved in ether (10 mL) and washed with water (5×5 mL). The organic layer was dried over sodium sulfate and treated with activated carbon (50 mg) for 1 day. It was filtered and the solvent was removed by rotary evaporation to give the desired product as yellow oil (1.12g, 91%). ^{1}H NMR (400 MHz, $CDCl_3$, 25ºC, TMS), δ, ppm = 6.96 (dd, J(H,H) = 11.32 Hz, 8.61 Hz, 1H; tropone CH), 6.92 (t, J(H,H) = 10.45 Hz, 1H; tropone CH), 6.76 (d, J(H,H) = 11.35Hz, 1H; tropone CH), 6.50 (d, J(H,H) = 10.96Hz, 1H; tropone CH), 6.40 (t, J(H,H) = 9.00Hz, 1H; tropone CH), 3.78 (t, J(H,H) = 5.48 Hz), 4H; macrocyclic NCH_2), 3.29 (s, 2H; acetate CH_2), 3.26 (s, 4H; acetate CH_2), 3.07 (br t, 4H; macrocyclic NCH_2), 2.75 (br, 4H; macrocyclic NCH_2) 2.72

(br, 4H; macrocyclic NCH_2), 1.41 (s, 9H; t-Bu), 1.40 (s, 18H; t-Bu). ^{13}C NMR (100 MHz, $CDCl_3$, 25ºC, TMS), δ, ppm = 180.49 (tropone CO,), 170.78 (COO), 157.70 (tropone C), 134.75 (tropone C), 133.71 (tropone C), 130.33 (tropone C), 121.08 (tropone C), 111.74 (tropone C), 80.68 (COO**C**$(CH)_3$), 57.68 (N**C**H_2COO), 55.04 (N**C**H_2COO), 52.65 (macrocyclic NCH_2), 52.55 (macrocyclic NCH_2), 52.00 (macrocyclic NCH_2), 51.31 (macrocyclic NCH_2), 28.12 (CH_3), 28.06 (CH_3). MS (ESI^+), m/z, Found: 619.25, Calcd. for [M+H]: 619.41.

1,4,7,10-Tetraazacyclododecane-1,4,7-tris(acetic acid)-10-(2-tropone) 1: Compound **1a** (300 mg) was dissolved in dichloromethane (5ml) and most of the solvent was removed with N_2 gas. The residue was dissolved in trifluoroacetic acid (TFA) (5ml) and the solution was stirred at room temperature and overnight. The TFA was removed in a stream of nitrogen gas. The product was treated with ether, decanted, and the solid residue was washed with ether (20 ml) three times and dried under vacuum. It was dissolved in water (10 mL), acidified with dilute HCl solution and lyophilized to give the desired product (200 mg, 80%). ^1H NMR (400 MHz, D_2O, 25ºC, TMS), δ, ppm = 7.56 (br t, J(H,H) = 9.20 Hz, 1H; tropone CH), 7.46 (br d, J(H,H) = 9.39 Hz, 1H; tropone CH), 7.39-7.28 (broad overlapping multiplets, 3H; tropone CH), 4.09 (br s, 4H; macrocyclic NCH_2), 3.76-3.44 (broad overlapping multiplets, 14 H; macrocyclic NCH_2 and acetate CH_2), 3.22 (br, 2H; macrocyclic NCH_2), 3.06 (br, 2H; macrocyclic NCH_2). ^{13}C NMR (100 MHz, D_2O, 25ºC, TMS), δ, ppm = 185.12 (tropone CO), 171.39 (COOH), 168.47 (COOH), 155.05, 138.84, 138.61, 133.87, 133.72, 128.75 (tropone carbons), 55.38, 52.27 (acetate CH_2), 51.37, 51.31, 47.70, 45.81 (macrocyclic NCH_2). MS (ESI^+), m/z, Found: 451.11, Calcd. for [M+H]: 451.22.

Lanthanide complexes . The ligand (200 mg) was dissolved in water (5 mL) and the lanthanide chloride (approx. 10 % excess) dissolved in a small amount of water was added dropwise. The mixture was stirred for 6 days at room temperature and the pH of the reaction mixture was maintained around 6 by adding small amounts of freshly prepared hydroxide form anion exchange resin (Dowex 1X4, 20-50 mesh). The reaction mixture was then treated with Chelex resin to remove excess free metal, filtered and lyophilized to give the desired complexes. The lanthanide chelates were purified by preparative HPLC on a C18 column using water–acetonitrile 0.1% TFA gradient as eluent. All complexes had very similar retention times and gave the expected molecular weight in LC-MS measurements (retention time around 7.8 min on an Atlantis T3 5µ 4.6 mm ×250 mm C18 column, water-acetonitrile, 0.1% formic acid, 98% to 10% water gradient in 30 min).[126]

Synthesis and characterization of ligand 2 and the Ln^{+3} complexes:

1, 4, 7, 10-Tetraazacyclododecane-1, 7-bis (acetic acid tert-butyl ester), DO2A(t-Bu)$_2$. DO2A (t-Bu)$_2$ is synthesized in the chemistry lab of the AIRC on a regular basis as previously published.[51]

1, 4, 7, 10-Tetraazacyclododecane-1, 7-bis (acetic acid tert-butyl ester)-4, 10-bis (2-tropone) 2a. A mixture of DO2A (t-Bu)$_2$ (500 mg), tropolone tosylate (700 mg) and potassium carbonate (400mg), in N, N-dimethylformamide (DMF) (6 mL) was stirred at 60 °C for 24 hours. The potassium carbonate was filtered and the solvent was removed in a stream of N_2-gas .The residue was dissolved in dichloromethane (20 ml) and washed with water (5×15 mL). The organic layer was dried over sodium sulfate, treated with activated carbon, filtered and the solvent was removed by rotary evaporation to give the desired product (620 mg, 81%). ^{1}H NMR (400 MHz, $CDCl_3$) ,δ, ppm = 7.88 (2H, s, Trop), 7.76 (2H, s, Trop), 6.88 (4H, m, Trop) , 6.75 (2H, s, Trop), 3.50 (4H, s, NCH_2CO), 3.18 (2H, s, NCH_2CO), 2.94 (6H, s, ring CH_2), 2.83 (2H, s, ring CH_2), 2.75 (2H, s, ring CH_2) , 2.20 (2H, s, ringCH_2), 1.31 (4H, s, ring CH_2). ^{13}C NMR (100 MHz, $CDCl_3$, 25ºC), δ, ppm = 181.7 (C=O Trop) , 170.3 ($COOCH_2$), 157.9 (CN, Trop), 135.06 (Trop), 133.4 (Trop), 132.3 (Trop), 123.1 (Trop), 115.0 (Trop), 81.1 ($CO(CH_3)_3$), 57.3 (NCH_2), 54.1 (ring CH_2), 51.7 (ring CH_2), 28.0 (CH_3). MS (ESI^+), m/z, Found: 608.41, Calcd. for [M+H]:608.78.

1, 4, 7, 10-Tetraazacyclododecane-1,7-bis(acetic acid)-4,10-bis(2-tropone), 2. Compound **2a** (600mg) was dissolved in HCl (6 mL, 20%) and was allowed to stand for 1 day. The dark brown solution was treated with activated carbon (50mg) for 12 hours. The solution was filtered and freeze-dried to give 0.525g of yellow solid (88%). ^{1}H NMR (400 MHz, D_2O), δ, ppm= 9.15 (COOH), 7.50 (2H, s, Trop), 7.43 (2H, s, Trop), 7.35 (4H, m, Trop), 7.26 (2H, s, Trop), 7.10 (1H, m Trop), 4.0 (4H, s, NCH_2CO), 3.66 (2H, s, NCH_2CO), 3.54 (6H, s, ring CH_2), 2.26 (2H, s, ring CH_2).^{13}C NMR (100 MHZ, D_2O) ,δ, ppm = 182.8 (COOH), 167.2 (CO Trop), 154.21 (CN, Trop), 139.04 (Trop), 138.30 (Trop), 134.37 (Trop), 129.55 (Trop), 123.1 (Trop), 69.46 (CH_2ON), 54.99 (ring CH_2), 51.04 (ring CH2). MS (ESI^+), m/z, Found: 497.12, Calcd. for [M+H]: 469.56.

Lanthanide complexes. The lanthanide complexes were obtained by reacting the ligand with freshly prepared Ln $(OH)_3$. *Preparation of Ln $(OH)_3$*. The $LnCl_3$ (0.5 mmol), was dissolved in water (40 mL) and NaOH (2M, 1.2 ml) was added with stirring resulting in the formation of a precipitate. The mixture was centrifuged and the clear solution was decanted. Water (40 mL) was added to the solid residue, stirred up, centrifuged and the clear solution was again decanted. This procedure was repeated until the pH of the supernatant reached to 8. *Complexation* . Ligand 2 (100mg) was dissolved in water (5 mL) and the solution was added to the freshly prepared solid Ln $(OH)_3$. The mixture was stirred for several days while pH was periodically checked and adjusted to 7 by NaOH (2M). When the pH stabilized, it was brought to 9 and centrifuged in order to remove excess free lanthanide ions in the form of insoluble hydroxide. The resulting solution was tested for free Ln^{3+} (xylenol orange probe) and small amount (5 mg) of extra ligand was added if needed. The solution was then lyophilized. The lanthanide chelates were purified by preparative HPLC on a C18 column using water–acetonitrile 0.1% TFA gradient as eluent. All complexes had very similar retention times and gave the expected molecular weight in LC-MS measurements (retention time around 5.8 min on an Atlantis T3 5μ 4.6 mm × 250 mm C18 column, water-acetonitrile, 0.1% formic acid, 98% to 10% water gradient in 30 min). Product (Gd [bis-tropolone]) confirm by the mass spectroscopy (ESMS, ESI^+), m/z 651.83 (100%, $[M+H]^+$), Calcd. 652.14.

Synthesis and characterization of ligand 3 and the Ln^{+3} complexes:

β-Thujaplicin tosylate. β-Thujaplicin (1.0 g) was dissolved in pyridine (2.5 mL). The solution was cooled in an ice bath and tosyl chloride (1.5 g) was added slowly in ice bath and stirred for 20 min. The resulting solution allowed to warm up to room temperature and stirred overnight. The solution was diluted by dichloromethane (10 mL) and washed three times with water. The organic layer was dried over sodium sulfate and treated with activated carbon (50 mg) for 1 hour. It was filtered and the solvent was removed by rotary evaporation and the oily residue was dried in vacuum. The resulting oil solidified on standing (1.76 g, 91%). ^{1}H NMR (400 MHz, $CDCl_3$, 25ºC, TMS), δ, ppm =7.83 (br, 5H, tropone CH), 7.69 (m, 1H, ring CH), 7.11(br, 1H, ring CH), 7.0 (s, 1H, tropone CH), 6.94 (s, 1H, tropone CH) , 6.85 (br, 1H, tropone CH), 2.68 (br, 3H, ring CH_3), 2.37 (s, 8H, $(CH_3)_2CHC$), 1.12 (br, 14H, CH_3CH). ^{13}C NMR (100 MHz, $CDCl_3$, 25ºC, TMS), δ, ppm = 179.15 (tropone CO) , 157.50 (tropone CO) , 152.26 (tropone CH), 145.49 (ring C), 137.72 (tropone CH), 136.78 (tropone $CCH(CH_3)_2$), 130.69 (ring CH), 129.67 (ring CH), 128.53 (tropone CH), 38.37 (CH $(CH_3)_2$), 22.70 (CH_3).

1, 4, 7, 10-Tetraazacyclododecane-1, 4, 7-tris (acetic acid tert-butyl ester)-10-[2-(4-isopropyl) –tropone] 3a. To a solution of 1, 4, 7, 10-tetraazacyclododecane-1, 4, 7-tris (acetic acid tert-butyl ester) [(DO3A (t-Bu)$_3$] (514 mg) in acetonitrile (5ml), potassium carbonate (K_2CO_3) (300 mg) and β-thujaplicin tosylate (320 mg) were added. The reaction mixture was stirred at 60°C for 5 days. The solvent was removed in a stream of dry nitrogen gas. The yellow residue was dissolved in ether (10 mL) and washed with water (5×5 mL). The organic layer was dried over sodium sulfate and treated with activated carbon (50 mg) for 1 day. It was filtered and the solvent was removed by rotary evaporation to give the desired product as yellow oil (1.12g, 91%). ^{1}H NMR (400 MHz, $CDCl_3$, 25ºC, TMS), δ, ppm = 7.93 (br, 1H, tropone CH), 7.36 (br, 1H tropone CH), 6.87 (br ,1H tropone CH), 6.38 (br, 2H, tropone CH), (tropone CH), 3.29 (br, 2H, macrocyclic NCH_2), 2.79 (br, 3H, macrocyclic CH_2), 2.45 (br, 1H, $CH(CH3)_2$), 2.31 (br, 1H, macrocyclic NCH_2), 1.44 (s, 9H; t-Bu), 1.21 (br,3H, CH_3). ^{13}C NMR (100 MHz, $CDCl_3$, 25ºC, TMS), δ, ppm = 180.9 (tropone CO,), 171.13 (COO), 157.59 (tropone CH), 155.28 (tropone C), 138.06 (tropone CH), 135.44 (tropone C), 133.12 (tropone CH), 129.81 (tropone CH), 81.55 (t-Bu), 57.88 (N**C**H_2COO), 55.45 (N**C**H_2COO), 53.14 (macrocyclic NCH_2), 51.62 (macrocyclic

NCH_2), 51.31 (macrocyclic NCH_2), 37.93($CH(CH_3)$), 28.24(t-Bu), 21.36 (CH_3). MS (ESI^+), m/z, Found: 676.25, Calcd. for [M+H]: 676.94.

1, 4, 7, 10-Tetraazacyclododecane-1, 4, 7-tris (aceticacid)-10-[2-(4-isopropyl)-tropone] 3. Compound **3a** (300 mg) was dissolved in dichloromethane (5 mL) and most of the solvent was removed with N_2 gas. The residue was dissolved in trifluoroacetic acid (TFA) (8 mL) and the solution was stirred overnight at room temperature. The TFA was removed in a stream of nitrogen gas. The residue was treated with ether, decanted (3×20 mL), and the solid residue was dried under vacuum. It was dissolved in water (10 mL), acidified with dilute HCl solution and lyophilized to give the desired product (200 mg, 80%). ^1H NMR (400 MHz, D_2O, 25ºC, TMS), δ, ppm = 7.42 (br , 1H; tropone CH), 7.26-7.15 (broad overlapping multiplets, 3H; tropone CH), 7.07(d, 1H, tropone CH) ,4.05 (br s, 4H; macrocyclic NCH_2), 3.64-3.43 (broad overlapping multiplets, 14 H; macrocyclic NCH_2 and acetate CH_2), 3.12 (br, 2H; macrocyclic NCH_2), 3.08 (br, 2H; macrocyclic NCH_2), 2.81(d, 1H, $C(CH_3)$), 1.15(d,4H, CH_3). ^{13}C NMR (100 MHz, D_2O, 25ºC), δ, ppm = 184.57 (tropone CO), 174.54 (COOH), 169.09 (COOH), 154.37, 139.54, 135.79, 132.85, 130.52, 127.90 (tropone carbons), 55.02, 53.05 (acetate CH_2), 51.50, 49.06, 47.63, 45.90 (macrocyclic NCH_2), 37.96 ($C(CH_3)_2$), 22.19(CH_3) . MS (ESI^+), m/z, Found: 504.11, Calcd. for [M+H]: 505.59.

Lanthanide complexes. 200 mg of ligand was dissolved in 5 ml water .To the solution lanthanide chloride (approx. 10 % excess) dissolved in a small amount of water was added dropwise . The mixture was stirred for 6 days at room temperature and the pH of the reaction mixture was maintained around 6 by adding small amounts of freshly prepared hydroxide form anion exchange resin (Dowex 1X4, 20-50 mesh). The reaction mixture was then treated with

Chelex resin to remove excess free metal, filtered and lyophilized to give the desired complexes. The lanthanide chelates were purified by preparative HPLC on a C18 column using water–acetonitrile 0.1% TFA gradient as eluent. All complexes had very similar retention times and gave the expected molecular weight in LC-MS measurements (retention time around 10.6 min on an Atlantis T3 5µ 4.6 mm × 250 mm C18 column, water-acetonitrile, 0.1% formic acid, 98% to 10% water gradient in 30 min). Product confirmed by the mass spectroscopy (ESMS, ESI$^+$), m/z 661.83 (100%, $[M+H]^+$), Calcd. 662.84.

Characterization of metal complexes

The first step in characterization of metal complex is metal content analysis. For biomedical applications, the required dosage is determined based on the metal content. It should be emphasized that excess inorganic salts, free ligand and water present in the samples can significantly increase the apparent molecular weight. The Gd^{3+}-content is generally measured by inductively coupled plasma atomic emission spectroscopy (ICP-AES), also known as inductively coupled plasma optical emission spectrometry (ICP-OES) or inductively coupled plasma mass spectrometry (ICP-MS).[126] Several companies offer metal content analysis ICM-AES and MS service.

2.3.2 Relaxivity measurements

The relaxivity measurements were performed on a Bruker Minispec MQ60 and MRS-6 instrument operating at 1.4 T and 0.47T, respectively. Using an inversion –recovery pulse sequence (180-τ-90). Relaxivity of Gd^{3+} complexes of ligand **1**, ligand **2** and ligand **3** were determined by the linear regression analysis of the relaxation rates of a set of solutions ranging in concentration from 0.3 to 3 mM solution.

Relaxivity measurement with Human Serum Albumin (HSA)

Affinity constants to HSA were assessed by proton relaxation enhancement (PRE) measurements according to published procedures. The proton relaxation rates at increasing concentrations of protein were measured with a MRS-6 NMR analyzer (20 MHz, 310 K). For the enzyme titration (E-titration), the concentration of GdL complex (0.1 mM) was kept constant, while the protein concentration was varied from 0 to 0.5 mM. The data were fitted to equation (2.11), where r_1^f and r_1^c are the proton relaxivities of the free and the bound state, c_{HSA} and c_1 are the concentration of HSA and of the complex, respectively, and *n* is the number of binding sites on the protein. [52]

$$R_1^{pobs} = 10^3 \times \left\{ \begin{array}{l} \left(r_1^f . c_1\right) + \frac{1}{2}\left(r_1^c - r_1^f\right) \times \\ \left(n.c_{HSA} + c_1 + K_A^{-1} - \sqrt{\left(n.c_{HSA} + c_1 + K_A^{-1}\right)^2 - 4.n.c_{HSA}.C_1} \right) \end{array} \right\} \tag{2.11}$$

2.3.3 ^{17}O NMR measurements

^{17}O NMR experiments were performed at 9.4 T on a Bruker AVANCE III NMR spectrometer. The temperature was varying from 293 to 350 K to estimate the water exchange rates. The samples ([Gd] approximately 15 mM) were prepared in ^{17}O enriched water (2%) with the pH being maintained at 7.4 with 100 mM HEPES buffer. The sample was loaded into an 18 µL spherical bulb (Wilmad-Lab Glass, Vineland, NJ) and placed inside a 5 mm NMR tube containing 400 µL of water to eliminate any susceptibility effects. Temperatures were calibrated using ethylene glycol solution. The temperature dependence of the ^{17}O linewidths were fitted using nonlinear least-squares MATLAB fit using the following equations. The equations and parameters are explained in detail in analysis section. [53]

Determination of the number of inner-sphere bound water molecules by ^{17}O NMR

Experiment performed in 9.4 T NMR , 200 μl of the 20 mM Gd complexes in ^{17}O enriched H_2O as solvent and 5μl of tert-butal was added to the solution as an internal reference was placed in the 5mm NMR tube. After equilibration of the temperature at 70° C in the spectrometer, the ^{17}O chemical shift of the water resonance was determined. Another sample of pure ^{17}O enriched H_2O (200μl) with 5μl tert-butanol was prepared as reference and chemical shift was recorded with the same spectrometer setting. Data were fitted to the questions to obtain the number of inner sphere bound water (q).[54]

^{17}O NMR analysis

From the measured ^{17}O NMR relaxation rates and angular frequencies of the paramagnetic solutions, $1/T_2$ and ω, and of the acidified water reference, $1/T_{2A}$ and ω_A, one can calculate the reduced relaxation rates and chemical shifts, $1/T_{2r}$ and $\Delta\omega_r$, which may be written in Equations (2.12)-(2.13), where, $1/T_{2m}$ is the relaxation rate of the bound water and $\Delta\omega_m$ is the chemical shift difference between bound and bulk water molecules, τ_m is the mean residence time or the inverse of the water exchange rate k_{ex} and P_m is the mole fraction of the bound water. [31,55]

$$\frac{1}{T_{2r}}=\frac{1}{P_m}\left[\frac{1}{T_2}-\frac{1}{T_{2A}}\right]=\frac{1}{\tau_m}\frac{T_{2m}^{-2}+\tau_m^{-1}T_{{2m}^{-1}}+\Delta\omega_m^2}{(\tau_m^{-1}+T_{2m}^{-1})^2+\Delta\omega_m^2}+\frac{1}{T_{2os}} \tag{2.12}$$

$$\Delta\omega_r=\frac{1}{P_m}(\omega-\omega_A)=\frac{\Delta\omega_m}{(1+\tau_m T_{2m}^{-1})^2+\tau_m^2\Delta\omega_m^2}+\Delta\omega_{os} \tag{2.13}$$

The outer sphere contributions to the ^{17}O relaxation rates $1/T_{2OS}$ are being neglected according to previous studies.[45] Therefore, Equations (2.12-2.13) can be further simplified to Equation (2.14):

$$\frac{1}{T_{2r}} = q\frac{p_m}{T_{2m} + \tau_m} \tag{2.14}$$

The exchange rate obeys the Eyring Equation (2.15). In Equation (2.15) $\Delta S^{\ddagger}$ and $\Delta H^{\ddagger}$ are the entropy and enthalpy of activation for the water exchange process, and k_{ex}^{298} is the exchange rate at 298.15 K.

$$\frac{1}{\tau_m} = k_{ex} = \frac{k_B T}{h}\exp\left\{\frac{\Delta S^{\ddagger}}{R} - \frac{\Delta H^{\ddagger}}{RT}\right\} = \frac{k_{ex}^{298} T}{298.15}\exp\left\{\frac{\Delta H^{\ddagger}}{R}\left(\frac{1}{298.15} - \frac{1}{T}\right)\right\} \tag{2.15}$$

In the transverse relaxation, the scalar contribution, $1/T_{2\mathrm{sc}}$, is the most relevant [Equation (2.16)]. $1/\tau_{\mathrm{s1}}$ is the sum of the exchange rate constant and the electron spin (S) relaxation rate [Equation (2.17)].

$$\frac{1}{T_{2\mathrm{m}}} \cong \frac{1}{T_{2\mathrm{sc}}} = \frac{S(S+1)}{3}\left(\frac{A}{\hbar}\right)^2\left(\tau_{s1} + \frac{\tau_{s2}}{1+\omega_S^2\tau_{s2}^2}\right) \tag{2.16}$$

$$\frac{1}{\tau_{s1}} = \frac{1}{\tau_m} + \frac{1}{T_{1e}} \tag{2.17}$$

In Equation (2.13) the chemical shift of the bound water molecule, $\Delta\omega_m$, depends on the hyperfine interaction between the Gd^{3+} electron spin and the ^{17}O nucleus and is directly proportional to the scalar coupling constant, $A/\hbar$, as expressed in Equation (2.18).[46]

$$\Delta\omega_m = \frac{g_L \mu_B S(S+1)B}{3k_B T}\frac{A}{\hbar} \tag{2.18}$$

The isotopic Landé g factor is equal to 2.0 for the Gd^{3+}, μ_B represents the dipolar magnetic moment, and k_B is the Boltzmann constant. The outer-sphere contribution to the chemical shift is assumed to be linearly related to $\Delta\omega_m$ by a constant C_{os} [Equation (2.19)].[37]

$$\Delta\omega_{os}=C_{os}\Delta\omega_m \tag{2.19}$$

2.3.4 Data analysis

In the ^{17}O NMR data fitting for the Gd^{3+} complexes, r_{GdO} has been fixed to 2.50 Å, based on available crystal structures and recent electron spin-echo envelope modulation (ESEEM) results[56]. The quadrupolar coupling constant, χ $(1+\eta^2/3)^{1/2}$, has been set to the value for pure water, 7.58 MHz. The parameters characterizing the electron spin relaxation, such as the correlation time for the modulation of the zero-field-splitting, τ_v^{298}, and its activation energy, E_v, and the mean-square zero-field-splitting energy, Δ^2 were fixed with $[GdDOTA(H_2O)]^-$ to 11 ps, 1 kJ mol^{-1} and 0.16×10^{-20} s^{-1}, respectively, for simpler analogy as reported for various Gd-DOTA derivatives.[57] The empirical constant describing the outer sphere contribution to the ^{17}O chemical shift, C_{os}, was also fitted for the all Gd complexes (0.1 ± 0.01) otherwise small $A/\hbar$ values were obtained.[57] Inner sphere water molecules were adjusted to the values calculated by ^{17}O NMR for each complex.[6]

2.3.5 In *vivo* experiments

All animal experiments were conducted according to the standard of the University of Texas Southwestern Medical Center Institutional Animal Care and Use Committee. Male

C57/blk6 mice of 6-10 weeks of age (approximately 30 g) were used for imaging. Animals were anesthetized with isoflurane (1-2% in medical oxygen) and probes were places on the skin to monitor temperature and on the chest to monitor respiration. Each animal experiment was performed three times. Gd**1** (15 mM, 100 μL, 0.05 mmol/kg and 30 mM, 100 μL, 0.1 mmol/kg doses) and Gd**2** (30 mM, 100 μL, 0.1 mmol/kg doses) were administered by i.v. injection. T_1-weighted imaging was performed on a 9.4T imaging system using a ge3D sequence. [126] The following parameters were used: TR 3.6 ms, TE 1.8ms, FOV $35 \times 75 \times 75$ mm^3, flip angle 20°, data matrix 128*128*128, 4 averages. Where the TR, TE and FOV are repetition time, echo time and filed of view respectively.

2.3.6 Photophysical measurements

Photophysical data were collected on samples in solution (HEPES buffer at pH 7.4 or D_2O) placed in 2.4 mm i.d. quartz capillaries or quartz Suprasil cells. Absorption spectra were acquired on a Jasco V670 spectrophotometer. Emission and excitation spectra were measured on a custom-designed Horiba Scientific Fluorolog 3 spectrofluorimeter equipped with a visible photomultiplier tube (PMT) (220–850 nm, R928P; Hamamatsu), a NIR solid-state InGaAs detector cooled to 77 K (800–1600 nm, DSS-IGA020L; Horiba Scientific), or a NIR PMT (950–1650 nm, H10330-75; Hamamatsu). Excitation and emission spectra were corrected for the instrumental functions. Luminescence lifetimes were determined under an excitation at 355 nm provided by a Nd:YAG laser (YG 980; Quantel). Signals were detected in the NIR by a Hamamatsu H10330-75 PMT. Output signals from the detector were fed into a 500 MHz bandpass digital oscilloscope (TDS 754C; Tektronix), transferred to a PC for data processing with the software Origin 8®. Luminescence lifetimes are averages of at least three independent measurements. Quantum yields were determined with a Fluorolog 3 spectrofluorimeter based on an absolute method with the use of an integration sphere (Model G8, GMP SA, Renens, Switzerland).[58] Each sample was measured several times under comparable experimental conditions, varying the position of samples. Estimated experimental error for the quantum yield determination is ~10 %. [58,126]

2.4 RESULT AND DISCUSSION

2.4.1 Structural characterization

The synthesis of ligands 1-3 are outlined in Scheme 2.1, 2.2 and 2.3. Tropones with a leaving group (Cl, Br or OTs) at position 2 easily undergo aromatic nucleophilic substitution. [45] We have chosen the commercially available tropolone-p-toluenesulfonate (tropolone tosylate) for the synthesis of ligand 1 and 2. This reagent reacted cleanly with DO3A-tris (tert-butyl ester) and DO2A-bis (tert-butyl ester) to give the expected tert-butyl protected products (Scheme 2.1 and 2.2). DO3A $(t\text{-Bu})_3$ and DO2A$(t\text{-Bu})_2$ are convenient starting materials that are frequently used for the synthesis of mixed sidearm DOTA derivatives compounds. Finally, for photophysical meaurements and *in vivo* imaging, the complexes were purified by preparative HPLC using a reversed phase C18 column and water–acetonitrile 0.1% TFA gradient as eluent, which removed inorganic salts along with other unwanted impurities. [126]

Acid hydrolysis of the tert-butyl groups gave the desired ligands as free acid in good yield. For the synthesis of ligand 3 the isopropyl derivative β-thujaplicin tosylate was easily obtained by reacting the commercially available β-thujaplicin (2-hydroxy-4-isopropyl-2,4,6-cycloheptatrien-1-one,4-isopropyl tropolone) with tosyl chloride in the presence of pyridine as base.

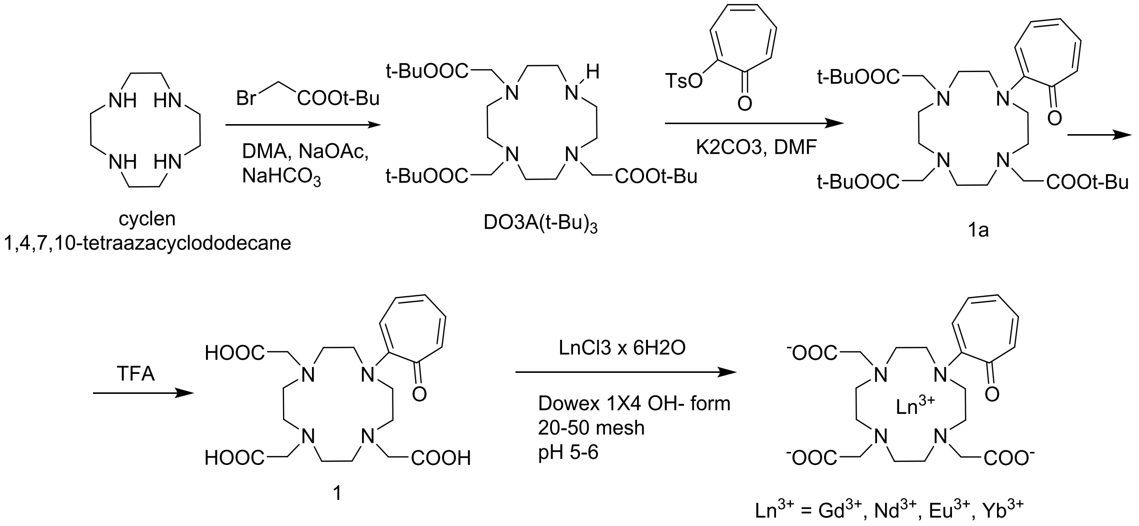

Scheme 2.1. Synthesis of ligand **1** and its complexes.[126]

The neutral lanthanide complexes of ligand 1 and 3 were prepared by adding $LnCl_3$ solutions (Ln = Gd, Eu, Nd and Yb) and (Ln=Gd) respectively to the ligand at pH 6 in the presence of OH-form anion exchange resin as a base. The use of anion exchanger minimized the presence of inorganic salts in the final product. Ligand **2** forms positively charged lanthanide complexes and in this case, the lanthanide complexes were prepared by adding $Ln(OH)_3$ solution (Ln = Gd, Eu, Nd and Yb) the ligand at pH 7. A slight excess of metal ion was employed to ensure complete complexation of the ligands. After complexation, the excess of metal was removed by raising the pH above 8 where Ln^{3+} ions form insoluble hydroxide. Traces of metal ion were removed by treatment with Chelex resin, which has free iminodiacetic acid moieties for metal binding.

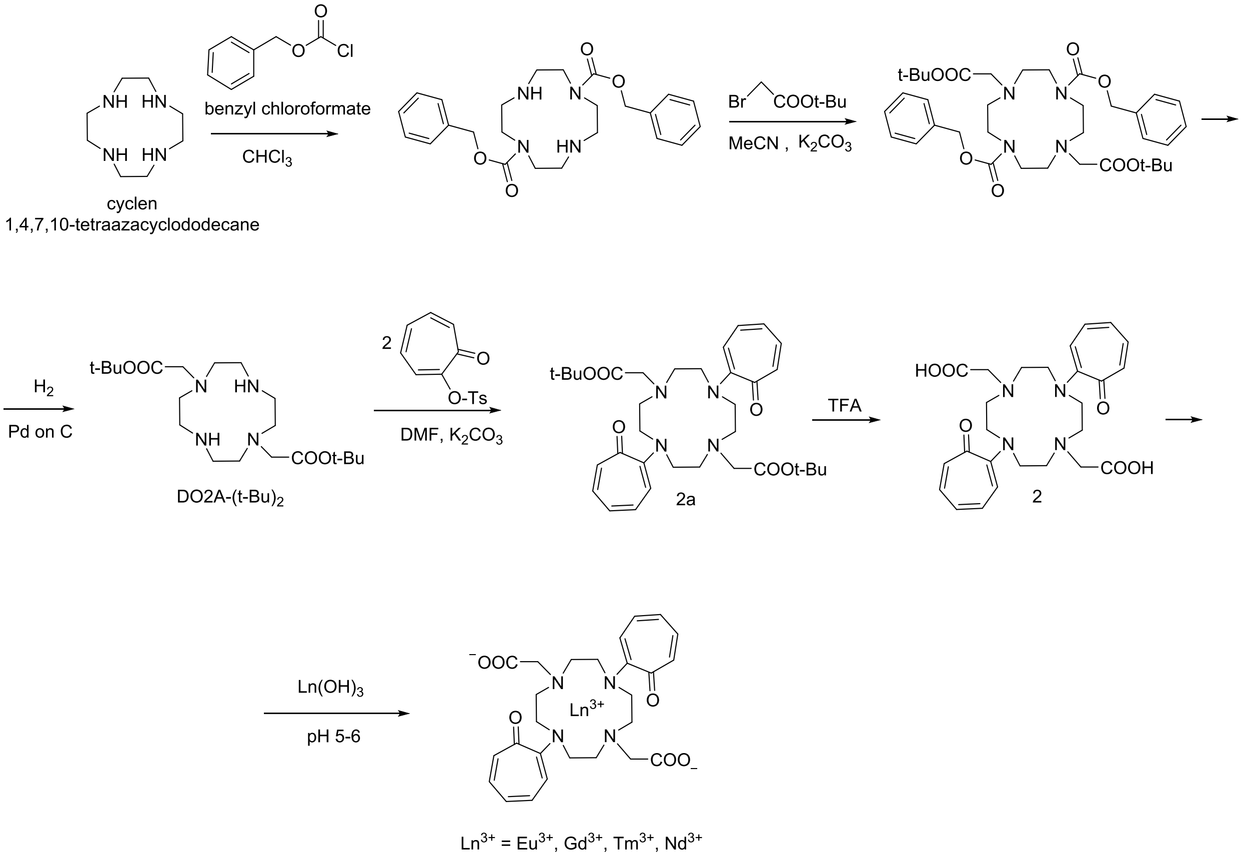

Scheme 2.2. Synthesis of ligand **2** and its complexes.

The absence of free metal was confirmed by the xylenol orange test. The resulting solutions were lyophilized to yield the compounds. Finally, for photophysical measurements and *in vivo* imaging, the complexes were purified by preparative HPLC using a reversed phase C18 column and water–acetonitrile 0.1% TFA gradient as eluent, which removed inorganic salts along with other unwanted impurities.

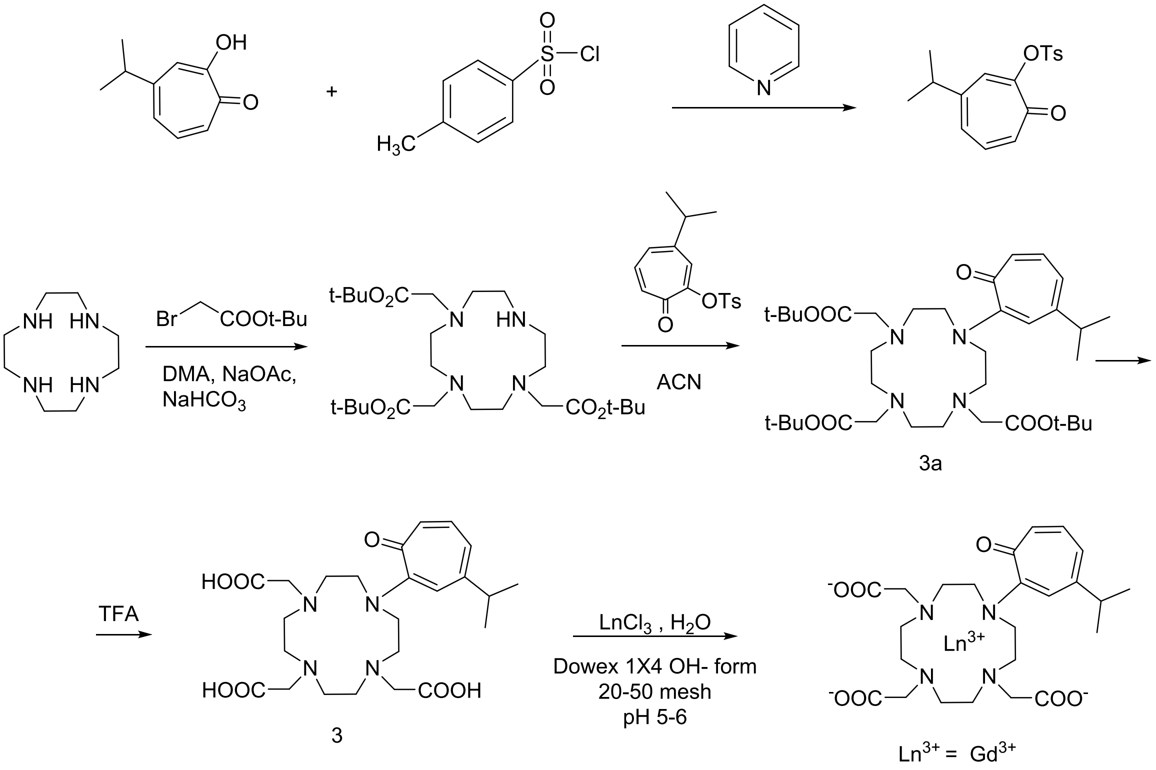

Scheme 2.3. Synthesis of ligand **3** and its complexes

2.4.2 High resolution of ^1H NMR spectra

Lanthanide chelates of DOTA and related ligands exist as mixtures of interconverting coordination isomers. These isomers differ in the twist angle of the N4/O4 squares. The square antiprism (SAP) isomer has a N4/O4 twist angle of approximately 39° while the twisted square antiprism (TSAP) isomer has a twist angle of around 27°. The N4 and O4 squares are closer to each other in the SAP isomer than in the TSAP, and therefore, the former has a more compact structure. [24,25] This is clearly illustrated by the much larger lanthanide-induced ^1H NMR shifts of the ligand proton signals. The inner sphere water molecule occupies a capping position above the O4 square and so in the more compact structure of the SAP isomer it is located closer to the metal ion. The shorter Ln-O distance means the SAP isomer generally has slower water exchange. Thus, the existence of these isomers is important for the design of MRI contrast agents because of the differences in water exchange rates of these forms. Due to the more open cavity of the TSAP form, the larger (lighter) lanthanide ions (Ce^{3+}, Pr^{3+} and Nd^{3+}) usually prefer the TSAP geometry while the smaller (heavier) lanthanides (Tb^{3+} and above) prefer the more compact SAP geometry.

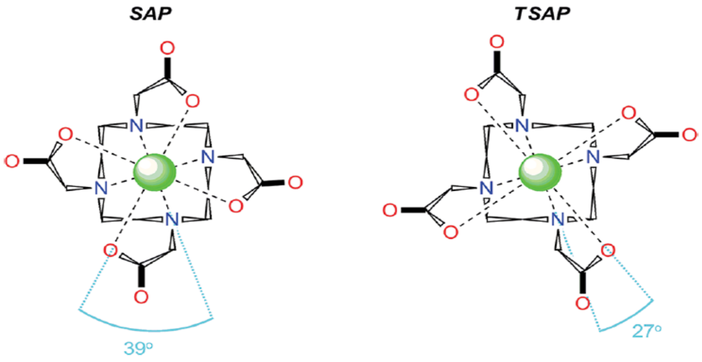

Figure 2.7. Model of LnDOTA-type chelate. The macrocyclic ring adopts a square conformation with a carbon atom at each corner. The four nitrogen donor atoms of the ring coordinate to one face of the metal ion while the four oxygen atoms of the pendant arm carboxylates coordinate to the opposite face. The coordination is completed by a capping water molecule. The DOTA-type chelates may adopt one of two coordination geometries, a capped square antiprism, SAP or capped twisted square antiprism, TSAP, defined by the torsion angle between the two coordination planes. Reprinted with permission from Ref. 24, 25. Copyright 2012 American Chemical Society.

Complexes of the medium sized Ln^{3+} ions such as Sm^{3+}, Eu^{3+} and Gd^{3+} exist as an equilibrium mixture of both isomers. The coordination geometry can easily be determined by ^{1}H NMR spectroscopy because the Ln^{3+} induced dipolar shifts of the ligand protons are quite different in the two forms. The paramagnetic shift of the axial ax_1 (H4) protons is particularly informative: for most lanthanides, the ^{1}H NMR signal of the H4 macrocyclic proton is about twice as large in the SAP than in the TSAP isomer.

^{1}H NMR spectra of Nd1, Eu1 and Yb1

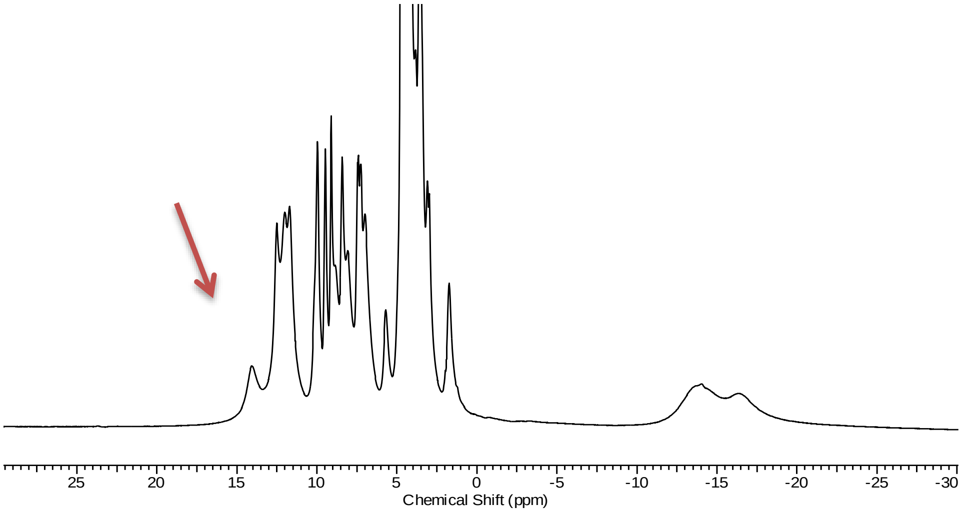

Figure 2.8a. ^{1}H NMR spectrum of Nd**1** recorded in D_2O, pD 7, 9.4 T, 25 ºC.

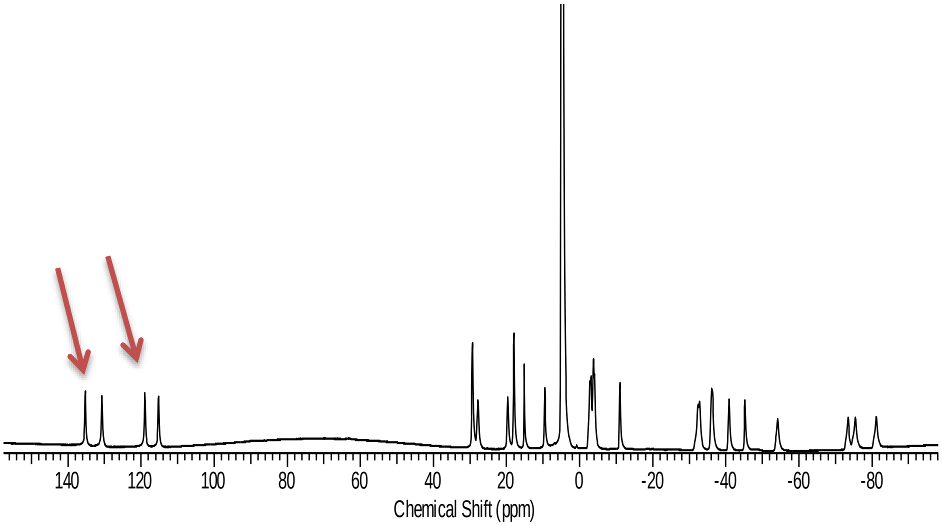

Figure 2.8b. ^{1}H NMR spectrum of Yb**1** recorded in D_2O, pD 7, 9.4 T, 25 ºC

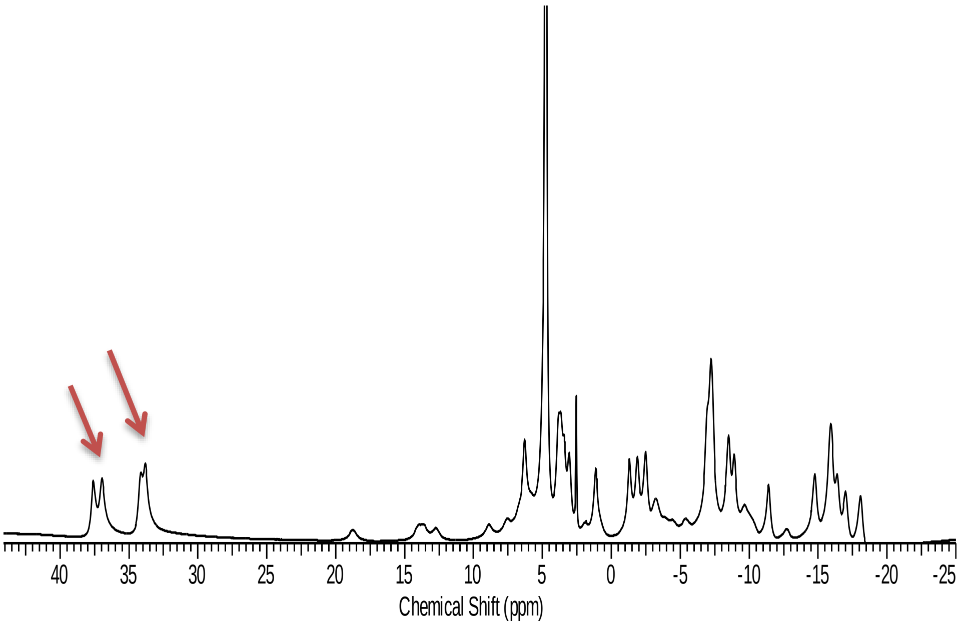

Figure 2.8c. ^{1}H NMR spectrum of Eu**1** recorded in D_2O, pD 7, 9.4 T, 25 ºC.

^{1}H NMR spectra of Nd2, Eu2 and Yb2

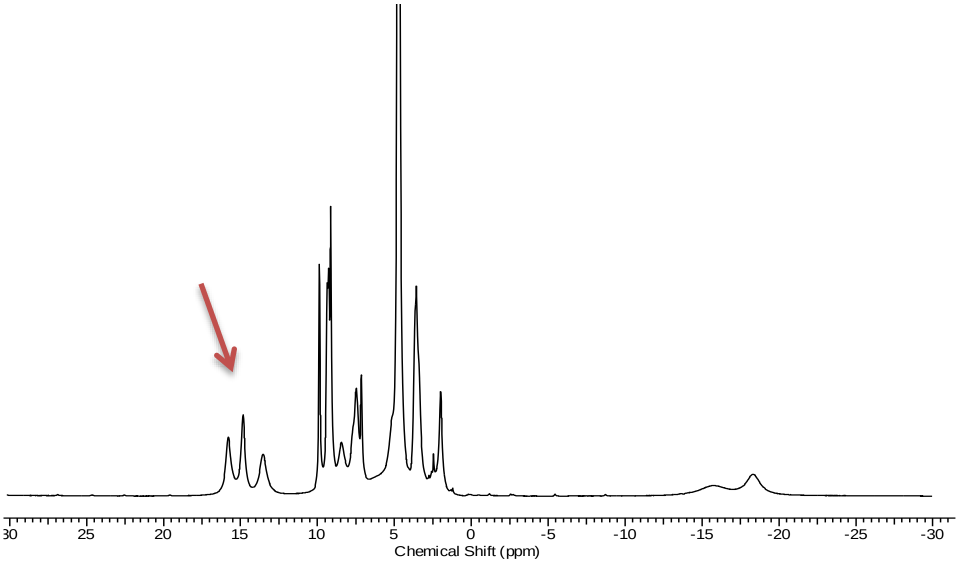

Figure 2.9a. ^{1}H NMR spectrum of Nd**2** recorded in D_2O, pD 7, 9.4 T, 25 ºC.

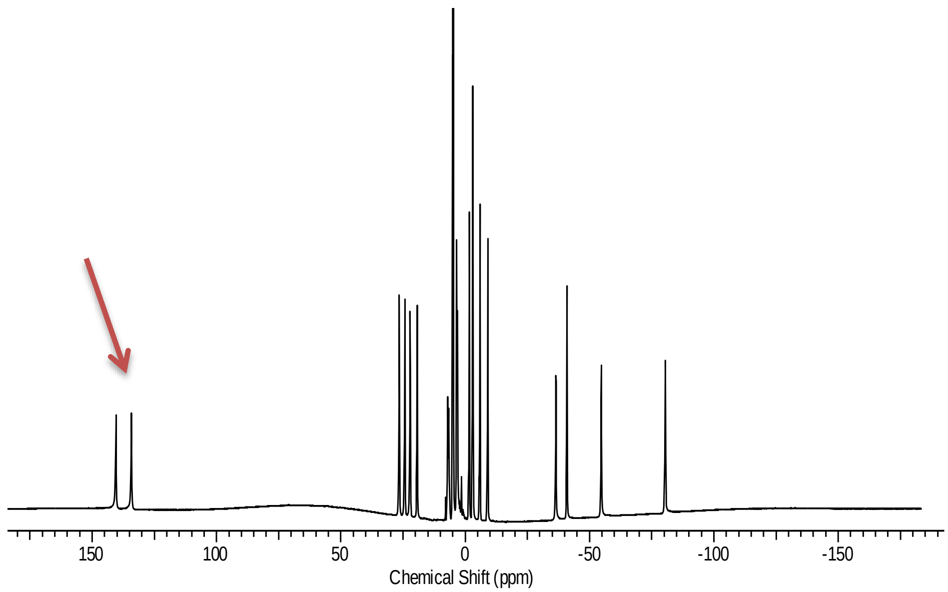

Figure 2.9b. ^{1}H NMR spectrum of Yb**2** recorded in D_2O, pD 7, 9.4 T, 25 ºC.

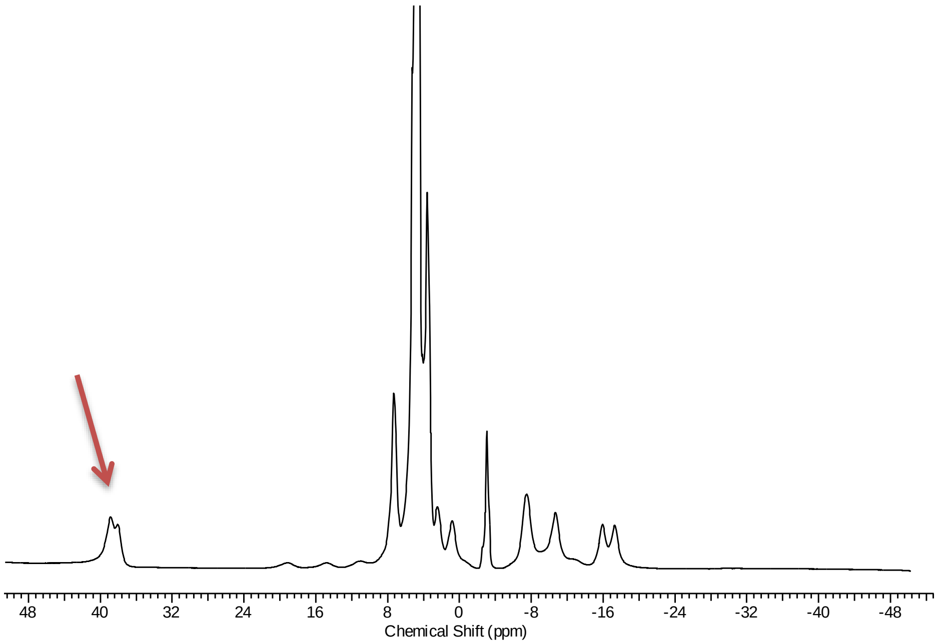

Figure 2.9c. ^{1}H NMR spectrum of Eu**2** recorded in D_2O, pD 7, 9.4 T, 25 ºC.

Thus, the shifts of the H4 protons in the ^{1}H NMR spectrum of Nd**1** (Figure 2.8a) indicates that this complex exclusively adopted the twisted square antiprism (TSAP) geometry. Eu**1** exists in solution predominantly as the square antiprism (SAP) isomer with about 20 % of the TSAP form while and Yb^{3+} chelate exclusively formed the SAP isomer. ^{1}H NMR spectra of ligand **2** indicated that the Nd^{+3} complexes (Figure 2.9a) adopted the twisted square antiprism (TSAP) geometry. Eu**2** exists in solution as the square antiprism (SAP) isomer and Yb^{3+} chelate exclusively formed the SAP isomer. This behavior is analogous to that of the corresponding DOTA complexes. [56]

2.4.3 Determination of the number of inner sphere water molecules in the Gd complexes

The number of inner sphere water molecules in Gd**1**, Gd**2** and Gd**3** complexes were measured by ^{17}O NMR bulk magnetic susceptibility water shift measurements The determination of the number of coordinated water molecules in Ln(III) complexes by ^{17}O NMR spectroscopy was performed as described previously by Djanashvily et al. Gd^{3+} complexes (in D_2O) were used for these studies, since at the fast exchange regime (high temperatures) the ^{17}O chemical shifts of water bound to these lanthanide ions are mostly of contact contribution. The calculations performed provided $q(Gd^{3+}) = 1.4 \pm 0.2$.

2.4.4 Relaxivity measurements at 1.4 T and 0.47 T

As discussed previously, the r_1 relaxivity characterizes how efficiently a contrast agent can shorten the nuclear T_1 relaxation time of the bulk water protons. It is generally measured as the slope of R_1 relaxation rate vs the concentration of the agent at 37 °C. Figure 2.10, 2.11 and 2.12

shows the experimental data for Gd**1**, Gd**2** and Gd**3** measured at two different fields (0.47 T and 1.4 T). The r_1 values are summarized in Table 2.2, along with literature data reported for some other Gd complexes. These values fall in the range that is expected for a small molecular weight complex with one metal bound water molecule. [13,59] The slightly higher r_1 values at lower field are also in agreement with theoretical predictions. Not surprisingly, Gd**3** had the highest relaxivity among the studied complexes, very likely because of its slower rotational correlation time (tumbling rate) and somewhat faster water exchange rate (see following section).

The paramagnetic relaxation effect between the Gd^{3+} ion and the ^1H nuclei is mediated through magnetic dipole-dipole interactions between the electron and nuclear spins. The strength of these dipole-dipole interactions has a r^{-6} distance dependence.

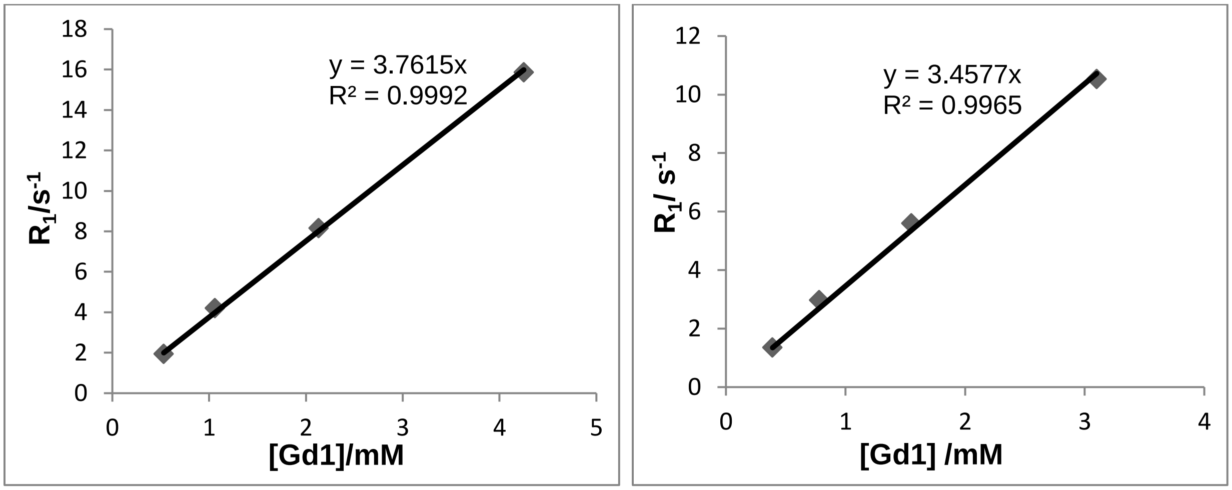

(a) (b)

Figure 2.10. Plot of the relaxation rate of Gd**1** versus concentration at (a) 0.47 T, (b) 1.4 T; 37 ºC in water at pH 7.

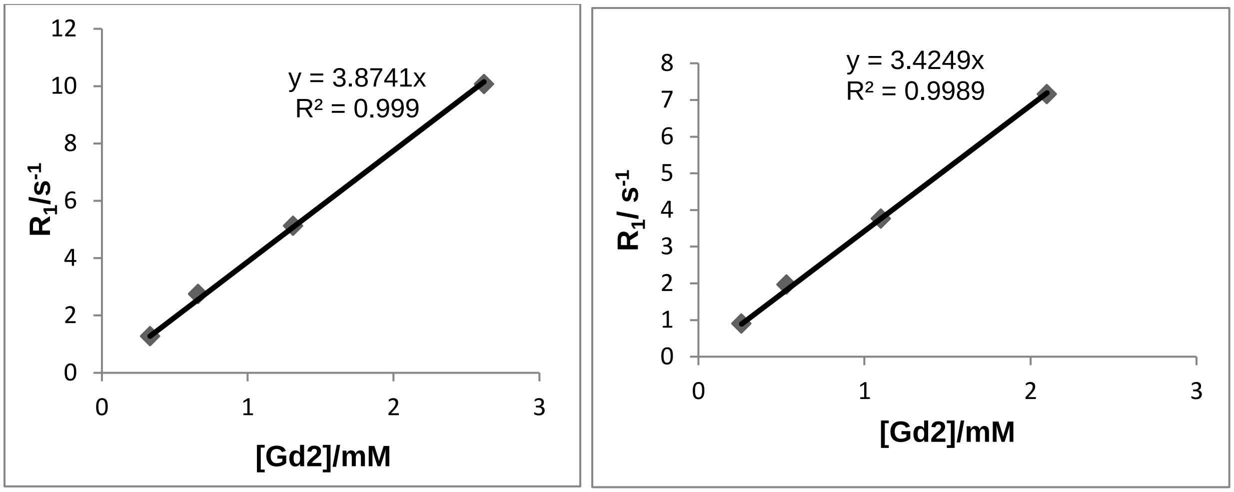

(a) (b)

Figure 2.11. Plot of the relaxation rate of Gd**2** versus concentration at (a) 0.47 T, (b) 1.4 T; 37 ºC in water at pH 7.

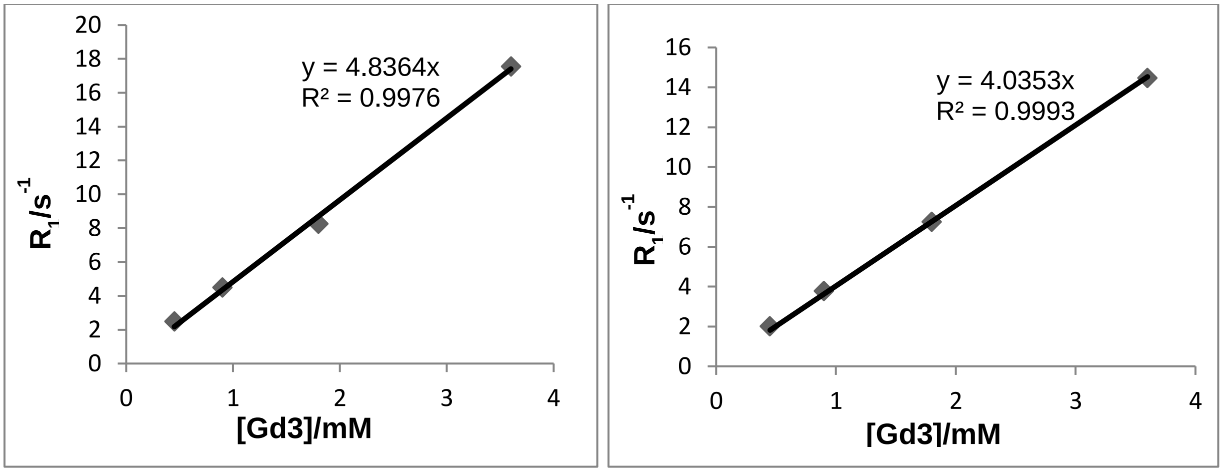

(a) (b)

Figure 2.12. Plot of the relaxation rate of Gd**3** versus concentration at (a) 0.47 T, (b) 1.4 T; 37 ºC in water at pH 7.

Table 2.2. Summary of relaxivity data at different magnetic fields

Agent	**r_1 at 0.47 T**	**r_1 at 1.4 T**	**References**
Gd1	3.8	3.5	This work [126]
Gd2	3.9	3.4	This work
Gd3	4.8	4.0	This work
Magnevist	3.4	3.3	Ref.[60]
Omniscan	5.3	4.7	Ref.[60]
Prohance	3.1	2.9	Ref.[60]
Dotarem	3.4	2.9	Ref.[60]
Gadovist	3.7	3.3	Ref.[60]

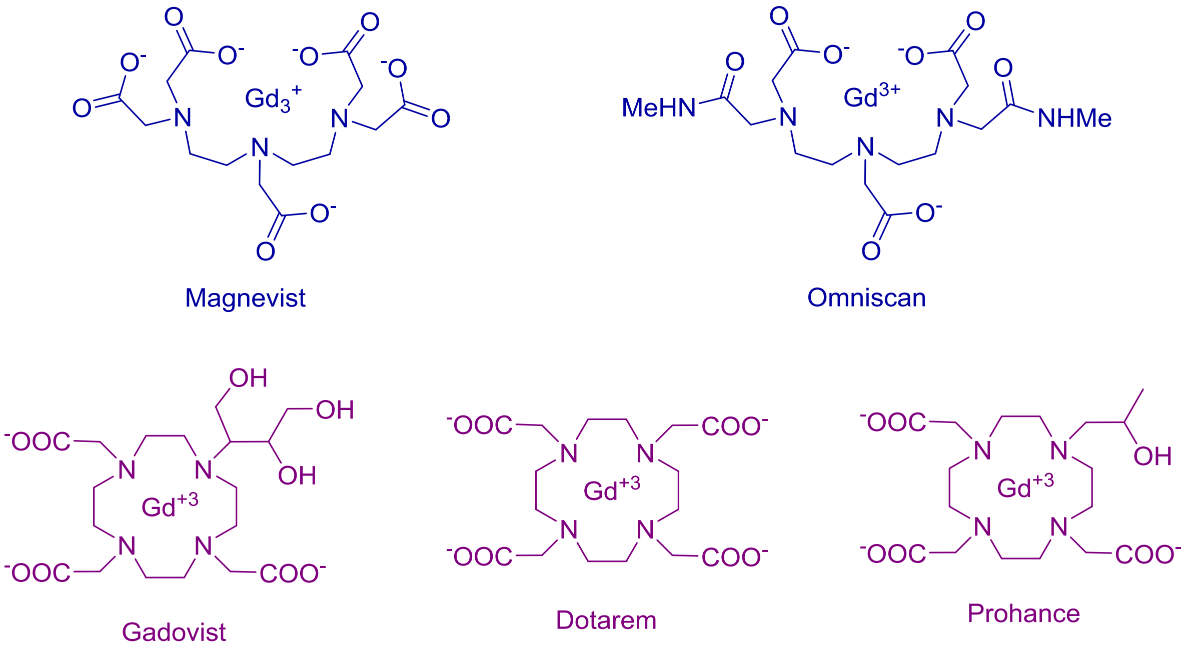
Magnevist

Omniscan

Gadovist

Dotarem

Prohance

Figure 2.13. Commercially available linear (open chain) and macrocyclic Gd containing MRI contrast agents that do not bind to serum albumin Reprinted with permission from Ref. 60.

Therefore, the paramagnetic relaxation enhancement is the strongest on the ^{1}H nuclei of the water molecules that are directly bound to the Gd^{3+} ion. The paramagnetic effect of the Gd^{3+} is transferred to the bulk water protons by the exchange of the inner-sphere water molecule. In order to have efficient relaxation of the bulk water proton spins, the bulk water protons of the solvent must be in rapid exchange with the inner sphere water protons (directly bound to the lanthanide) of the Gd $^{3+}$ complex. However, it is important to emphasize that there is an optimal range for the water exchange. The maximum $r_1$value cannot be achieved, if the water exchange is too fast or too slow. Based on SBM theory, for Gd^{3+} complexes with q=1, the $r_1$value depends on the molecular tumbling correlation time,τ_c , bound water lifetime (τ_M) and magnetic field. If τ_M is too short (<1 ns), the water molecule does not spend enough time bound with the lanthanide center to get fully relaxed. On the other hand, if τ_M is too long (>1μs), the fewer bulk water molecules exchange with the inner sphere water molecule and the paramagnetic relaxation effect of the Gd^{3+}-ion is not efficiently transferred to the bulk. Therefore, τ_M must be optimal to have maximal r_1 value at any imaging field strength.

Thus, the exchange rate (k_{ex}) of the metal bound water is an especially important parameter in the design and optimization of MR agents. The k_{ex} is frequently discussed as residence lifetime (τ_M = 1/k_{ex}). Based on SBM theory, for optimal relaxivity, k_{ex} value should be around 10^8 s^{-1}. Water exchange rates of current Gd^{3+} complexes based on a polyazapolycarboxylate framework are slower ($k_{ex}\approx$ 10^6 s^{-1}), than the optimal value which is predicted by the SBM theory. [61] As described previously, the steric and electronic factors that influence water exchange rate in lanthanide complexes are now well known. Generally, increasing steric crowding around the lanthanide ion as well as increasing negative charge tends to accelerate the water exchange rate.

Replacing an acetate arm of DOTA with bulkier methylenephosphonate group [-CH_2-$P(O)(OH)_2$] increases the water exchange rate significantly, due to sreric crowding around the water binding site (Gd**4**) . Replacing more acetate arms with methylenephosphonate groups will prevent the inner sphere water from coordinating to the lanthanide.[62,63] On the other hand, replacing an acetate side arm of DOTA with an amide group slows down the water exchange rate significantly. The substitution of an amide for a carboxylate decrease the water exchange rate about 3-4 fold.[64] The amide coordinating sidearm slows down the water exchange rate because the neutral coordinating oxygen can donate less electron density to the central lanthanide ion compared with the negatively charged carboxylate oxygen. In other words, the amide neutral oxygen creates a weaker ligand field around the lanthanide ion than the negatively charged carboxylate. [23]

Since the tropone sidearm has a neutral oxygen donor atom, we anticipated that this would have a decelerating effect on the exchange compared to a negatively charged carboxylate coordinating group. The neutral amide group has an analogous water exchange decelerating effect relative to the negatively charged carboxylate coordinating group. The water exchange rate was measured by variable temperature ^{17}O NMR measurements, (table2.3). [126] The technique is based on measuring the temperature dependence of the ^{17}O NMR transverse relaxation rate ($1/T_2$) of the bulk water, which is in exchange with the metal bound water molecule.[65]

Fitting of the data to the equations as described in the experimental section revealed that the exchange rate of the inner sphere water molecule in Gd**1** was about 2 times slower than that in the parent complex GdDOTA. The exchange rate was even slower for the positively charged

Gd**2** with two neutral oxygen donor groups but Gd**3** has shown faster water exchange rate than Gd**1** likely due to the electron donating effect of the isopropyl group (Figure 2.14).

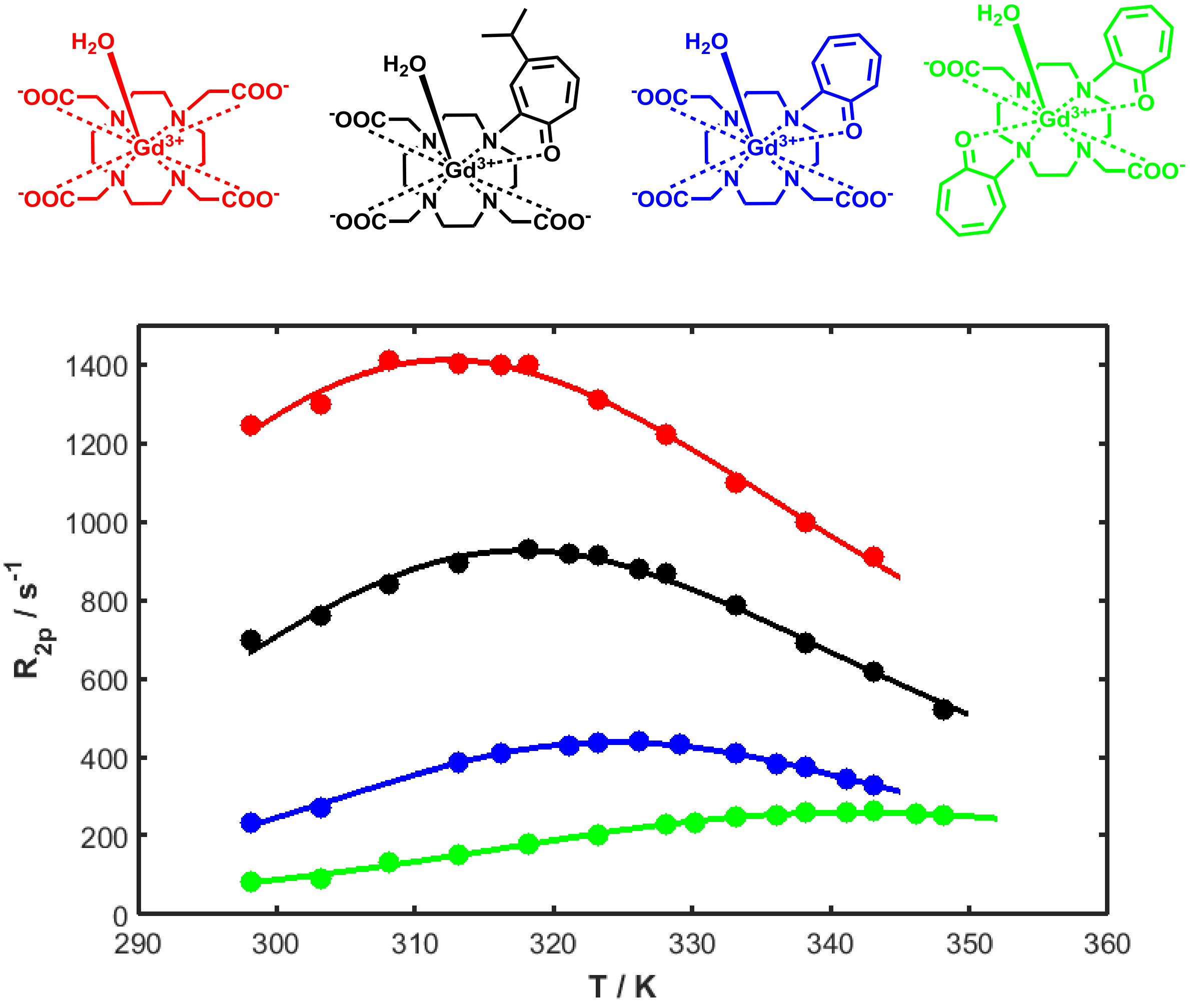

Figure 2.14. Temperature dependence of the ^{17}O NMR linewidth (points) of the bulk water of a Gd[DOTA] (red), Gd**3** (black) Gd**1** (blue) and Gd**2** (green) solution in H_2O containing 2 % $H_2{}^{17}O$ at 9.4 T. The lines represent the best fit obtained using nonlinear least-squares fitting in MATLAB.

Table 2.3. Fitting results of the water exchange rates for GdDOTA , Gd**3**, Gd**1** and Gd**2** at 9.4 T in 2 % ^{17}O water. The water lifetime, τ_m, and the activation enthalpy of the exchange, $\Delta H_{m,}$ was varied. The estimated fitting error is below 20 % in all fitted parameters.

Parameters	**q**	**k_{ex} (s^{-1})**	**τ_M^{298} (ns)**	**ΔH_M (J mol^{-1})**	**Refrences**
GdDOTA	1	4.1×10^6	244	49000	Ref.[23,67]
Gd3	1	3.17×10^6	320	34325	This work
Gd1	0.8	2.01×10^6	500	39461	This work
Gd2	0.8	1.12×10^6	890	35301	This work

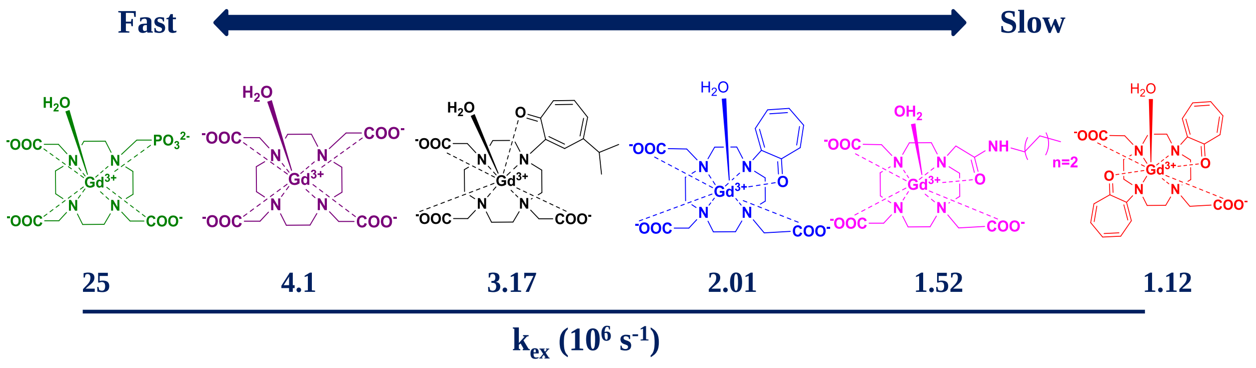

Figure 2.15.The effect of the tropone sidearm on the water exchange rate of lanthanide complexes in DOTA based ligands in comparison to other coordinating groups.

While these exchange rates are slower than optimal, they did not affect the r_1 considerably because they are still in the range where the relaxivity is limited by the short rotational correlation time of the complex.[66] In comparison to other coordinating groups, the tropone sidearm have a water exchange slowing effect similar to, but somewhat weaker than the amide group and it nicely fills the gap between the acetate and the amide (Figure 2.15).

Thus, the tropone sidearm could be used to fine tune the water exchange rate of a lanthanide complex for applications where slow water exchange is preferred (e. g. paraCEST).

2.4.5 Relaxivity in Presence of Human Serum Albumin (HSA)

Human serum albumin (HSA) is the most abundant blood protein (0.6 mM) with multiple binding sites which is providing a depot for different substrates. Binding to HSA is also important factor for developing MRI contrast agents. Generally, albumin binding increase the lifetime of the complexes in the blood pool, and could retain the contrast agent in blood pool longer to provide enough time period and allows radiologist to obtain multiple imaging. It is well known that a variety of substrates compounds can bind to HSA via site I and II (Sudlow's sites) on the protein. Site II preferred mostly by the aromatic carboxylates. The location of the HSA binding sites can be determined by using fluorescent probes such as dansyl-L-asparagine and dansylsacrosine, which bind to Sudlow's site I and II, respectively.[68] Metal complexes with aromatic groups can also interact with albumin. When a paramagnetic substrate interacts with a protein the relaxation rate of the bulk solvent protons is increased due to the slower rotation of the paramagnetic complex. Assuming that the complex binds to only one site, the association and dissociation constants are defined as shown below:

$$\mathrm{HSA} + \mathrm{GdL} \rightleftharpoons \mathrm{HSA\text{-}GdL}$$

$$K_A = 1/K_D = \frac{[\mathrm{HSA\text{-}GdL}]}{[\mathrm{HSA}]\,[\mathrm{GdL}]}$$

This relaxometric technique is commonly used to determine the thermodynamic binding constants ($K_D = 1/K_A$) of Gd^{3+} complexes to HSA as well as to other proteins. [69]

MS-325 (Vasovist, Ablavar) is a Gd-complex that binds to albumin and it is a clinically approved blood pool contrast agent for MR angiography. [70] MS-325 shows strong binding to human serum albumin (HSA) in plasma via site II with a dissociation constant (K_D) of around 100 µM. The relaxivity of MS-325 increases 8-fold in the presence of HSA vs. without HSA.[71,72] The reversible binding restricts the agent to the intravascular space (blood pool), causes a significant increase in relaxivity due to the slowing down of the tumbling rate and produces high quality angiographic images.

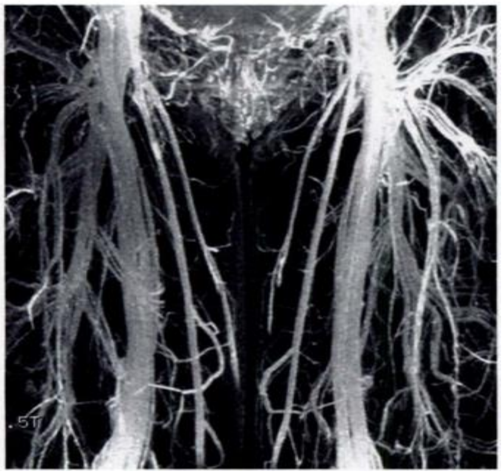

Figure 2.16. Peripheral vascular enhancement in the thighs of a healthy volunteer. The image was recorded at 1.5 T using a gradient echo pulse sequence. The dose of the agent was 0.05 mmol/kg.Ref. 70.

We anticipated that the tropone derivatives might also bind to albumin because of the presence of the lipophilic tropone moiety. Therefore, the binding of Gd**1,** Gd**2** and Gd**3** to albumin was studied by adding increasing amounts of albumin to the complex and measuring the proton relaxation enhancement (PRE) of the solution. [126]

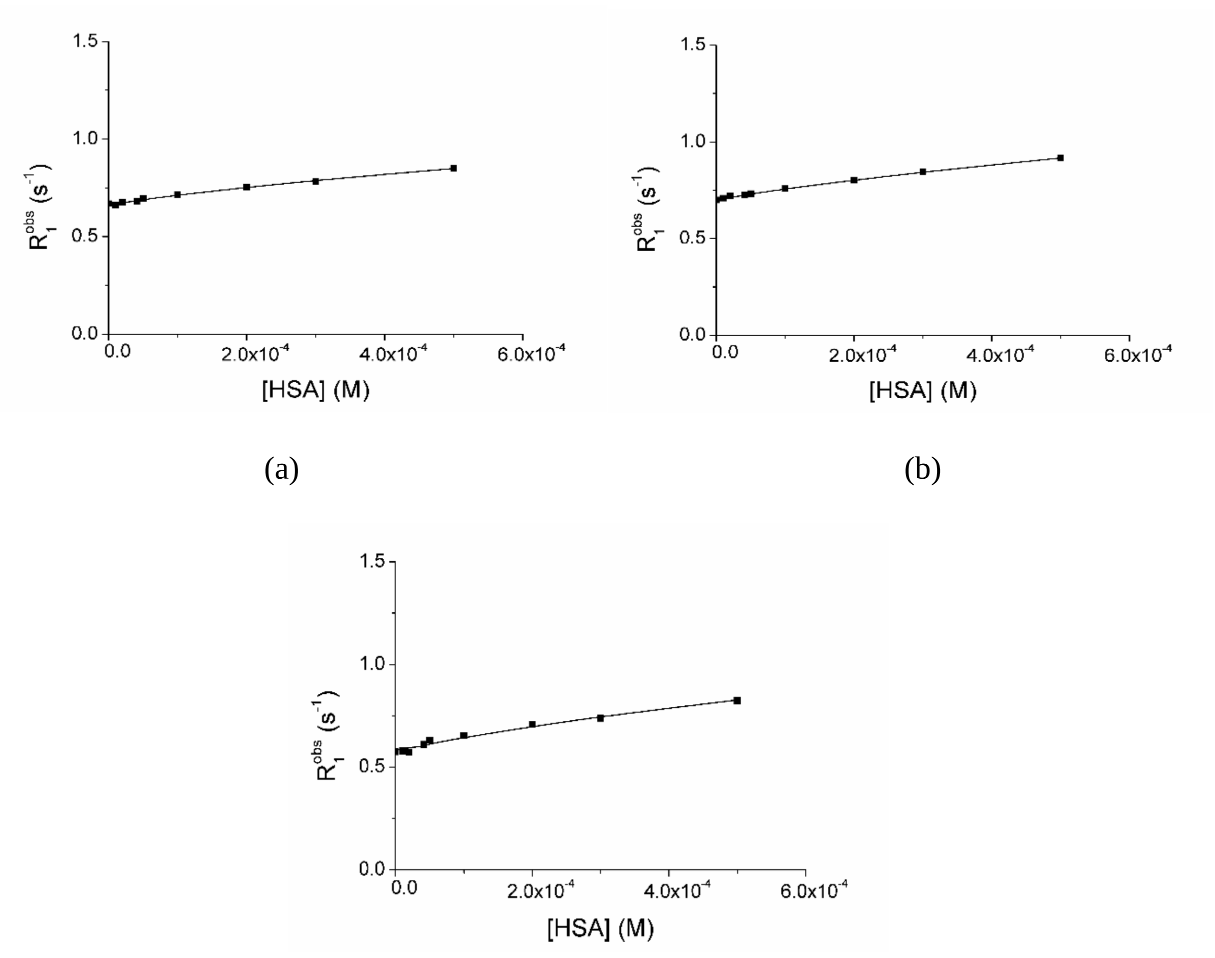

(a)

(b)

(c)

Figure 2.17. Proton relaxation enhancement data to assess HSA binding of (a) Gd**1**, (b) Gd**2**, and (c) Gd**3** complexes: E-titration technique at 0.1 mM Gd-complex (0.47T, 310 K, pH 7.4) as a function of increasing [HSA].

Table 2.4. Parameters obtained from relaxometric titrations of Gd-complexes with human serum albumin (0.47 T, 310 K).

Complex	**K_D (mM)**	**n**	**r_1^c (s^{-1} mM^{-1})**	**r_1^f (s^{-1} mM^{-1})**	**references**
Gd1	1.63 ±0.08	1	16 ± 2	3.5 ± 0.1	This work
Gd2	1.39±0.07	1	14 ±2	3.4±0.1	This work
Gd3	1.29±0.08	1	15±2	4.0±0.1	This work
Gd(BOPTA) **Multihance**	0.667	1	43	5.2	[39,44]
Gd(EOB-DTPA) **Primovist/Eovist**	0.667	1	37	6.0	[73]
MS-325 **(Vasovist, Ablavar)**	0.164	1	49	5.6	[69,72]

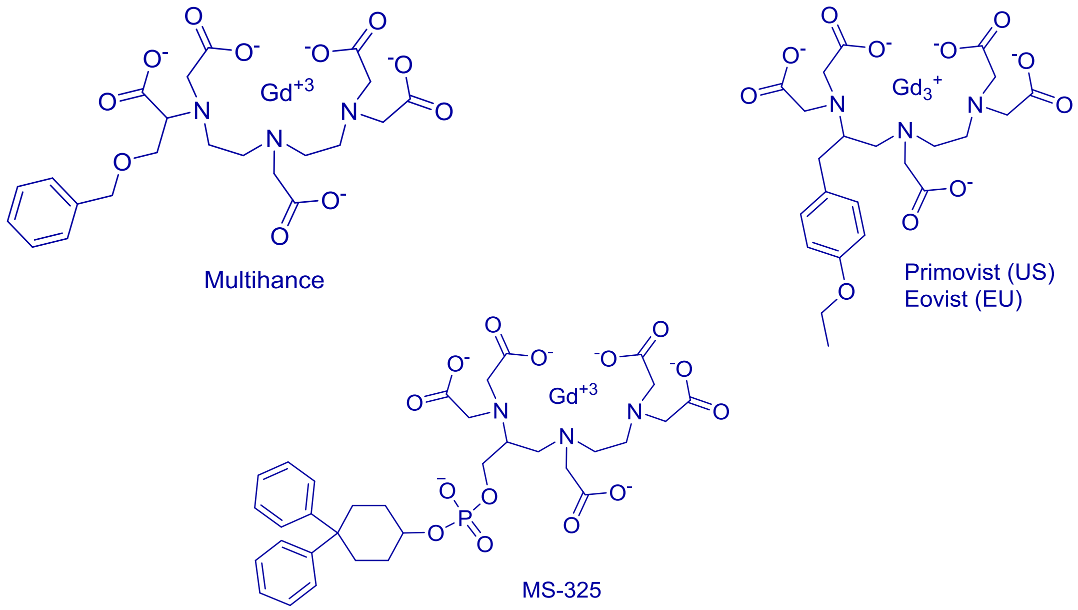

Figure 2.18. Commercially available Gd-based MRI agents that bind to HSA.

Assuming that Gd-complexes only bind to one binding site in HSA (n = 1), we were able to determine the K_D values using Equation 2.11 as described in the experimental (Table 2.4).[52] The binding of the complexes resulted in increased relaxivities as expected, but the r_1 values did not improve dramatically in the presence of albumin. Fitting of the data revealed a weak binding to HSA with a dissociation constant of K_D = 1.6, 1.4 and 1.3 mM^{-1} for Gd**1,** [126] Gd**2** and Gd**3** respectively, which does not significantly increase the r_1 value of the complex in the concentration range relevant for MR imaging. The affinity constant $K_A = 1/K_D$, obtained for all tropone complexes were about an order of magnitude lower than that of MS-325. The lower binding affinity can be explained by the fact that the aromatic tropone moiety is sterically not as available for binding to HSA as the phenyl groups of MS-325.

2.4.6 *In vivo* imaging

Paramagnetic lanthanide complexes, in particular, Gd^{3+} chelates, have made a great impact in diagnostic medicine as magnetic resonance imaging (MRI) probes. A large variety of gadolinium complexes have been synthesized and tested as MRI contrast agents. All Gd-complexes approved for clinical use are based on either the linear diethylenetriamine pentaacetic acid (DTPA) or the macrocyclic 1, 4, 7, 10- tetraazacyclodecane -1,4,7,10-tetraacetic acid (DOTA) ligand. Of these, the DOTA based complexes should be the preferred ones for in *vivo* use because they have much higher kinetic inertness and therefore, in *vivo* stability, than the linear complexes. The goal of our in *vivo* imaging studies was to demonstrate that the tropone complexes show contrast enhancement in *vivo* and, perhaps even more importantly, they do not have toxicity. In *vivo* imaging experiments were performed with the neutral Gd**1** and Gd**3** complexes but not with the positively charged Gd**2**, which is presumed to be toxic based on previous data. The complexes were administered by i.v. injection at doses usually used in MRI, ranging from 0.05 to 0.1 mmol /kg in male mice. The images (Figures 2.19 and 2.20) were acquired up to 50 min. and the animals were monitored for several days for any adverse effects. T_1-weighted imaging was performed on a 9.4T small animal imaging system using a standard gradient echo pulse sequence.

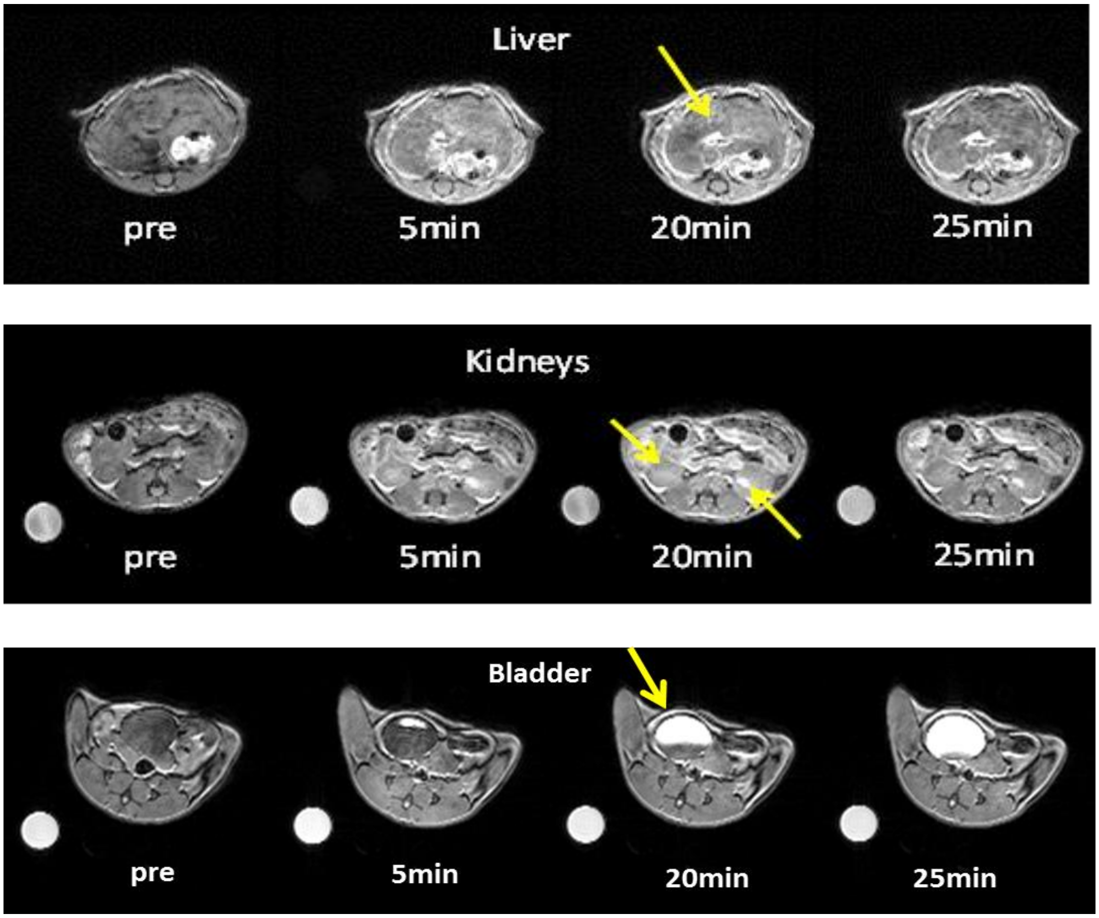

Figure 2.19. Axial T_1 weighted images of mice after injection of Gd**1** (15mM, 100μL, 0.1 mmol/kg).[126] The images show clearance by the kidneys and the liver (yellow arrows).

The following parameters were used: TR 3.6 ms, TE 1.8ms, FOV 35 × 75 ×75 mm^3, flip angle 20°, data matrix 128*128*128, 4 averages. [5,74] The images show clearance by the kidneys and the liver (yellow arrows). Interestingly, enhancement of the blood vessels in the liver is clearly visible at higher doses, likely due to the weak albumin binding of the complexes.

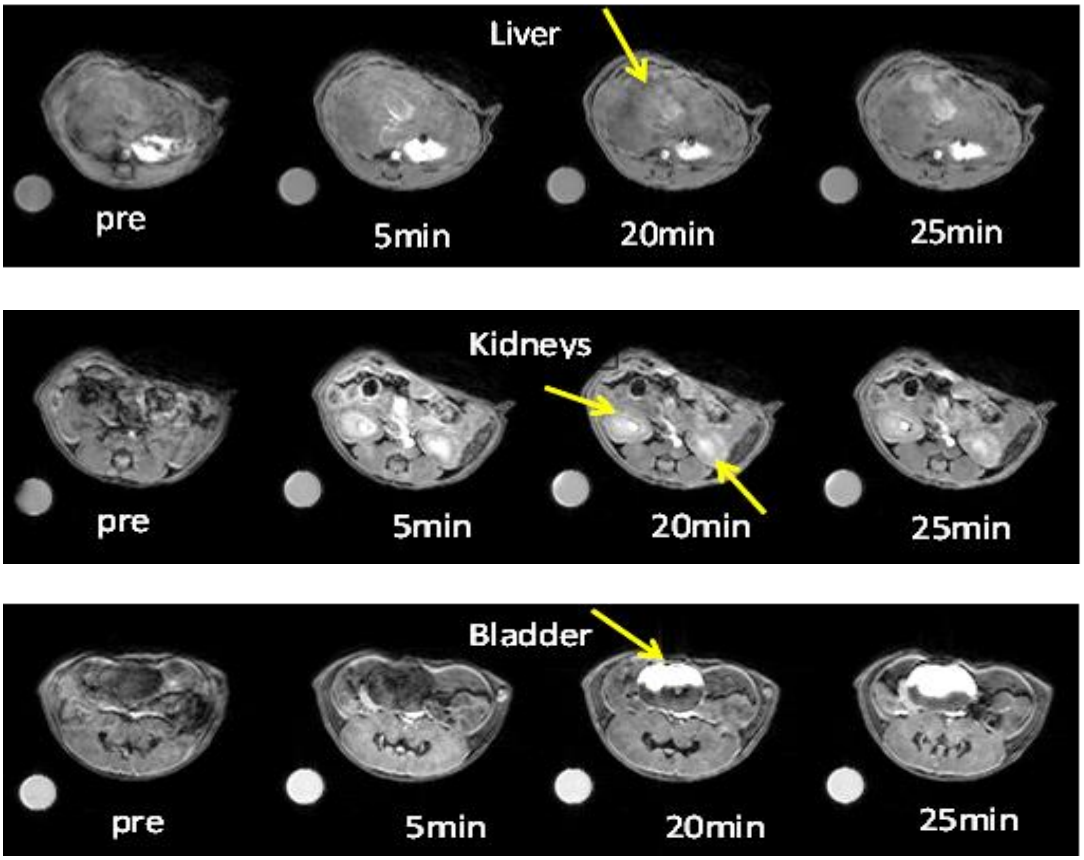

Figure 2.20. Axial T_1 weighted images of mice after injection of Gd**1** (30 mM, 100μL, 0.05 mmol/kg doses) at 9.4 T. The images show clearance by the kidneys and the liver (yellow arrows).

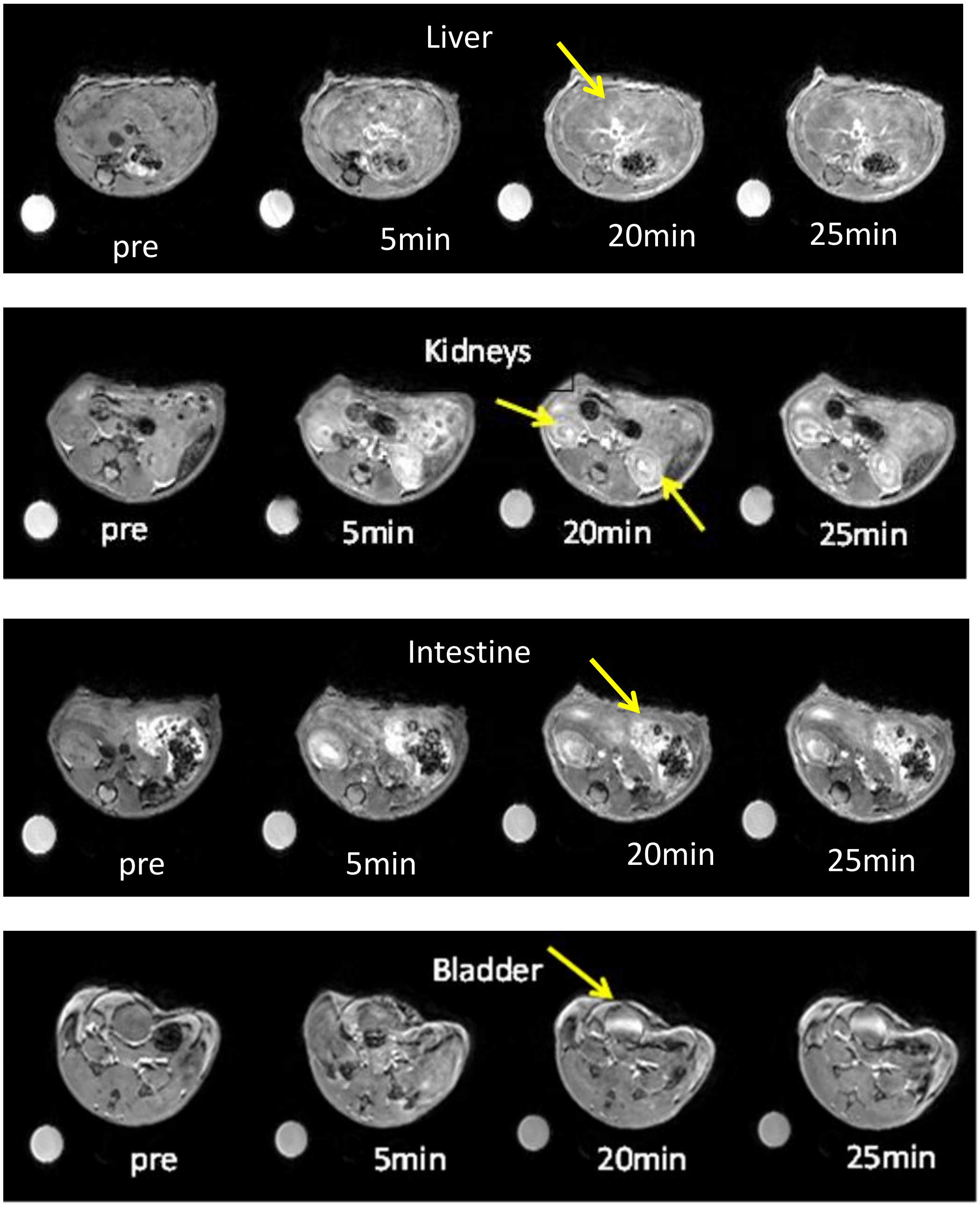

Figure 2.21. Axial T_1 weighted images of mice after injection of Gd**3** (30mM, 100µL, 0.1 mmol/kg doses) at 9.4 T. The images show clearance by the kidneys and the liver (yellow arrows).

Mass spectrometric analysis of a urine sample taken from one of the mice injected with Gd**1** indicated the presence of the intact complex in the urine. Gd**3** imaging showed more contrast enhancement compared to Gd**1** especially in the liver. The MR images show that Gd**3** did not eliminate as fast as Gd**1** [126] and also, clearance of the more lipophilic Gd**3** by hepatobiliary (by the liver, gallbladder) elimination was more prominent.

This behavior was expected because MR contrast agents with an aromatic group such as Primovist and Multihance, are known to be eliminated at least partially, by hepatobiliary excretion. [75]

2.4.7 Near Infrared (NIR) Luminescence:

The photophysical properties of the Gd^{3+}, Nd^{3+} and Yb^{3+} complexes were studied by recording the absorption, excitation and emission spectra (Figures 2.22 and 2.24).

UV-vis absorption spectra

The absorption spectra of aqueous solutions of Ln**1** and Ln**2** chelates were found to be fairly similar and display two broad bands at around 220 and 340 nm. The band at 220 nm can be assigned to the carboxylate groups while the one around 340 nm is due to the $\pi^* \leftarrow \pi$ transitions of the tropone moiety.[76]

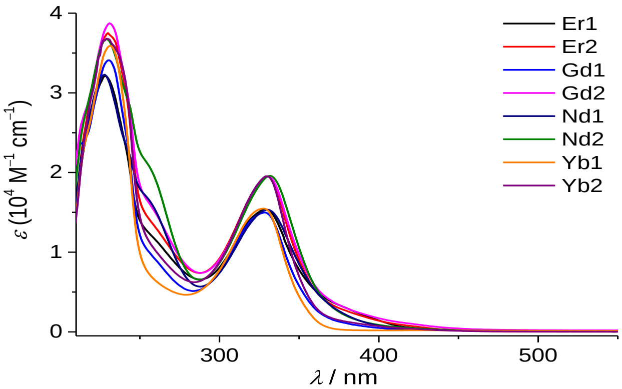

Figure 2.22. Absorption spectra of aqueous solutions of Ln**1** and Ln **2** chelates; 300 µM solutions in HEPES buffer (pH = 7.4), room temperature.

Determination of the ligand chromophore triplet state energy

The exited states of Gd^{3+} have high energies as a result of the high stability of its symmetric $^{8}S_{7/2}$ ground state. Consequently, ligand to metal energy transfer does not occur and emissions from Gd-complexes are ligand centered and appear at longer wavelengths. In these complexes the ligand centered fluorescence (emission due to $S_1 \rightarrow S_0$) is quenched by the heavy-atom and paramagnetic effect of Gd^{3+} and only phosphorescence due to the $T_1 \rightarrow S_0$ transition can be observed. The position of the chromophore triplet state can be determined from emission phosphorescence spectrum.[77] The energy position of the triplet state of the ligands was determined from the phosphorescence spectrum of their Gd^{3+} complexes (Figure 2.23).

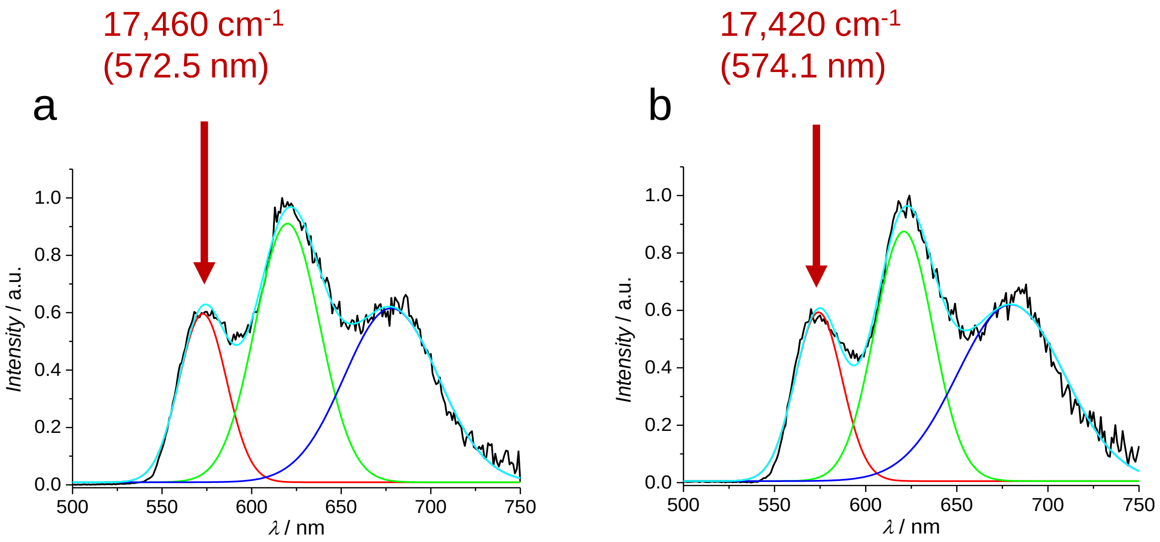
17,460 cm^{-1} (572.5 nm)

17,420 cm^{-1} (574.1 nm)

Figure 2.23. Phosphorescence spectrum (a) Gd**1,** (b) Gd**2;** under excitation at 340 nm at 77K (black trace, 300 μM, HEPES buffer (pH = 7.4) + 10% glycerol, 500 μs time delay). The two lower energy transitions due to vibronic progression are separated from the 0-0 transition by Gaussian decomposition (colored traces).

The emission displayed three maxima at 572-574, 620-621 and 678-680 nm due to vibronic progression. Gaussian decomposition of the phosphorescence spectrum allowed the determination of the position of the triplet state as a 0-0 transition at 17,460 cm^{-1} (572.5 nm) and 17,420 cm^{-1} (574.1 nm) of Gd**1** [126]and Gd**2** respectively. These values are slightly higher but still quite comparable to the reported value for tropolone, 16,800 cm^{-1}. Therefore, the energy of the triplet state is located higher than the corresponding emitting levels of E^{Nd} ($^4F_{3/2}$) = 11,460 cm^{-1}, and E^{Yb} ($^2F_{5/2}$) = 10,300 cm^{-1}, [57] which facilitates energy transfer from the ligand triplet state to the metal. [126]

Excitation and emission spectra

The excitation spectra of Yb**1**, Yb**2** and Nd**1**, Nd**2** recorded upon monitoring the main transitions at 980 and 1064 nm, respectively, displayed broad bands in the range 250-400 nm. This confirms that the sensitization of these ions occurs through the ligand-centered levels (antenna effect).[58] Upon excitation of the ligand-centered bands at 340 nm, the Yb^{3+} and Nd^{3+} complex exhibited characteristic emission in the NIR arising from the $^2F_{5/2} \rightarrow {}^2F_{7/2}$ and $^4F_{3/2} \rightarrow {}^4I_J$ (J = 9/2, 11/2, 13/2) transitions, respectively.[126]

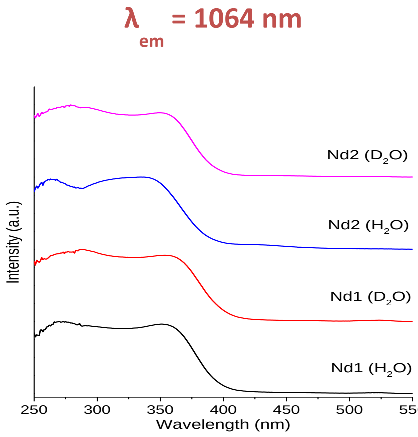

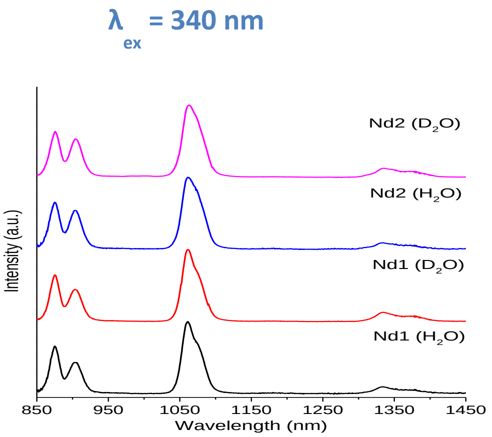

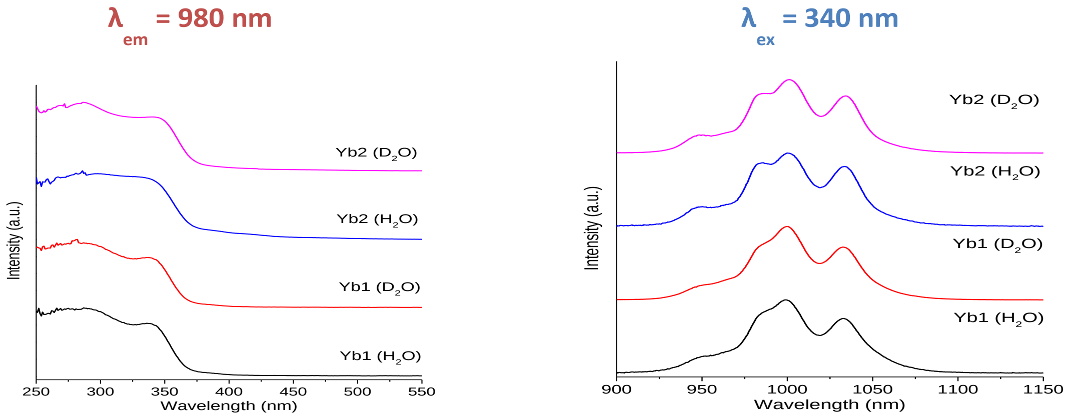

Figure 2.24. Excitation and emission spectra of the Nd (a, b) and Yb (c, d) complexes recorded in 300 µM solutions in H_2O and D_2O, at 25 °C.

Quantum yields

Quantum yield is defined as a ratio of number of photons emitted to the number of photon absorbed.[35] The quantum yield can be estimated by the equation (2.20),

$$\emptyset_x = \emptyset_s \times \left(\frac{I_{(em)_x}}{I_{(em)_s}}\right) \times \left(\frac{A_{(ex)_s}}{A_{(ex)_x}}\right) \times \left(\frac{I_{(ex)_s}}{I_{(ex)_x}}\right) \times \left(\frac{n_x}{n_s}\right)^2 \qquad (2.20)$$

where subscripts "x" and "s" represents the unknown and standard sample respectively. Φ_s , is the standard quantum yield, Φ_x is the quantum yield of the sample. I(em) is the integrated intensity of emission; A(ex) is the absorbance at excitation wavelength; I(ex) is the intensity of the excitation light; and n is the refractive index of the solution.[78] The quantum yields measured in H_2O and D_2O are summarized in Table 2.5. While these quantum yields are several orders of magnitude lower in comparison to those reported for organic fluorophores, they are fairly high for hydrated lanthanide chelates. The higher quantum yield values and longer luminescence lifetimes in D_2O indicate the higher probability of non-radiative deactivation of Ln^{3+} ions through overtones of O-H (3,600 cm^{-1}) rather than O-D (2,200 cm^{-1}) vibrations.[6]

Table 2.5. Summarized quantum yields in H_2O and D_2O.

Compound	**Solvent**	**Quantum yield (%)**	**Lifetime**	**q**
Yb1	H_2O	$6.7(2)\cdot10^{-3}$	0.864(2) µs	0.8
	D_2O	$8.29(2)\cdot10^{-2}$	7.75 µs	
Yb2	H_2O	$5.9(1)\cdot10^{-3}$	0.863(9) µs	0.8
	D_2O	$7.6(2)\cdot10^{-2}$	8.33(3) µs	
Nd1	H_2O	$5.5(2)\cdot10^{-3}$	84(2) ns	0.8
	D_2O	$2.68(1)\cdot10^{-2}$	342(2) ns	
Nd2	H_2O	$6.77(2)\cdot10^{-3}$	88(1) ns	0.8
	D_2O	$3.16(3)\cdot10^{-2}$	372(4) ns	

Determination of the number of inner sphere water molecules (q) from the luminescence decay lifetimes

Non-radiative quenching of the excited states of certain lanthanide complexes offers a very convenient way to measure the number of inner sphere molecules (q). The luminescence of these lanthanide ions decays by a vibrational energy- transfer that has several quenching sources. However, O-H oscillators present in the inner sphere water molecules have the strongest deactivating effect because quenching through coupling with O-H oscillators is strongly distance dependent (with r^{-6}). The determination of q by luminescence lifetime measurement is based on the observation that the lifetime of the excited state is shorter in H_2O than in D_2O because the O-H oscillators are over two orders of magnitude more efficient in quenching the excited state than O-D oscillators. There is a linear relationship between q and the ($k_{\text{obs,H2O}} - k_{\text{obs,D2O}}$) values, where k_{obs} (in ms^{-1} or μs^{-1}) is the luminescence decay rate constant (the inverse of the excited state lifetime τ_{obs}, in ms or μs) as shown in Equations (2.21 ,2.22 and 2.23).[35]

$$k_{\text{obs}} = 1/\tau_{\text{obs}} \tag{2.21}$$

$$\Delta k_{\text{obs}} = k_{\text{obs}}(H_2O) - k_{\text{obs}}(D_2O) \tag{2.22}$$

$$q = \text{m}\ \Delta k_{\text{obs}} - \text{C} \tag{2.23}$$

The value of empirical parameters m and C have been determined experimentally and have been reported for several lanthanide ions and they have the following values for Nd^{3+} and Yb^{3+} , Equations(2.24, 2.25 and 2.26). [76]

$$q(\text{Ln}) = \text{A}\ \Delta k_{\text{obs}} - \text{B} \tag{2.24}$$

$$q(\text{Nd}) = 130\ \Delta k_{\text{obs}} - 0.4 \tag{2.25}$$

$$q(\mathrm{Yb}) = 1.0\ \Delta k_{\mathrm{obs}} - 0.20 \qquad (2.26)$$

Where A = 130 ns for Nd^{3+} and 1.0 μs for Yb^{3+}, B = 0.2 μs^{-1}, 0.4 for Yb^{3+} and Nd^{3+} respectively; Δk_{obs} is given in ns^{-1} and μs^{-1}. The luminescence decay over time for all studied complexes (Nd**1**, Yb**1**, Nd**2** and Yb**2**) (Figure 2.25) could be best fitted by monoexponential functions reflecting the presence of only one Ln^{3+}-containing emitting species in solutions.

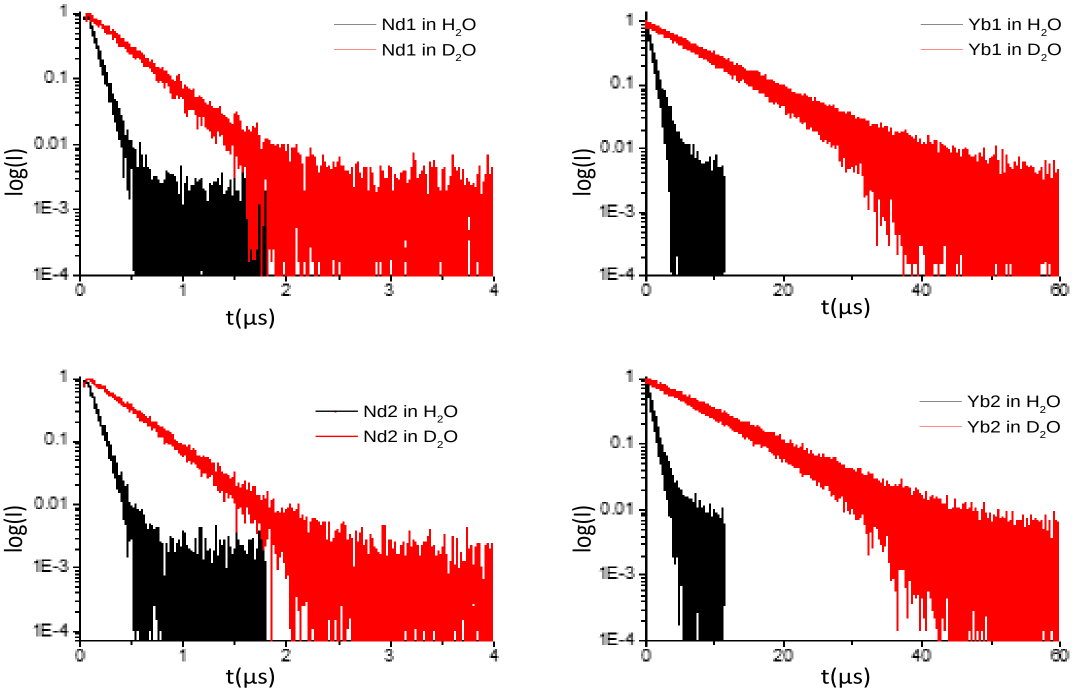

Figure 2.25. Luminescence decay curves for Nd**1** and Yb**1** (top) and Nd**2** and Yb**2** (bottom) in H_2O (black) and D_2O (red).

The fitting of the decay curves afforded the exponential time decay constant τ_{obs} excited state lifetime, Equation (2.27).

$$I_t = I_0 \exp(-t/\tau) \qquad (2.27)$$

Where I_t and I_0 are the emission intensity of the lanthanide at time t and zero respectively, and τ is a decay constant.

Comparison of τ_{obs} values obtained in H_2O and D_2O solutions and the use of the above mentioned phenomenological equations allowed the estimation of the number of inner sphere water molecules for all complexes. The value of q=0.8±0.2 was found for all these chelates, which is in good agreement with the value obtained for Gd**1** and Gd**2** by susceptibility measurements.

2.5 CONCLUSION

In conclusion, I have synthesized a novel DOTA based ligand with a tropone sidearm/s. The Ln^{3+} complexes have one inner sphere water molecule and the Gd-complexes have nearly the same r_1 value as GdDOTA. The neutral O-donor atom of the tropone moiety slows down the water exchange rate by a factor of 3 relative to GdDOTA. It is worth noting that the tropone coordinating group could therefore be used to fine tune the water exchange rate of a lanthanide complex for applications where slow water exchange is preferred (e. g. paraCEST). Photophysical measurements revealed that the tropone unit is an efficient sensitizer for the NIR emitting Nd^{3+} and Yb^{3+} allowing the detection of bright NIR emission in aqueous solutions. The excitation wavelength (340 nm) is relatively long, and more suitable for *in vivo* applications than most previously reported examples.[55] The favorable photophysical properties of the tropone chromophore combined with the DOTA framework offers a suitable platform for the design of lanthanide based bimodal MR/optical imaging agents for *in vivo* applications.

CHAPTER 3

HYPERPOLARIZED 13C-LABELED OXALOACETATE DERIVATIVES AS POTENTIAL MR PROBE FOR METABOLISM

3.1 INTRODUCTION

As discussed in Chapter 1, dramatic increases in nuclear magnetic resonance (NMR) sensitivity can be achieved by increasing the nuclear spin polarization. Hyperpolarization generally refers to methods that aim at enhancing nuclear polarization. Several experimental techniques have been proposed to increase the nuclear spin polarization and enhance NMR signal. [79] These include the brute force method, optical pumping, parahydrogen induced polarization and dynamic nuclear polarization. The brute force method is a direct approach and is based on the fact that the thermal equilibrium polarization increases with decreasing temperature and increasing external magnetic field (Equation 1.6). This is, however, impractical as the sample has to be kept at temperatures below 4K in very strong magnetic fields for an extended period of time. Optical pumping is limited to the hyperpolarization of some inert gas nuclei such as ^{3}He and ^{129}Xe, which are then used for lung imaging. Parahydrogen induced polarization (PHIP) involves the addition of para-H_2 to an unsaturated organic molecule using a catalyst and converting the spin order of the parahydrogen molecule into ^{1}H nuclear polarization followed by the transfer of polarization from ^{1}H to ^{13}C nuclei present in the substrate. The applicability of PHIP is limited by the specific chemistry involving the addition of H_2 to unsaturated compounds. On the other hand, dynamic nuclear polarization (DNP) is quite general and can be applied for any magnetically active nuclei provided that they have sufficiently long longitudinal (spin lattice) relaxation time. DNP is a phenomenon based on transferring electron polarization to nuclei via microwave irradiation of the electron spins, which results in dramatically enhanced NMR signal. In 1953, Albert Overhauser was the first one who predicted the effect in metals by the saturation of electron spin resonance (ESR) line of conducting electrons .[80] The Overhauser effect was experimentally verified by Carver and Slichter in 1956. [81] Soon after that, DNP effect in non-conducting materials at low temperature was proposed by Jeffries and Abragam, Proctor and Goldman in the 1960s and 1970s described DNP via thermal mixing.[82,83] In 2003, Goldman and Ardenkjaer–Larsen demonstrated that compounds hyperpolarized in the solid state could be dissolved and transferred into an NMR magnet for spectrum acquisition with negligible loss of polarization. This new technique, known as liquid state DNP NMR, offers dramatically enhanced signal gains for ^{13}C and ^{15}N nuclei and over 10,000-fold increases in signal to noise ratio have been reported for certain compounds. This novel technique, known as dissolution DNP-NMR, enabled the application of hyperpolarized compounds in biomedical MRI. In dissolution DNP, the transfer of high electron polarization of nuclear spins occur at low temperature, around 1 K in a relatively strong magnetic field (3.4 T or higher). The DNP sample must be in amorphous, isotropic glass, because anisotropy destroys the electron–nuclear spin coupling in the sample that is required for DNP. Experimentally, DNP is performed by microwave irradiation of a sample doped with a small amount of paramagnetic species such as stable organic free radicals or transition metal ions as free electron source. The optimal microwave frequency is near the electron paramagnetic resonance (EPR) of the paramagnetic species and depends on the mechanism involved in the polarization transfer. The glassing matrix is usually a mixture of glycerol or dimethyl sulfoxide (DMSO) with water.[84]

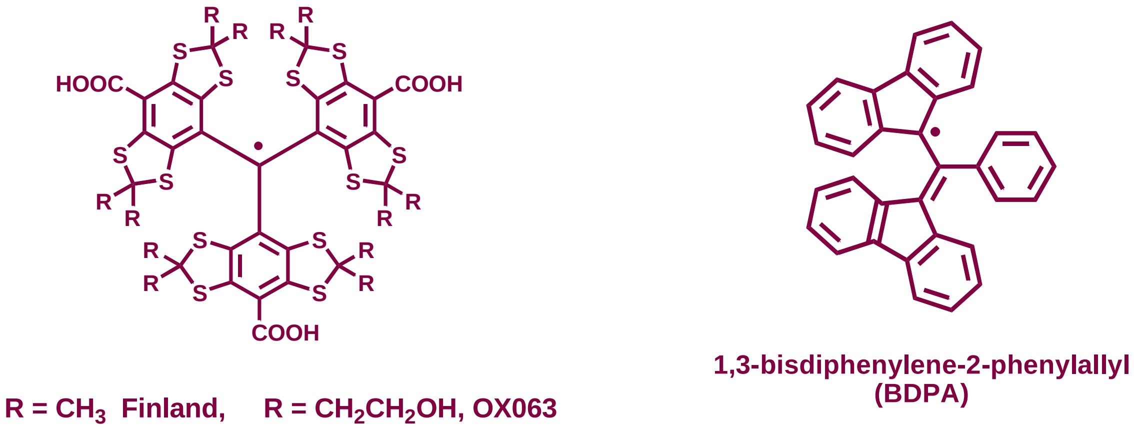

R = CH_3 Finland, R = CH_2CH_2OH, OX063

1,3-bisdiphenylene-2-phenylallyl (BDPA)

Figure 3.1. Paramagnetic species used as DNP polarizing agents. Ref. 84, 85.

3.1.1 The mechanism of dynamic nuclear polarization (DNP)

Dynamic nuclear polarization (DNP) refers to the transfer of electron spin polarization to nuclear spins. At low temperatures (around 1K) in moderately strong magnetic fields (3T), nuclear spin polarization is still negligible while the electron spins are highly polarized due to the higher gyromagnetic ratio of the electron. Microwave irradiation of samples containing trace amounts of paramagnetic species (organic free radicals or paramagnetic metal complexes) near the electron resonance frequency transfers the polarization from the electrons to coupled nuclear spins in the solid state. Since the spin lattice relaxation of the electron is much faster than that of the nuclei, under DNP conditions a single electron can polarize several nuclei. The transfer of polarization can occur by different mechanisms depending on the temperature and ESR properties of the free radical. Very briefly, the solid effect involves one electron and one nuclear spin and arises from the microwave excitation of the forbidden transitions involving both spins simultaneously.[86] Since the transitions are forbidden, the solid effect has a strong dependence upon the incident power of the microwave source.

Thermal mixing [87] is an energy exchange process between the electron Zeeman, the electron dipole-dipole and the nuclear Zeeman reservoirs.[88,89] At thermal equilibrium, the spin temperature of the electron dipole-dipole (T_{SS}), the electron (T_{EZ}) and the nuclear Zeeman (T_{NZ}) reservoirs is equal to the lattice temperature. [90] Off center irradiation on the side of the ESR line drives the electron dipole-dipole transitions and cools the electron dipole-dipole reservoir relative to the lattice, resulting in a highly polarized electron reservoir. When the ESR linewidth is comparable to the nuclear Larmor frequency, the electron dipole-dipole reservoir is thermally coupled to the nuclear Zeeman reservoir, and energy transfer occurs between them. As a result, the spin temperature of the nuclear Zeeman reservoir (T_{NZ}) will be equal with T_{SS}, leading to enhanced nuclear spin polarization. This process depends upon the allowed electron-electron dipolar flip-flops, and can therefore be of very high efficiency at higher magnetic fields where the solid effect begins to fail. Maximum positive and negative enhancements are achieved at $\omega_e \pm \omega_{1/2}$ where $\omega_{1/2}$ is the ESR linewidth.

The cross effect involves two coupled unpaired electrons with different EPR frequency (ω_{e1} and ω_{e2}, respectively) for which ω_{e2}-ω_{e1} = ω_n holds.[22,91] When the microwave radiation flips the electron spin at ω_{e1} that is coupled to the other electron at ω_{e2} a nuclear spin flip takes place simultaneously with the spin flip of the second electron. The matching frequency difference can be achieved through random orientation of spin packets of the same free radical with inhomogenously broadened EPR line or with two different radicals that satisfy the matching frequency difference requirement.

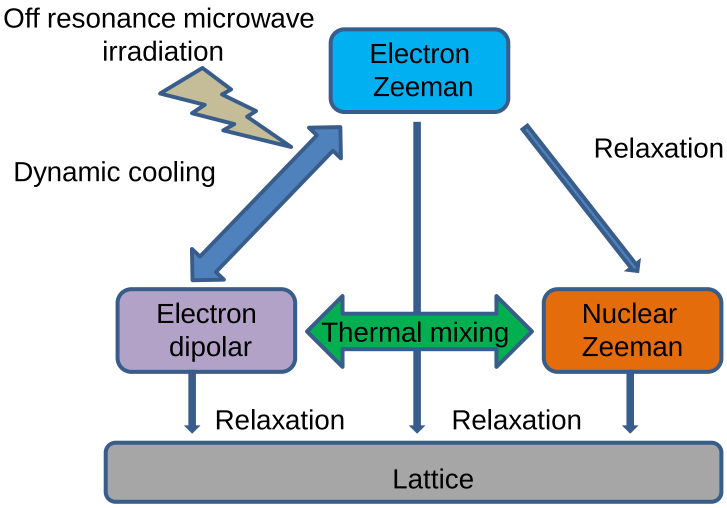

Figure 3.2. Mechanism of DNP at 1.4 K and 3.35 T.

Both the thermal mixing and the cross effect are based on the excitation of allowed electron-electron-nucleus three spin processes of EPR and therefore more efficient for DNP than the solid effect. The efficiency of these three-spin transitions depends primarily on the magnitude of the electron-electron dipolar and electron nuclear coupling and the population of the electrons that satisfy the matching frequency difference requirement. The relative size of the nuclear Larmor frequency and EPR linewidth will largely determine the mechanism of DNP. When the Larmor frequency is larger than the linewidth then the excitation of the forbidden one electron-one nucleus transitions is possible and the dominating mechanism of DNP is the solid effect. When the EPR linewidth is equal or larger than the Larmor frequency, thermal mixing or/and the cross effect dominates. Under the experimental conditions of the HyperSense commercial dissolution DNP polarizer (1 K, isotropic matrix, 3.3 T field), the dominant mechanism for DNP of ^{13}C

nuclei is hermal mixing when carbon centered organic free radicals are used as polarizing agents.[22]

Figure 3.3. Commercially available HyperSense DNP polarizer at UTSW.

3.1.2 The effect of nuclear spin-lattice (T_1) relaxation on polarization

The built up polarization of ^{13}C nuclei will decay according to the T_1 value of the nucleus. Under DNP conditions (at temperatures less than 4K) the T_1 relaxation times of ^{13}C nuclei are extremely long, on the order of 10,000 s or more. The free radical concentration has a significant effect on the T_1, as it has been shown that the T_1 value of ^{13}C labeled urea is 28,200 s and 15,800 s the presence of 15mmol/l and 20 mmol/l of trityl radical, respectively. [85] In solution at ambient temperature, the ^{13}C T_1 values in small organic compounds range from a few seconds to ~1 minute and one can anticipate having a detectable ^{13}C signal for ~5T_1 or a maximum of 5 minutes. The structural position of the ^{13}C label and the molecular weight will largely determine the relaxation rate of the ^{13}C nucleus. Dipolar relaxation through attached protons provides a very efficient pathway for relaxation.[85]

3.1.3 The dependence of polarization build-up on microwave frequency, power, temperature and free radical concentration

As already discussed, the optimal microwave irradiation frequency depends on the mechanism of DNP process. Generally, for ^{13}C enriched compounds, the enhancement curves and optimal frequencies for the maximum positive and negative enhancement indicate that the dominating mechanism for ^{13}C DNP is thermal mixing when trityl radicals are used. It has been shown that the ^{13}C saturation polarization increases with increasing microwave power until 60mW and then reaches a plateau and higher power has no effect on the final polarization enhancement. As expected, temperature has a very profound effect on both the saturation polarization and rate of polarization build-up. A decrease from 4K to 1.4K results in an almost fourfold increase in polarization. At a given temperature, higher radical concentration results in a faster buildup rate but a lower final polarization enhancement probably due to the relaxation effect of the paramagnetic radical.

3.1.4 The HyperSense DNP polarizer

The DNP polarizer is a modified high resolution, narrow bore 7T magnet charged to 3.35T and integrated with a variable temperature insert (VTI) and a microwave source (200mW maximum power at 94GHz with a tuning range of 500MHz and a frequency modulation bandwidth of 10kHz). The sample is cooled to 1.2K in a pumped helium bath and the microwave irradiation is turned on. When the desired polarization is reached, the irradiation is turned off and hot water or methanol is injected into the sample holder and the solution is transferred into the bore of a 51 mm vertical bore 400 MHz NMR spectrometer for spectrum acquisition with negligible loss of polarization. Detailed descriptions of the HyperSense DNP polarizer and similar instruments have been published.[102]

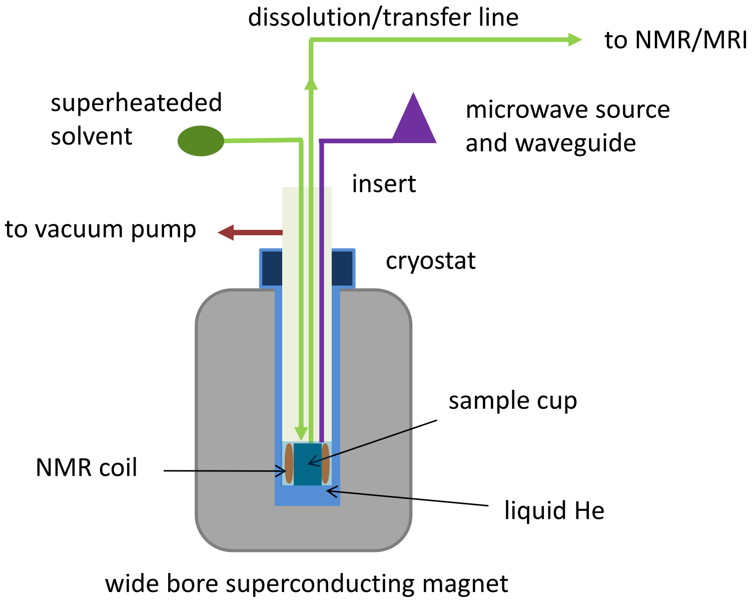

Figure 3.4. The structure of dissolution DNP polarizers.

The sample preparation requires special attention. Both the substrate molecule and the free radical must be soluble in the glassing agent. The sample is dissolved in a solvent that acts as a glassing agent, doped with the free radical to a final concentration between 10 and 40 mM depending on the radical. About 50 to 150 µL aliqot of the sample is then placed into the hyperpolarizer at temperature about 1.4 K and irradiated with microwaves (100 mV) at a frequency near the ESR frequency (94.17 GHz at 3.35 T) of the radical.[85] After 2 hours of polarizing time, 4 mL of superheated water is injected into the sample holder and 4 mL of solution is transferred into a 10 mm NMR tube in a high resolution magnet via a Teflon tube with a transfer time t_{tr} of 8 s for ^{1} H and NMR spectra acquisition. The most commonly used glassing matrix is glycerol/water mixture, although other glassing agents such as DMSO/water can also be used. The glassing matrix has a strong influence on the DNP because efficient polarization transfer requires isotropic glass matrix, in which both the substrate and the free radical polarizing agent should be completely soluble. [85]

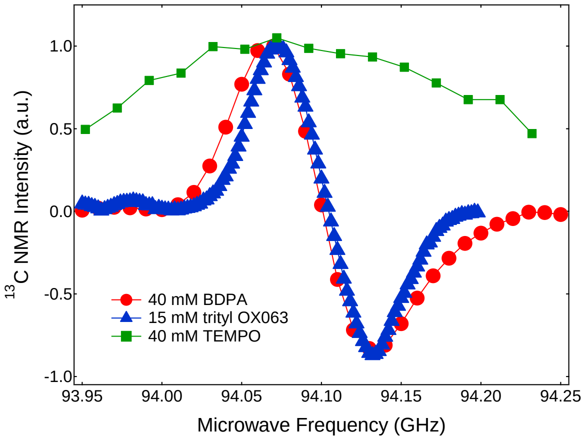

Figure 3.5. DNP spectra of different radicals recorded in the HyperSense polarizer (40mL aliquots of 1:1 [1-^{13}C] pyruvic acid: sulfolane glass doped with different radicals. DNP conditions: 3.35 T, 1.4 K, 100 mW microwave source. Note that for TEMPO, only the positive enhancement peak could be observed due to its wide ESR line. Reprinted with permission from Ref.85.

The optimal microwave frequency is determined for each radical by using the built in solid state NMR spectrometer of the HyperSense hyperpolarizer. This measures the solid state ^{13}C polarization of a ^{13}C enriched sample in the frequency range of 93.90-94.10 GHz in steps of 5 MHz (“microwave sweep). The nuclear polarization after sample dissolution and transfer is estimated from the integral of the obtained liquid state NMR signal by comparing it to the thermal equilibrium signal obtained from a reference sample, normally the same sample at thermal equilibrium.

3.1.5 The impact and significance of liquid state DNP NMR

NMR spectroscopy has become the most important technique for the structure determination of organic compounds. The major disadvantage of NMR is its inherently low sensitivity and DNP NMR addresses this issue by creating a non-equilibrium spin state population of the observed nuclei in the sample. [11,92,93] Liquid state DNP NMR produces dramatically enhanced signal to noise ratios for low sensitivity nuclei such as ^{13}C and ^{15}N. This enables the use of much smaller sample amounts and shorter experiment times (often a single scan) than in conventional NMR. Scientific and clinical applications of hyperpolarized ^{13}C MRS/MRI include kinetic measurements of the activity of specific metabolic pathways or single enzyme catalyzed steps with previously unavailable chemical specificity.[94]

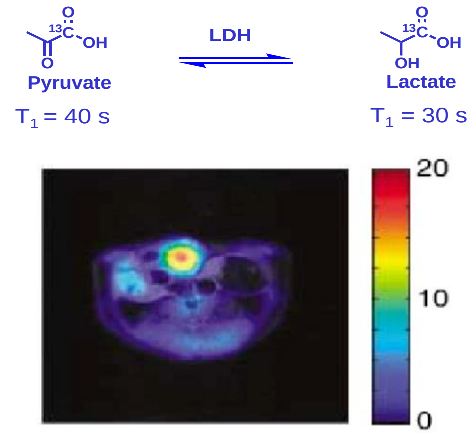

Figure 3.6. ^{13}C MR imaging of lactate pool with hyperpolarized [1-^{13}C]-pyruvate in rats with implanted P22 tumors. The tumors showed significantly higher lactate content than normal tissues. (LDH = lactate dehydrogenase). Reprinted with permission from Ref. 97.

Metabolic imaging with hyperpolarized nuclei has been applied to the detection of the distribution of a labeled substrate and all metabolites derived from this substrate. [10,95] A number of hyperpolarized ^{13}C labeled compounds have been tested in animals. Among these, [1-^{13}C] pyruvate is by far the most important, largely due to its central metabolic role and sufficiently long T_1 relaxation time of both the C1 and C2 carbons. [96] Hyperpolarized [1-^{13}C]-pyruvate has been used to highlight elevated lactate production in tumors because pyruvate rapidly exchanges into the lactate pool.[98] Hyperpolarized [1-^{13}C]-pyruvate is currently being tested in human patients for the detection of prostate cancer.[99]

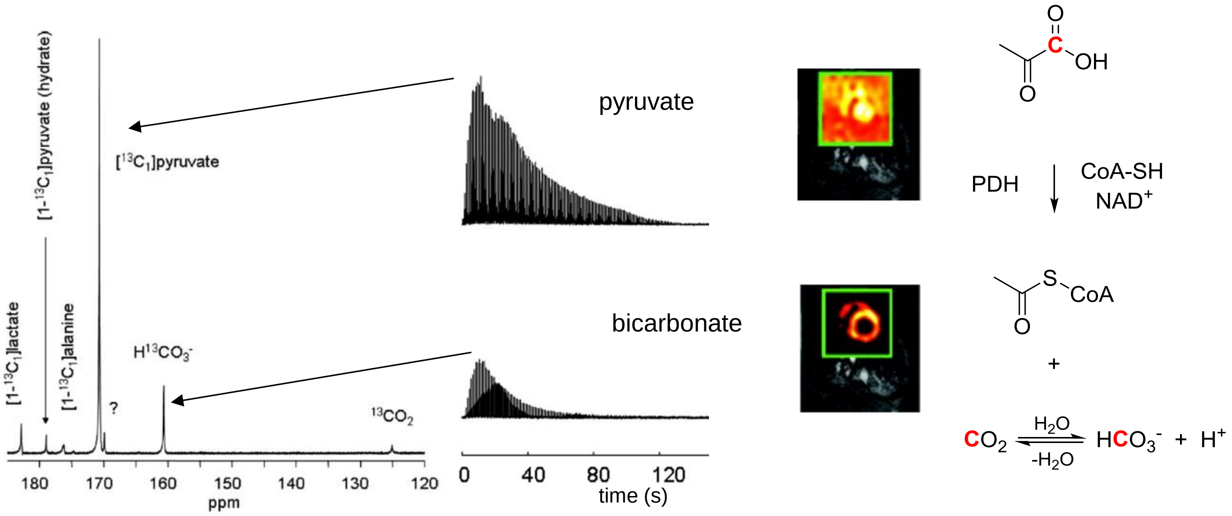

^{13}C NMR spectrum of an isolated rat heart perfused with 2 mM HP [1-^{13}C]-pyruvate

Decay of hyperpolarized ^{13}C magnetization

^{13}C chemical shift imaging of HP-[^{13}C]bicarbonate production in porcine heart muscle

Figure 3.7. Measuring mitochondrial pyruvate dehydrogenase (PDH) activity in heart muscle using hyperpolarized (HP) [1-^{13}C]-pyruvate. Flux though the PDH catalyzed step was calculated from the magnetization decay curves at 14.1 T. The production HP-[^{13}C] bicarbonate from HP pyruvate is visualized by the ^{13}C MR images recorded *in vivo*. The imaging experiments were performed at 1.5 T using a ^{13}C chemical shift imaging sequence. Reprinted with permission from Ref. 100.

Hyperpolarized substrates have been also used to measure flux through specific enzyme catalyzed pathways in tissue. For example, mitochondrial pyruvate dehydrogenase (PDH) activity was measured in heart muscle using hyperpolarized [1-^{13}C]-pyruvate (Figure 3.5). [100,101]

3.2 PROJECT GOAL

^{13}C NMR spectroscopy in combination with the use of ^{13}C-labeled tracers has been successfully applied to the study of various metabolic pathways. ^{13}C NMR isotopomer analysis relies on ^{13}C-^{13}C *J*-coupling information and labeling pattern to determine the distribution of isotopes and the metabolic fate of the labeled substrates.[103,104] ^{13}C isotopomer analysis is typically performed on tissue and organ extracts but rarely used *in vivo* because the inherently low sensitivity of NMR precludes its real time observation of ^{13}C *in vivo*. [105] In recent years, dissolution DNP NMR has revolutionized *in vivo* magnetic resonance spectroscopy and imaging as the large increases in sensitivity allows for MRS/MRI of nuclei other than ^{1}H, in particular, ^{13}C. The fate of metabolic substrates labeled in specific positions can be followed real time because the HP-signal can come only from the label; in this respect, it is analogous to positron emission tomography (PET) tracers. [92,106] However, unlike PET, MR spectroscopy allows the collection of spectral information (chemical shift), which can be used to distinguish and quantify the downstream metabolites of the hyperpolarized agent. As already discussed, hyperpolarized [1-^{13}C]-pyruvate has been widely used to study the metabolism normal and diseased tissues. The popularity of hyperpolarized pyruvate is not surprising considering its important role in many metabolic processes (Figure 3.6). [107,108]

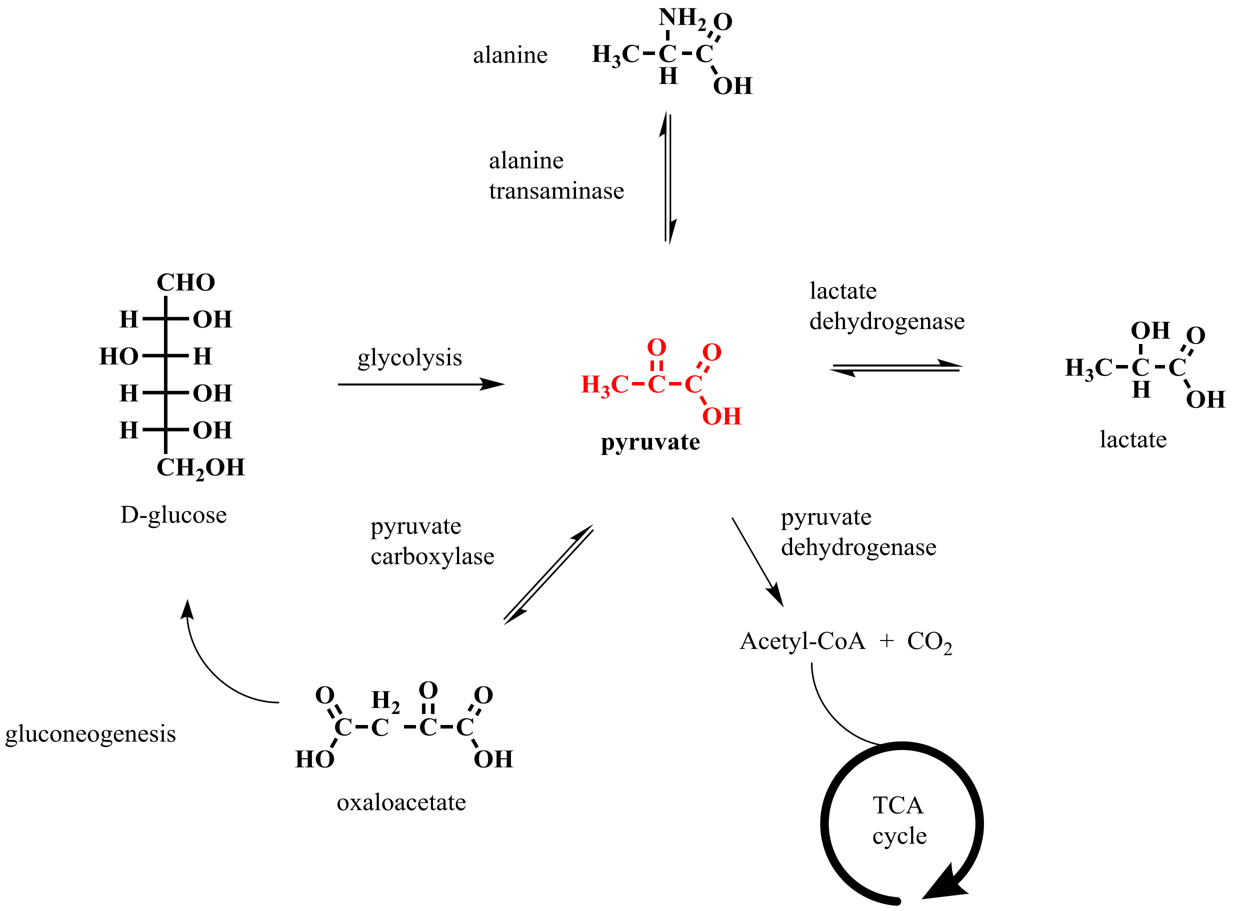

Figure 3.8. Pyruvate is involved in several important metabolic processes.

However, pyruvate is not the only metabolic intermediate that could provide useful information about important biochemical processes. These include other tricarboxylic acid (TCA) cycle intermediates such as citrate, succinate, malate and oxaloacetate. This last compound is particularly interesting because it is involved in not only the TCA cycle but also gluconeogenesis, lipogenesis and amino acid synthesis. [109]

The metabolic role of oxaloacetate

Oxaloacetate is an intermediate in tricarboxylic acid (TCA) cycle or citric acid cycle. TCA cycle is a fundamentally important metabolic pathway which connects fat, carbohydrate and amino acid metabolism. The TCA cycle essentially oxidizes acetyl-CoA originating from carbohydrates, fats, and proteins into carbon dioxide while generating reducing equivalents nicotinamide adenine dinucleotide reduced form (NADH) for the oxidative phosphorylation (ATP synthesis). It also produces four and five carbon precursors for amino acid synthesis. It is considered a cycle because the starting molecule, oxaloacetate (4 carbons), is regenerated at the end of the cycle. At the start of the cycle, acetyl CoA reacts with oxaloacetate to form citrate, a 6 carbon molecule. Citrate is transformed to isocitrate, which undergoes oxidative decarboxylation to form the five carbon α-ketoglutarate and losing a carbon dioxide. α- Ketoglutarate loses another carbon as CO_2 and yields the four carbon compound succinate. Dehydrogenation of succinate followed, by hydration of fumarate yields malate, which is then converted to oxaloacetate by malate dehydrogenase. However, these two reactions are reversible, resulting in the backward scrambling of a ^{13}C label at position 1 or 4 in oxaloacetate. [110,111] In each cycle, one acetyl group (2 carbons) enters in form of acetyl-CoA and two carbons leave as CO_2.

Oxaloacetate can be transferred from mitochondria to cytosol after reduction to malate and involved in gluconeogenesis, urea cycle, amino acid synthesis, and fatty acid synthesis. Gluconeogenesis is the de novo synthesis of glucose and it is a normal metabolic process whose main role is to maintain blood glucose levels during starvation. It consist eleven enzyme-catalyzed reactions and predominantly occurs either in liver or kidneys.[112,113] The rate of gluconeogenesis is regulated by the expression of the enzyme phosphoenolpyruvate carboxykinase (PEPCK), which is in turn influenced by insulin levels. However, compromised regulatory mechanisms of gluconeogenesis in type 2 diabetes results in the production of excess glucose and elevated blood sugar levels.[114] Phosphoenolpyruvate kinase (PEPCK) catalyzes the rate determining step of gluconeogenesis, namely, the decarboxylation and phosphorylation of oxaloacetate to form phosphoenolpyruvate (PEP).[108,115] Therefore, ^{13}C labeled oxaloacetate could potentially be used for measuring PEPCK activity. For example, the action of PEPCK on hyperpolarized oxaloacetate labeled with ^{13}C in position C4 would produce hyperpolarized CO_2/bicarbonate and therefore, would reflect metabolic flux through this enzyme. Hyperpolarized CO_2/bicarbonate easily detected at 125 and 160 ppm, respectively.

Oxaloacetate is di-anion and generally, cannot cross the cell membrane although mammalian Na+/dicarboxylate co-transporters have been identified in the kidney.[116] Monocarboxylic acids on the other hand, are rapidly transported by plasma membrane monocarboxylate transporters (MCTs). MCTs can transport a wide variety of monocarboxylates including derivatives with oxo and hydroxyl substituents on the C2 and C3 carbon. [117,118] We therefore, assumed that the monoester of oxaloacetate, specifically, the oxaloacetic acid-1-monoethyl ester, will be transported by MCTs. [119,120] We also assumed that the hydrolysis of the ester group will occur rapidly because it has already been demonstrated that carboxylesterases present in liver cells can hydrolyse ethyl esters of small carboxylic acids such as diethyl succinate and ethyl acetoacetate without significant loss of ^{13}C spin polarization. [121,122] Thus, the goal of this study was to determine whether it is feasible to use hyperpolarized ^{13}C labeled oxaloacetic acid derivatives as metabolic probes.

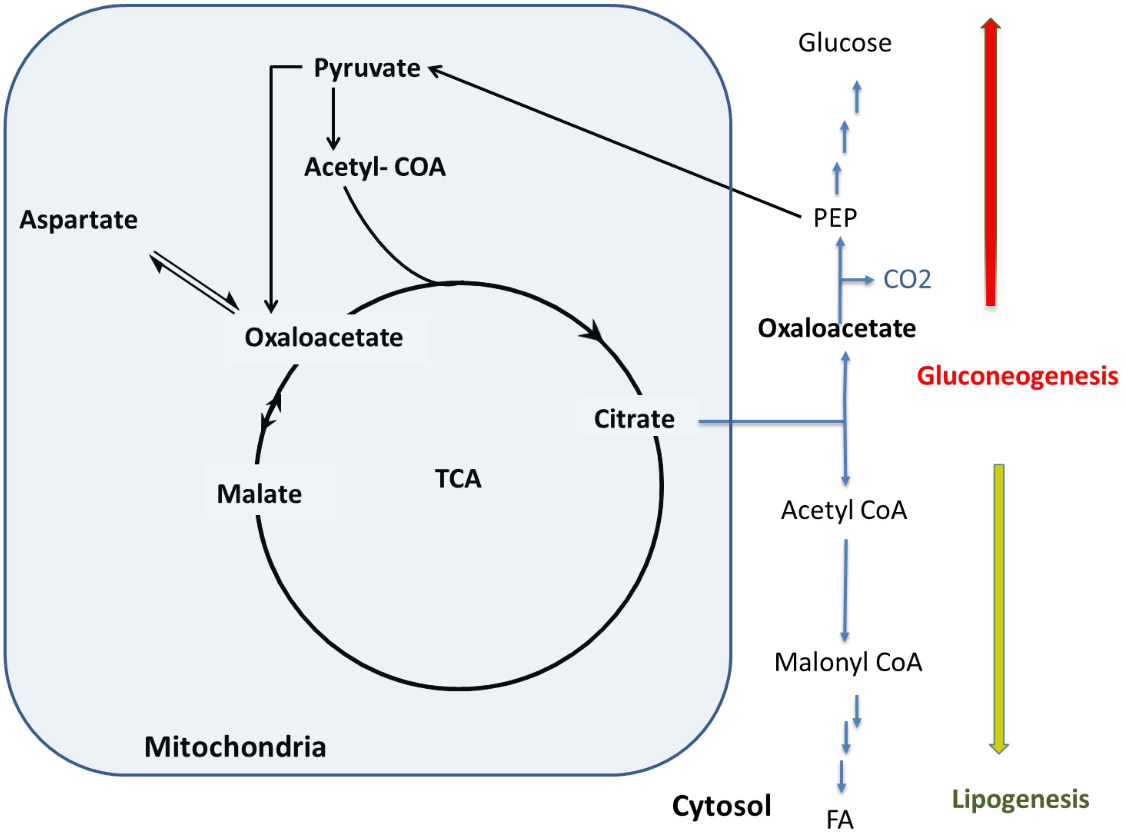

Figure 3.9. The metabolic role of oxaloacetate.

We propose [4-^{13}C]-monoethyl oxaloacetate as candidate to explore glycogenesis. In this regard, this project will be focused on the synthesis of ^{13}C labeled oxaloacetic acid derivatives. The metabolism of these derivatives will be studied in isolated, perfused liver experiments. ^{13}C DNP studies will be perfomed to measure ^{13}C NMR signal enhancement and the T_1 relation time. Finally, we will attempt to use hyperpolarized derivatives to probe gluconogenesis in real time using *in vivo* ^{13}C NMR.[111]

3.3 EXPERIMETAL

3.3.1 Synthesis

General Remarks. All solvents were obtained from commercial sources and were used without further purification. The free radical, (trityl OX063) was obtained from Oxford Instruments Molecular Biotools. The DNP was performed using an Oxford HyperSense commercial polarizer. ^{1}H NMR spectra were recorded using a Varian 9.4T NMR system.

[4-^{13}C]-diethyl oxaloacetate sodium salt (1a). This compound was prepared following a literature procedure. [128] To 21% solution of sodium ethoxide in ethanol (3.2 mL), a mixture of of diethyl oxalate (3.2 g) and ethyl [1-^{13}C]-acetate (1.8 g) was added dropwise over a period of 25 minutes in an ice bath. The mixture was stirred for 2 h. The mixture was allowed to warm up to room temperature while stirred for another hour. Then the mixture was heated to 85 ºC for 3 hours. The reaction mixture was allowed to cool to room temperature and stirred for an additional 14 h. The product separated as a yellowish precipitate. It was taken up with ethanol, filtered, washed with ethanol and ether several times and dried to a constant mass in vacuum to give the product as a white solid (2.3 g, 53%).

[4-^{13}C]-monoethyl oxaloacetate disodium salt (1). This compound was prepared following a literature procedure. [124] To the solution of 200 mg sodium hydroxide in absolute ethanol (20 mL) and water (4 mL), 1.0 g of **1a** was added to form a clear solution. The mixture was stirred overnight, over which period the product precipitated as a white solid. The product was filtered and washed with ethanol and ether several times. The solvents were removed in vacuum to give the product as a white solid (550 mg, 64%)

Hyperpolarization of [4-^{13}C]-monoethyl oxaloacetate disodium salt

[4-^{13}C]-Monoethyl oxaloacetate disodium salt was dissolved in a solvent mixture that acts as a glassing matrix (approximately 1M concentration in 1:1 glycerol-water) and doped with the trityl radical OX063 (15 mM). The sample (150 μL) was placed into the HyperSense polarizer operating at 1.4 K then irradiated with microwaves (100 mV) at a frequency near the ESR frequency (94.17 GHz at 3.35 T) of the radical. After 2 hours of polarizing time, 4 mL of superheated water was injected into the sample holder and the solution was transferred into a 10 mm NMR tube in a 9.4 T high resolution magnet via a Teflon tube. The concentration after dissolution was approximately 2mM. ^{13}C NMR spectra were recorded at 9.4 T.

3.3.2 Data analyses

The NMR data were acquired using a Varian VNMR spectrometer, and the spectra were processed using ACDLABS version 12 software (Advanced Chemistry Development, Inc., Toronto, Canada). ^{13}C spectra were collected using a non-selective 5 degree excitation with a repetition time of 5 s and a total of 21 spectra were collected (n = 1). In liver perfusion experiments the C3 lactate peak was used as reference. The graphs, fits, and data analyses were done using Graph pad prism 7.01. T_1 values were calculated by fitting NMR signal intensity as a function of time in Equation (3.1). [127]

$$M_z\,(t) = M_0\,\sin\theta\,\,(\cos\theta)^{t/T_R}\,\,e^{-t/T_1} \tag{3.1}$$

Where M_z is the magnetization of the hyperpolarized species along z axis as function of time , M_0 initial magnetization, T_1 relaxation time, θ is the flip angle and T_R the repetition time.

3.3.3 Liver perfusion

This protocol for liver perfusion is used at the Advanced Imaging Research Center of UT Southwestern. The animal protocol was approved by the Institutional Animal Care and Use Committee of UT Southwestern Medical Center. Female C57Bl/6 mice obtained from Charles River Laboratories were housed in the university vivarium on a 12 h light–dark cycle and had free access to standard lab chow and water. Mice (35-36g) were fasted overnight with free access to drinking water before the experiments. Following general anesthesia using isoflurane, the livers of adult mice were rapidly cannulated then excised. The liver was perfused through the portal vein with a modified Krebs-Henseleit (KH) buffered medium while suspended in the effluent at 37 °C and the perfusion was carried out at a constant flow rate of 5 mL/min. The perfusion medium was temperature regulated with a water jacket. Efferent and afferent pO_2 were measured with a blood gas analyzer (Instrumentation Laboratory, Lexington, MA, U.S.A.). Livers were rejected if they did not maintain a pO_2 gradient of at least 100 mmHg or if the tissue color changed during the study. The perfusion medium consisted of 118 mM NaCl, 5 mM KCl, 1.2 mM $MgSO_4$, 1.25 mM $CaCl_2$, 25 mM $NaHCO_3$, 1.2 mM KH_2PO_4 and 0.2 mM octanoate.

Isolated liver perfusion

Livers were supplied with a mixture of 2 mM [4-^{13}C]-monoethyl oxaloacetate and perfusion medium. Livers were perfused for ~30 min in a perfusion column height of 15 cm H_2O at constant flow rate of 5 mL/min. Under these conditions, livers reach steady-state ^{13}C enrichment after ~ 30 min (Hausler et al. 2006). Effluent medium was collected every 15 min to measure O_2 consumption. Livers were freeze-clamped and stored at −80 °C immediately after the NMR is done for extraction.

Liver perfusion with hyperpolarized agent

[4-^{13}C]-monoethyl oxaloacetate was polarized as described. The sample was dissolved with a superheated of KH buffer solution. After dissolution, 3 mL of the resulting solution was mixed into 20 mL of the perfusate containing the same perfusion medium (118 mM NaCl, 5 mM KCl, 1.2 mM $MgSO_4$, and 1.25 mM $CaCl_2$, 25 mM $NaHCO_3$, 1.2 mM KH_2PO_4 and 0.2 mM octanoate) and pH was adjusted to 7.4. The liver was placed in a 25 mm NMR tube and positioned in an 89 mm bore 9.4 T magnet (Agilent) equipped with a Doty 1H/13 C probe. Shimming was performed on the ^{23}Na signal. Broadband ^{1}H decoupling using WALTZ-16 was gated on during acquisition only. To facilitate shimming, a sodium-free perfusion medium was pumped through a separate line to the bottom of the NMR tube at a rate of ~5 mL/min. This flush served two purposes: (1) to remove extracellular sodium from the active volume of the probe to facilitate shimming and (2) to remove any metabolites excreted by the perfused liver. The HP ^{13}C NMR signal was collected using a series of 5° ^{13}C pulses with an acquisition time of 1s and 1s interpulse delay. The ~ 23 mL of HP material, as described, was injected by catheter into the medium directly above the cannulated liver at a rate of ~ 5 mL/min. After the injection the liver was perfuse additionally for 15min to reach to steady state. The medium was not recirculated. Livers were freeze-clamped and stored at −80 °C immediately after the NMR is done for further processing.[107,123]

3.3.4 Perchloric acid (PCA) extraction

Mortar and pestle was placed in a PVC bucket and cooled by liquid nitrogen (LN_2), and then frozen tissue was weighed and placed into LN_2. Pulverize tissue into a fine powder in the presence of LN_2. A Bunsen burner was used to heat a 10 ml glass beaker to remove all moisture. The hot beaker was weighed and cooled down to the room temperature and placed in LN2 along with the scoop end of a steel spatula. The LN_2-cooled 10-mL beaker was placed on the balance and the balance was covered to keep the balance cool. The LN_2-cooled spatula was used to transfer ~ 100 mg of pulverized tissue into the cold beaker. Transferred tissue should not have LN_2 present. The 10-mL beaker was removed from the balance and placed in a 70 °C oven for 24 hrs. After 24 hrs, the warm 10-mL beaker was weighed by the same balance at room temperature. Difference in pre-dried vs dried tissue weight is the amount of moisture lost from tissue. Perchloric acid (PCA) solution (6%) was transferred into a 15 ml centrifuge tube and kept in ice to cool down. Volume transferred should be equal to 4 × the frozen weight of the tissue. A mortar was removed from bucket and after checking that all LN_2 has evaporated, tissue was transferred into 15-mL centrifuge tube. A steel spatula was used to remove all tissue from mortar. The tube was capped and the tissue was mixed into the acid solution, uncapping periodically to allow any residual N_2 (g) to escape. Once mixed thoroughly, the centrifuge tube was placed in an ultra-centrifuge cooled to 2 °C for 15 min @ 13500 rpm. The supernatant was transferred to an ice-cold 10-mL beaker. The ice-cold solution was neutralized with KOH (aq) solution. After pH correction, the mixture was transferred to another 15-mL centrifuge tube and kept in ice for 10-15 min. The tube was centrifuged for 10 min @ 13500 rpm @ 2 °C. Once complete, the supernatant was transferred to a pre-weighed scintillation vial and placed in a freeze-dryer system overnight. An NMR spectrum was obtained.

3.4 RESULT AND DISSCUSSION

3.4.1 Synthesis

The synthesis of [4-^{13}C] monoethyl oxaloacetate disodium salt is outlined in Scheme 3.1. We have chosen the commercially available ethyl [1-^{13}C]-acetate for the synthesis of [4-^{13}C]-diethyl oxaloacetate sodium salt (1a). This reagent reacted cleanly with diethyloxalate in presence of sodium ethoxide and ethanol to give the expected sodium salt of the enolate of diethyl oxaloacetate (Scheme 3.1). The sodium ethoxide used for the condensation was freshly prepared by dissolving sodium in anhydrous ethyl alcohol. The C4 monoester was prepared by selective hydrolysis of the diester with NaOH in ethanol. The regioselectivity in this reaction likely arises from the larger separation of the negative charges in the C4 monoester enolate ion as compared to the other isomer. [124]

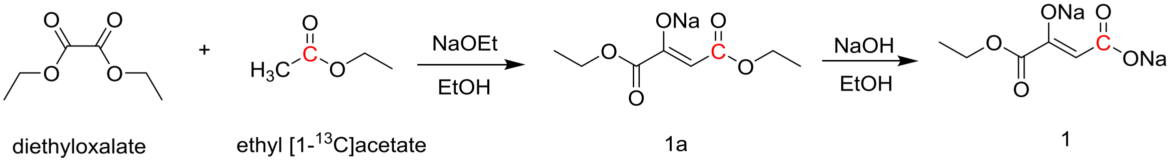

Scheme 3.1.Synthesis of [4-^{13}C] monoethyl oxaloacetate disodium salt (1).

3.4.2 Isolated, perfused liver experiments

After synthesis of the [4-^{13}C]-monoethyl oxaloacetate disodium salt, we decided to investigate the metabolic fate of this compound to establish whether the compound is taken up and metabolized by the liver. Therefore, we performed isolated, perfused mouse liver experiments. The isolated mouse livers were perfused with a perfusate containing 2mM [4-^{13}C]-monoethyl oxaloacetate, 0.2 mM octanoate and KH buffer for 30 min. The liver then was freeze-clamped and extracted with PCA to remove all enzymes and protenis for methabolic extraction. High resolution ^{13}C NMR spectroscopy at 600MHz equipped with 10mm cold probe of the PCA extracts revealed the presence of [1-^{13}C]-citrate (179.7 ppm), [4-^{13}C]-aspartate (178.5ppm) and [4-^{13}C]-malate (180.9ppm), indicating that [4-^{13}C]-monoethyl oxaloacetate can enter the cells, the ethyl ester undergoes hydrolysis and the resulting [4-^{13}C]-oxaloacetate enters the TCA cycle.

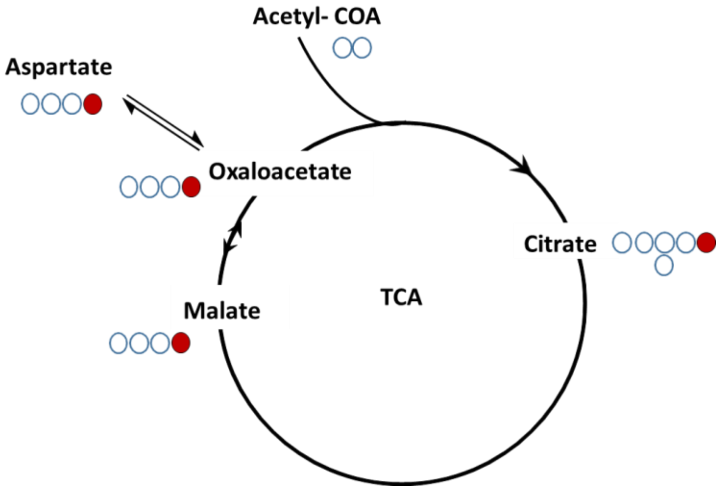

Figure 3.10. The conversion of [4-^{13}C]-monoethyl oxaloacetate to [1-^{13}C]-citrate, [4-^{13}C]-malate and [4-^{13}C]-aspartate in the TCA cycle.

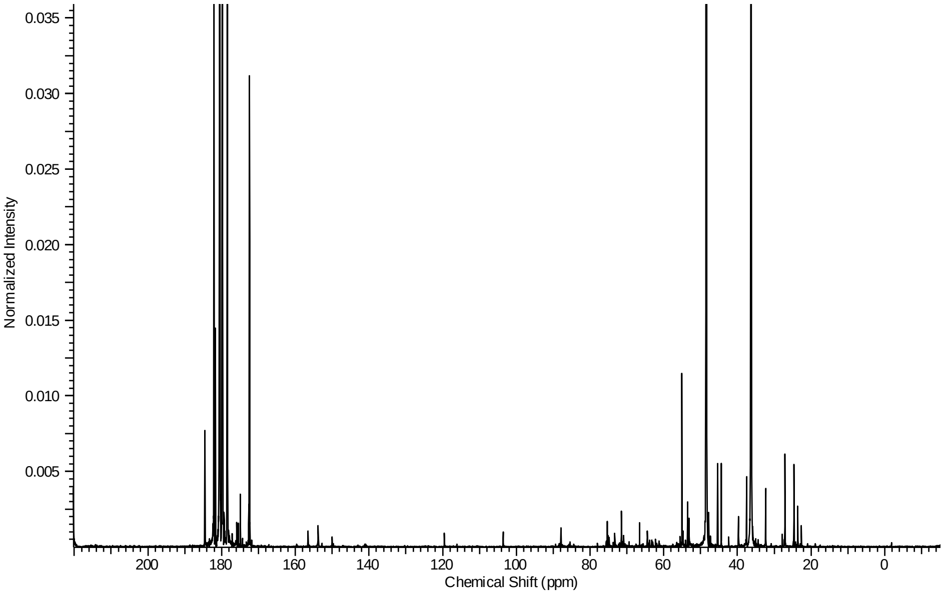

Figure 3.11. Full ^{13}C NMR spectrum at 600 MHz of a mouse liver extract after perfusion with that [4-^{13}C]-monoethyl oxaloacetate.

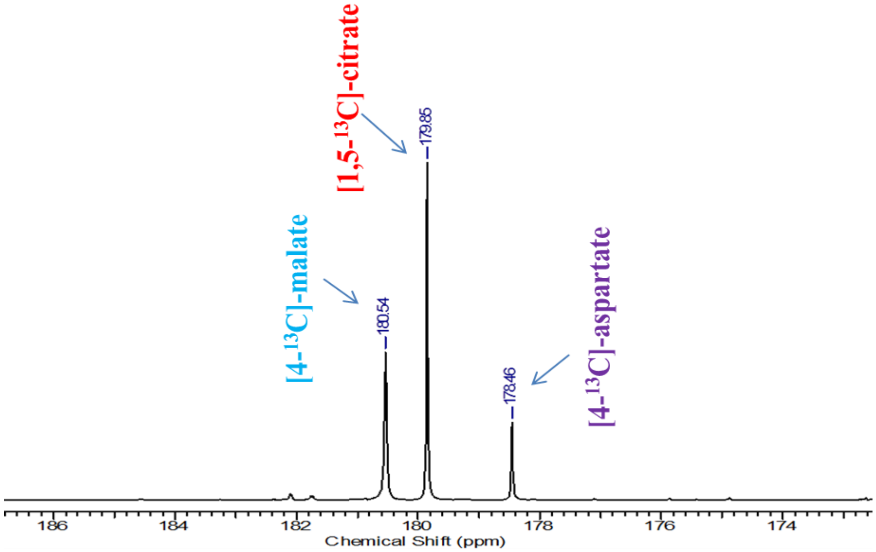

Figure 3.12. The 174 - 186 ppm region of the above ^{13}C NMR spectrum showing the metabolites of [4-^{13}C]-monoethyl oxaloacetate.

[C4-^{13}C]-Oxaloacetate was not observed, but this is not surprising because the *in vivo* pool size of oxaloacetate is very small The NMR spectrum is shown in Figure 3.9 and 3.10. The resonances were assigned by comparison of the experimental chemical shifts with a chemical shift reference database of metabolites compiled at the advanced imaging research center (AIRC). Figure 3.8 shows the metabolic fate of [4-^{13}C]-oxaloacetate in the TCA cycle.

3.4.3 *In vitro* DNP-NMR studies

The liver extract results have demonstrated that [4-^{13}C]-monoethyl oxaloacetate is taken up and metabolized in the liver. However, as discussed, the sensitivity of a conventional ^{13}C NMR experiment is not high enough to be able to detect TCA cycle metabolites *in vivo* within a reasonable time frame. Therefore, we have decided to study the real time metabolism of [4-^{13}C]-monoethyl oxaloacetate using hyperpolarized [4-^{13}C]-monoethyl oxaloacetate in perfused mouse livers. As discussed, the hyperpolarized ^{13}C magnetization decays by spin-lattice (longitudinal) relaxation and enhanced ^{13}C signal can be observed for about 3 to 5 T_1 periods. Thus, considering the time required for dissolution, transfer (around 10 s) and injection, successful in *vivo* detection of metabolites generally requires T_1 relaxation times longer than 15s. Before the in *vivo* studies we have performed in *vitro* dynamic nuclear polarization (DNP-NMR) experiments to measure the ^{13}C NMR signal enhancement and the T_1 relaxation time of the ^{13}C label in [4-^{13}C]-monoethyl oxaloacetate. The compound was polarized under standard DNP conditions in glycerol-water matrix with trityl OX063 in the HyperSense polarizer.

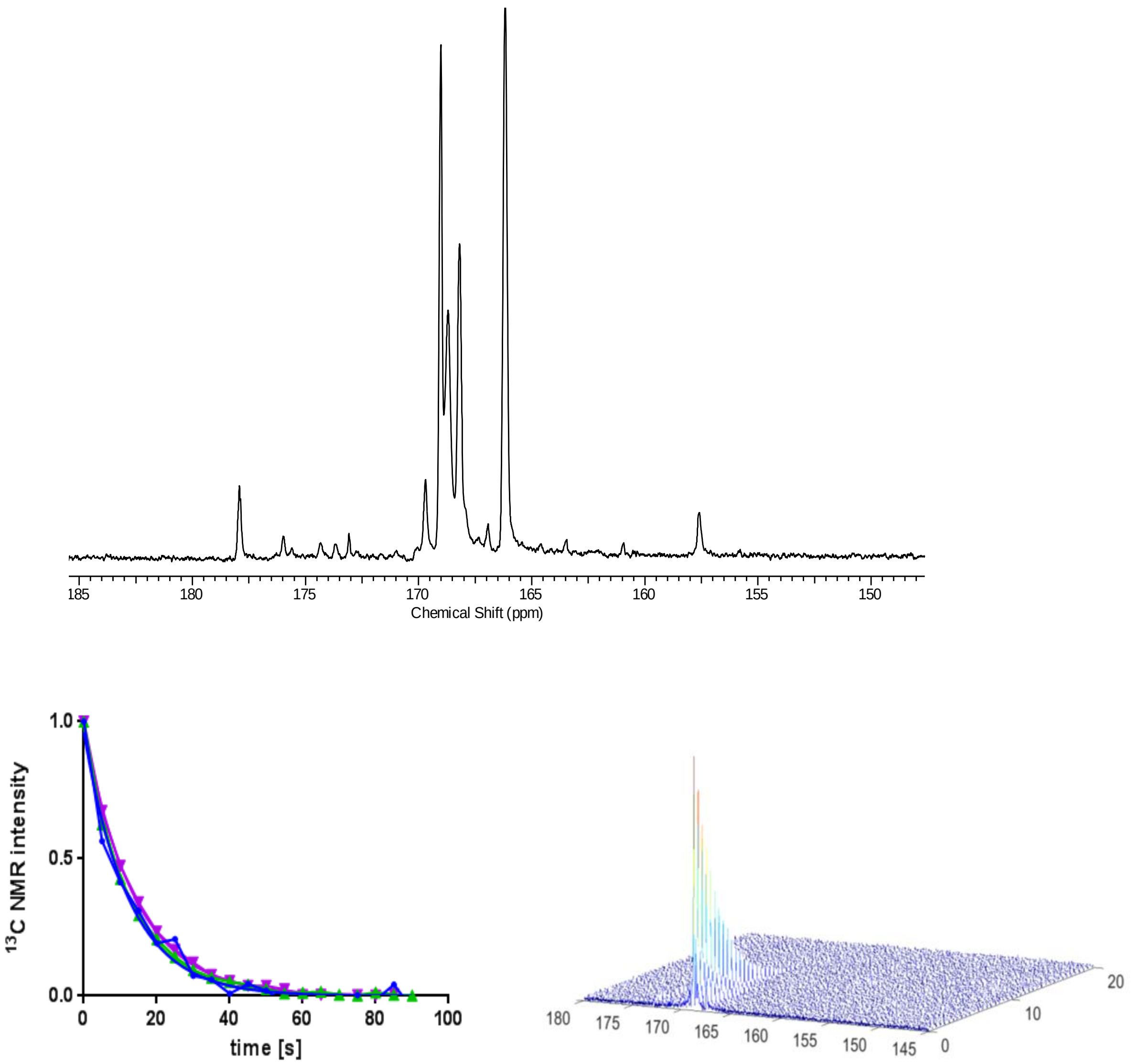

Figure 3.13. T_1 decay of hyperpolarized magnetization [4-^{13}C] monoethyl oxaloacetate disodium salt after dissolution in KH buffer. Approximately 5000-fold ^{13}C NMR signal enhancement was observed at room temperature and 9.4 T. Fitting of the decay curves gave approximately the same T_1 value, 14 s for all three peaks at 9.4 T.

^{13}C NMR spectra were recorded at 9.4 T after dissolution in water or aqueous KH buffer solution. Approximately 5000-fold ^{13}C signal enhancements at room temperature were achieved at 9.4 T. The carbonyl region in the ^{13}C NMR indicated the presence of 3 major isomers (Figure 3.11).[125] The T_1 was determined from the decay of the hyperpolarized magnetization (Figure 3.11). Unfortunately, the T_1 value was found to be only around 14s.

3.4.4 Liver perfusion experiments with hyperpolarized [4-^{13}C] monoethyl oxaloacetate disodium salt

Although the T_1 value of the C1 carboxylate was found to be short (14 s) we decided to perform hyperpolarized ^{13}C NMR spectroscopy studies with perfused livers. Isolated livers were perfused with hyperpolarized [4-^{13}C] monoethyl oxaloacetate disodium salt in the bore of a 9.4 T magnet and the metabolism of this substrate was followed real time by ^{13}C NMR spectroscopy. A sum spectrum of the carboxylate region is shown in Figure 3.12. Although the signal to noise ratio is very poor, the spectrum clearly indicates that hyperpolarized [4-^{13}C] monoethyl oxaloacetate disodium salt undergoes some transformation. Unfortunately, we were unable to unequivocally identify any metabolites from these spectra.

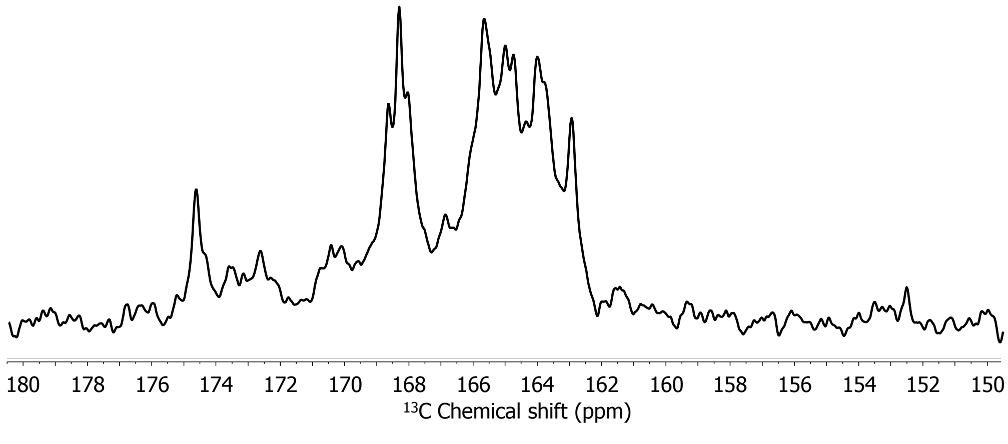

Figure 3.14. ^{13}C NMR spectrum (sum of 20 FIDs) of isolated mouse liver perfused with perfused with 0.2 mM hyperpolarized [4-^{13}C] monoethyl oxaloacetate disodium salt and 0.2 mM octanoate.

3.5 CONCLUSION

In summary, I have synthesized a ^{13}C- labeled oxaloacetate derivative, [4-^{13}C]-monoethyl oxaloacetate. I have shown in isolated, perfused liver experiments using the non-hyperpolarized [4-^{13}C]-monoethyl oxaloacetate that the compound is taken up by the liver, the ethyl ester group is cleaved, the C4 labeled oxaloacetate enters the TCA cycle, and is metabolized to produce maleate, citrate and aspartate, as expected. Dynamic nuclear polarization of [4-^{13}C]-monoethyl oxaloacetate sodium salt was successfully performed, however, the T_1 relaxation time of the ^{13}C label at the C4 position was only about 14s, not long enough to observe significant downstream real time metabolism in perfused liver with the hyperpolarized compound.

REFERENCES

1. Dale, B.M., M.A. Brown, and R.C. Semelka, Magnetic resonace imaging: Basic principles and applications. *Wiley,2015.*

2. Bloch, F., Nuclear induction. *Physical Review*, 1946. **70**(7-8): p. 460.

3. Purcell, E.M., H.C. Torrey, and R.V. Pound, Resonance absorption by nuclear magnetic moments in a solid. *Physical Review*, 1946. **69**(1-2): p. 37.

4. Aime, S., et al., High relaxivity contrast agents for MRI and molecular imaging, in molecular imaging. *Springer*,2005.p. 99-121.

5. Berger, A., Magnetic resonance imaging. *BMJ: British Medical Journal*, 2002. **324**(7328): p. 35-35.

6. Caravan, P., et al., Gadolinium(III) chelates as MRI contrast agents: structure, dynamics, and applications. *Chemical Reviews*, 1999. **99**(9): p. 2293-2352.

7. Abragam, A. and M. Goldman, Principles of dynamic nuclear polarisation. *Reports on Progress in Physics*, 1978. **41**(3): p. 395.

8. Griffin, R.G., Dynamic nuclear polarization at 9 T applied to solid state nuclear magnetic resonance. *Ecole Normale Supérieur de Lyon, 2000.*

9. Ardenkjær-Larsen, J.H., et al., Increase in signal-to-noise ratio of> 10,000 times in liquid-state NMR. *Proceedings of the National Academy of Sciences*, 2003. **100**(18): p. 10158-10163.

10. Hurd, R.E., et al., Hyperpolarized 13C metabolic imaging using dissolution dynamic nuclear polarization. *Journal of Magnetic Resonance Imaging*, 2012. **36**(6): p. 1314-1328.

11. Månsson, S., et al., 13C imaging—a new diagnostic platform. *European Radiology*, 2006. **16**(1): p. 57-67.

12. Golman, K., et al., Molecular imaging using hyperpolarized 13C. *The British journal of radiology*, 2003. **76**(suppl_2): p. S118-S127.

13. Caravan, P., et al., Gadolinium (III) chelates as MRI contrast agents: structure, dynamics, and applications. *Chemical Reviews*, 1999. **99**(9): p. 2293-2352.

14. Laurent, S., L. Vander Elst, and R. Muller, Lanthanide complexes for magnetic resonance and optical molecular imaging. *The Quarterly Journal of Nuclear Medicine and Molecular Imaging*, 2009. **53**(6): p. 586.

15. Toth, E., L. Helm, and A.E. Merbach, Relaxivity of gadolinium (III) complexes: theory and mechanism. *Wiley*, 2001.

16. Debroye, E. and T.N. Parac-Vogt, Towards polymetallic lanthanide complexes as dual contrast agents for magnetic resonance and optical imaging. *Chemical Society Reviews*, 2014. **43**(23): p. 8178-8192.

17. Sherry, A.D. and Y. Wu, The importance of water exchange rates in the design of responsive agents for MRI. *Current Opinion in Chemical Biology*, 2013. **17**(2): p. 167-174.

18. Westlund, P.-O., A generalized Solomon-Bloembergen-Morgan theory for arbitrary electron spin quantum number S: The dipole-dipole coupling between a nuclear spin I= 1/2 and an electron spin system S= 5/2. *Molecular Physics*, 1995. **85**(6): p. 1165-1178.

19. Aime, S., et al., Prototropic and water-exchange processes in aqueous solutions of Gd (III) chelates. *Accounts of Chemical Research*, 1999. **32**(11): p. 941-949.

20. Zhang, S., et al., 1H and 17O NMR detection of a lanthanide-bound water molecule at ambient temperatures in pure water as solvent. *Inorganic Chemistry*, 2001. **40**(17): p. 4284-4290.

21. Lauffer, R.B., Paramagnetic metal complexes as water proton relaxation agents for NMR imaging: theory and design. *Chemical Reviews*, 1987. **87**(5): p. 901-927.

22. Farrar, C.T., et al., Mechanism of dynamic nuclear polarization in high magnetic fields. *The Journal of Chemical Physics*, 2001. **114**(11): p. 4922-4933.

23. Viswanathan, S., et al., Alternatives to gadolinium-based metal chelates for magnetic resonance imaging .*Chemical Reviews*, 2010. **110**(5): p. 2960-3018.

24. Ren, J., et al., Analysis of lanthanide induced NMR shifts using a crystal field independent method: application to complexes of tetraazamacrocyclic ligands. *Inorganica Chimica Acta*, 2002. **339**: p. 273-282.

25. Webber, B.C. and M. Woods, Structural analysis of isomeric europium (III) chelates of NB-DOTMA. *Inorganic Chemistry*, 2012. **51**(15): p. 8576-8582.

26. Ratnakar, S.J., et al., Modulation of water exchange in europium (III) DOTA− tetraamide complexes via electronic substituent effects. *Journal of the American Chemical Society*, 2008. **130**(1): p. 6-7.

27. van Zijl, P. and N.N. Yadav, Chemical exchange saturation transfer (CEST): what is in a name and what isn't? *Magnetic Resonance in Medicine*, 2011. **65**(4): p. 927-948.

28. Vinogradov, E., A.D. Sherry, and R.E. Lenkinski, CEST: from basic principles to applications, challenges and opportunities. *Journal of Magnetic Resonance*, 2013. **229**: p. 155-172.

29. Zhang, S., et al., PARACEST agents: modulating MRI contrast via water proton exchange. *Accounts of Chemical Research*, 2003. **36**(10): p. 783-790.

30. Pedersen, M., Safety update on the possible causal relationship between gadolinium-containing MRI agents and nephrogenic systemic fibrosis. *Journal of Magnetic Resonance Imaging*, 2007. **25**(5): p. 881-883.

31. Brücher, E., et al., Stability and toxicity of contrast agents. *The Chemistry of Contrast Agents in Medical Magnetic Resonance Imaging, Second Edition*, 2013: p. 157-208.

32. Bunzli, J.-C.G. and C. Piguet, Taking advantage of luminescent lanthanide ions. *Chemical Society Reviews*, 2005. **34**(12): p. 1048-1077.

33. Bünzli, J.-C.G. and S.V. Eliseeva, Lanthanide NIR luminescence for telecommunications, bioanalyses and solar energy conversion. *Journal of Rare Earths*, 2010. **28**(6): p. 824-842.

34. Alpha, B., et al., Antenna effect in luminescent lanthanide cryptates: a photophysical study. *Photochemistry and Photobiology*, 1990. **52**(2): p. 299-306.

35. Bünzli, J.-C.G., Lanthanide luminescence for biomedical analyses and imaging. *Chemical Reviews*, 2010. **110**(5): p. 2729-2755.

36. Doffek, C., et al., Understanding the quenching effects of aromatic C–H- and C–D-oscillators in near-IR lanthanoid luminescence. *Journal of the American Chemical Society*, 2012. **134**(39): p. 16413-16423.

37. Zhang, J., et al., Sensitization of near-infrared-emitting lanthanide cations in solution by tropolonate ligands. *Angewandte Chemie International Edition*, 2005. **44**(17): p. 2508-2512.

38. Buenzli, J.-C.G., On the design of highly luminescent lanthanide complexes. *Coordination Chemistry Reviews*, 2015. **293**: p. 19-47.

39. Kobayashi, H., et al., Rational chemical design of the next generation of molecular imaging probes based on physics and biology: mixing modalities, colors and signals. *Chemical Society Reviews*, 2011. **40**(9): p. 4626-4648.

40. Ma, Y. and Y. Wang, Recent advances in the sensitized luminescence of organic europium complexes. *Coordination Chemistry Reviews*, 2010. **254**(9): p. 972-990.

41. Moeller, T., Coordination chemistry of the lanthanide elements—one hundred years of development and understanding. *American Chemical Socitey Publication,* 1967.

42. Rojas-Quijano, F.A., et al., Lanthanide (III) complexes of tris (amide) PCTA derivatives as potential bimodal magnetic resonance and optical imaging agents. *Chemistry-A European Journal*, 2009. **15**(47): p. 13188-13200.

43. Bonnet, C.S., et al., Pyridine-based lanthanide complexes combining MRI and NIR luminescence activities. *Chemistry-A European Journal*, 2012. **18**(5): p. 1419-1431.

44. Verwilst, P., et al., Recent advances in Gd-chelate based bimodal optical/MRI contrast agents. *Chemical Society Reviews*, 2015. **44**(7): p. 1791-1806.

45. Pauson, P.L., Tropones and tropolones. *Chemical Reviews*, 1955. **55**(1): p. 9-136.

46. Dutt, Y., R. Singh, and M. Katyal, Metal complexes with tropolones. *Talanta,* 1969. **16**(10): p. 1369-1382.

47. Zhang, J., et al., Synthesis and structural properties of lanthanide complexes formed with tropolonate ligands. *Inorganic Chemistry*, 2007. **46**(16): p. 6473-6482.

48. Beeby, A., et al., Non-radiative deactivation of the excited states of europium, terbium and ytterbium complexes by proximate energy-matched OH, NH and CH oscillators: an improved luminescence method for establishing solution hydration states. *Journal of the Chemical Society, Perkin Transactions 2,* 1999(3): p. 493-504.

49. Caillé, F., et al., Isoquinoline-based lanthanide complexes: bright NIR optical probes and efficient MRI agents. *Inorganic Chemistry*, 2012. **51**(4): p. 2522-2532.

50. Jagadish, B., et al., On the Synthesis of 1, 4, 7-Tris (tert-butoxycarbonylmethyl)-1, 4, 7, 10-tetraazacyclododecane. *Tetrahedron Letters,* 2011. **52**(17): p. 2058-2061.

51. Kovacs, Z. and A.D. Sherry, pH-controlled selective protection of polyaza macrocycles. *Synthesis*, 1997. **1997**(07): p. 759-763.

52. Martins, A.F., et al., Gd3+ complexes conjugated to Pittsburgh compound B: potential MRI markers of β-amyloid plaques. *Journal of Biological Inorganic Chemistry*, 2014. **19**(2): p. 281-295.

53. Micskei, K., et al., Oxygen-17 NMR study of water exchange on gadolinium polyaminopolyacetates [Gd(DTPA)(H2O)]2- and [Gd(DOTA)(H2O)]- related to NMR imaging. *Inorganic Chemistry*, 1993. **32**(18): p. 3844-3850.

54. CarmenáAlpoim, M. and F. Carlos, Determination of the number of inner-sphere water molecules in lanthanide (III) polyaminocarboxylate complexes. *Journal of the Chemical Society, Dalton Transactions*, 1992(3): p. 463-467.

55. Martins, A.F., et al., A bis (pyridine N-oxide) analogue of DOTA: relaxometric properties of the GdIII complex and efficient sensitization of visible and NIR-emitting lanthanide (III) cations including PrIII and HoIII. *Chemistry-A European Journal*, 2014. **20**(45): p. 14834-14845.

56. Aime, S., et al., Conformational and coordination equilibria on DOTA complexes of lanthanide metal ions in aqueous solution studied by 1H-NMR spectroscopy. *Inorganic. Chemistry*, 1997. **36**(10): p. 2059-2068.

57. Carnall, W., P. Fields, and K. Rajnak, Electronic energy levels in the trivalent lanthanide aquo ions. I. Pr^{3+}, Nd^{3+}, Pm^{3+}, Sm^{3+}, Dy^{3+}, Ho^{3+}, Er^{3+}, and Tm^{3+}. *The Journal of Chemical Physics*, 1968. **49**(10): p. 4424-4442.

58. Bünzli, J.-C.G. and S.V. Eliseeva, Intriguing aspects of lanthanide luminescence. *Chemical Science*, 2013. **4**(5): p. 1939-1949.

59. Peters, J., J. Huskens, and D. Raber, Lanthanide induced shifts and relaxation rate enhancements. *Progress in Nuclear Magnetic Resonance Spectroscopy*, 1996. **28**(3-4): p. 283-350.

60. Rohrer, M., et al., Comparison of magnetic properties of MRI contrast media solutions at different magnetic field strengths. *Investigative Radiology*, 2005. **40**(11): p. 715-724.

61. Ruloff, R., et al., Accelerating water exchange for Gd III chelates by steric compression around the water binding site. *Chemical Communications*, 2002(22): p. 2630-2631.

62. Rudovský, J., et al., Synthesis of a bifunctional monophosphinic acid DOTA analogue ligand and its lanthanide (III) complexes. A gadolinium (III) complex endowed with an optimal water exchange rate for MRI applications. *Organic & Biomolecular Chemistry*, 2005. **3**(1): p. 112-117.

63. Kálmán, F.K., et al., Synthesis, potentiometric, kinetic, and NMR Studies of 1, 4, 7, 10-tetraazacyclododecane-1, 7-bis (acetic acid)-4, 10-bis (methylenephosphonic acid)(DO2A2P) and its complexes with Ca (II), Cu (II), Zn (II) and lanthanide (III) ions. *Inorganic Chemistry*, 2008. **47**(9): p. 3851-3862.

64. Rojas-Quijano, F.A., et al., Synthesis and characterization of a hypoxia-sensitive MRI probe. *Chemistry-A European Journal*, 2012. **18**(31): p. 9669-9676.

65. Bleuzen, A., et al., Water exchange on in aqueous magnesium (II) solution: a variable temperature and pressure 17O NMR study. *Magnetic Resonance in Chemistry*, 1997. **35**: p. 765È773.

66. Djanashvili, K. and J. Peters, How to determine the number of inner-sphere water molecules in Lanthanide (III) complexes by 17O NMR spectroscopy. A technical note. *Contrast Media & Molecular Imaging*, 2007. **2**(2): p. 67-71.

67. Rudovský, J., et al., Lanthanide (III) complexes of a mono (methylphosphonate) analogue of H4dota: The influence of protonation of the phosphonate moiety on the TSAP/SAP isomer ratio and the water exchange rate. *Chemistry-A European Journal*, 2005. **11**(8): p. 2373-2384.

68. Fasano, M., et al., The extraordinary ligand binding properties of human serum albumin. *International Union of Biochemistry and Molecular Biology life*, 2005. **57**(12): p. 787-796.

69. Caravan, P., et al., Albumin binding, relaxivity, and water exchange kinetics of the diastereoisomers of MS-325, a gadolinium (III)-based magnetic resonance angiography contrast agent. *Inorganic Chemistry*, 2007. **46**(16): p. 6632-6639.

70. Grist, T.M., et al., Steady-state and dynamic MR angiography with MS-325: initial experience in humans. *Radiology*, 1998. **207**(2): p. 539-544.

71. Caravan, P., et al., The interaction of MS-325 with human serum albumin and its effect on proton relaxation rates. *Journal of the American Chemical Society*, 2002. **124**(12): p. 3152-3162.

72. Lauffer, R.B., et al., MS-325: albumin-targeted contrast agent for MR angiography. *Radiology*, 1998. **207**(2): p. 529-538.

73. Beeby, A., et al., AS d. Sousa, JAG Williams and M. Woods. Intramolecular sensitisation of lanthanide(III) luminescence by acetophenone-containing ligands: the critical effect of para-substituents and solvent. *Journal of the Chemical Society, Perkin Transactions*, 1999. **2**(2): p. 493.

74. Hurd, R.E., et al., Metabolic imaging in the anesthetized rat brain using hyperpolarized [1-13C] pyruvate and [1-13C] ethyl pyruvate. *Magnetic Resonance in Medicine*, 2010. **63**(5): p. 1137-43.

75. Aime, S. and P. Caravan, Biodistribution of gadolinium-based contrast agents, including gadolinium deposition. *Journal of Magnetic Resonance Imaging*, 2009. **30**(6): p. 1259-1267.

76. Caillé, F., et al., Isoquinoline-based lanthanide complexes: bright NIR optical probes and efficient MRI agents. *Inorganic Chemistry*, 2012. **51**(4): p. 2522-2532.

77. Krumpel, A.H., Locating energy levels of lanthanide ions in inorganic ionic compounds. *PhD Thesis, Technical University Delft, Netherlands*, 2009.

78. Ishida, H., J.-C. Bünzli, and A. Beeby, Guidelines for measurement of luminescence spectra and quantum yields of inorganic and organometallic compounds in solution and solid state (IUPAC Technical Report). *Pure and Applied Chemistry.*, 2016. **88**(7): p. 701-711.

79. Kuhn, L.T., Hyperpolarization methods in NMR spectroscopy. *Springer.* 2013.

80. Overhauser, A.W., Polarization of nuclei in metals. *Physical Review*, 1953. **92**(2): p. 411.

81. Carver, T.R. and C.P. Slichter, Experimental Verification of the Overhauser Nuclear Polarization Effect. *Physical Review*, 1956. **102**(4): p. 975-980.

82. Abragam, A., Overhauser effect in nonmetals. *Physical Review*, 1955. **98**(6): p. 1729-1735.

83. Ramanathan, C., Dynamic nuclear polarization and spin diffusion in nonconducting solids. *Applied Magnetic Resonance*, 2008. **34**(3): p. 409.

84. Ardenkjær-Larsen, J.H., et al., Increase in signal-to-noise ratio of > 10,000 times in liquid-state NMR. *Proceedings of the National Academy of Sciences*, 2003. **100**(18): p. 10158-10163.

85. Lumata, L., et al., BDPA: An efficient polarizing agent for fast dissolution dynamic nuclear polarization NMR spectroscopy. *Chemistry – A European Journal*, 2011. **17**(39): p. 10825-10827.

86. Gerfen, G.J., et al., High frequency (140 GHz) dynamic nuclear polarization: polarization transfer to a solute in frozen aqueous solution. *The Journal of Chemical Physics*, 1995. **102**(24): p. 9494-9497.

87. Goldman, M., Thermal mixing between spin systems in solids. *Physical Review*, 1965. **138**(6A): p. A1668-A1674.

88. Goertz, S.T., The dynamic nuclear polarization process. *Nuclear Instruments and Methods in Physics Research Section A: Accelerators, Spectrometers, Detectors and Associated Equipment*, 2004. **526**(1): p. 28-42.

89. Lumata, L., et al., DNP by thermal mixing under optimized conditions yields >60 000-fold enhancement of 89Y NMR signal. *Journal of the American Chemical Society*, 2011. **133**(22): p. 8673-8680.

90. Wenckebach, W.T., Dynamic nuclear polarization via thermal mixing: beyond the high temperature approximation. *Journal of Magnetic Resonance*, 2017. **277**(supplement C): p. 68-78.

91. Thurber, K.R. and R. Tycko, Theory for cross effect dynamic nuclear polarization under magic-angle spinning in solid state nuclear magnetic resonance: The importance of level crossings. *The Journal of Chemical Physics*, 2012. **137**(8): p. 084508.

92. Golman, K., et al., Molecular imaging with endogenous substances. *Proceedings of the National Academy of Sciences*, 2003. **100**(18): p. 10435-10439.

93. Golman, K. and J.S. Petersson, metabolic imaging and other applications of hyperpolarized 13C1. *Academic Radiology*, 2006. **13**(8): p. 932-942.

94. Merritt, M.E., et al., Hyperpolarized 13C allows a direct measure of flux through a single enzyme-catalyzed step by NMR. *Proceedings of the National Academy of Sciences*, 2007. **104**(50): p. 19773-19777.

95. Gallagher, F.A., M.I. Kettunen, and K.M. Brindle, Biomedical applications of hyperpolarized 13C magnetic resonance imaging. *Progress in Nuclear Magnetic Resonance Spectroscopy*, 2009. **55**(4): p. 285-295.

96. Serrao, E.M. and K.M. Brindle, Potential clinical roles for metabolic imaging with hyperpolarized [1-(13)C]pyruvate. *Frontiers in Oncology*, 2016. **6**: p. 59.

97. Golman, K., et al., Metabolic imaging by hyperpolarized 13C magnetic resonance imaging for *in vivo* tumor diagnosis. *Cancer Research*, 2006. **66**(22): p. 10855-10860.

98. Golman, K., et al., Metabolic imaging by hyperpolarized magnetic resonance imaging for tumor diagnosis. *Cancer Research*, 2006. **66**(22): p. 10855.

99. Nelson, S.J., et al., Metabolic imaging of patients with prostate cancer using hyperpolarized [13C]Pyruvate. *Science Translational Medicine*, 2013. **5**(198): p. 198.

100. Bhattacharya, P., B.D. Ross, and R. Bünger, Cardiovascular applications of hyperpolarized contrast media and metabolic tracers. *Experimental Biology and Medicine*, 2009. **234**(12): p. 1395-1416.

101. Harrison, C., et al., Comparison of kinetic models for analysis of pyruvate-to-lactate exchange by hyperpolarized (13)C NMR. *NMR in Biomedicine*, 2012. **25**(11): p. 1286-1294.

102. Lumata, L.L., et al., Development and performance of a 129-GHz dynamic nuclear polarizer in an ultra-wide bore superconducting magnet. *Magnetic Resonance Materials in Physics, Biology and Medicine*, 2015. **28**(2): p. 195-205.

103. Sherry, A.D. and C.R. Malloy, 13C Isotopomer analysis of glutamate a NMR method to probe metabolic pathways intersecting in the citric acid cycle, in vivo carbon-13 NMR 2002, *Springer* US: Boston, MA. p. 59-97.

104. Lu, D., et al., 13C NMR isotopomer analysis reveals a connection between pyruvate cycling and glucose-stimulated insulin secretion (GSIS). *Proceedings of the National Academy of Sciences*, 2002. **99**(5): p. 2708-2713.

105. Puccetti, C., et al., 13C-NMR isotopomer distribution analysis: a method for measuring metabolic fluxes in condensation biosynthesis. *NMR in Biomedicine*, 2002. **15**(6): p. 404-415.

106. Golman, K., et al., 13C-angiography .*Academic Radiology*. 2002. **9 Suppl 2**: p. S507-10.

107. Moreno, K.X., et al., Competition of pyruvate with physiological substrates for oxidation by the heart: implications for studies with hyperpolarized [1-(13)C]pyruvate. *American Journal of Physiology - Heart and Circulatory Physiology*, 2010. **298**(5): p. H1556-H1564.

108. Merritt, M.E., et al., Flux through hepatic pyruvate carboxylase and phosphoenolpyruvate carboxykinase detected by hyperpolarized 13C magnetic resonance. *Proceedings of the National Academy of Sciences*, 2011. **108**(47): p. 19084-19089.

109. Golman, K. and M. Thaning, Real-time metabolic imaging. *Proceedings of the National Academy of Sciences*, 2006. **103**(30): p. 11270-11275.

110. Jin, E.S., A.D. Sherry, and C.R. Malloy, Metabolism of glycerol, glucose, and lactate in the citric acid cycle prior to incorporation into hepatic acylglycerols. *Journal of Biological Chemistry*, 2013. **288**(20): p. 14488-14496.

111. Jones, J.G., et al., Measurement of gluconeogenesis and pyruvate recycling in the rat liver: a simple analysis of glucose and glutamate isotopomers during metabolism of [1,2,3-13C3]propionate. *Federation of European Biochemical Societies L*etters., 1997. **412**(1): p. 131-137.

112. Rines, A.K., et al., Targeting hepatic glucose metabolism in the treatment of type 2 diabetes. *Nature Reviews Drug Discovery* ,2016. **15**(11): p. 786-804.

113. Nuttall, F.Q., A. Ngo, and M.C. Gannon, Regulation of hepatic glucose production and the role of gluconeogenesis in humans: is the rate of gluconeogenesis constant? *Diabetes/Metabolism Research and Reviews*, 2008. **24**(6): p. 438-458.

114. Hanson, R.W. and L. Reshef, Regulation of phosphoenolpyruvate carboxykinase (GTP) gene expression. *Annual Review of Biochemistry*, 1997. **66**(1): p. 581-611.

115. Hanson, R.W. and A.J. Garber, Phosphoenolpyruvate carboxykinase. I. Its role in gluconeogenesis. *The American Journal of Clinical Nutrition*, 1972. **25**(10): p. 1010-21.

116. Pajor, A.M., Sodium-coupled transporters for Krebs cycle intermediates. *Annual Review of Physiology*, 1999. **61**: p. 663-82.

117. Halestrap, A.P., The monocarboxylate transporter family--Structure and functional characterization. *International Union of Biochemistry and Molecular Biology life*, 2012. **64**(1): p. 1-9.

118. Halestrap, A.P. and N.T. Price, The proton-linked monocarboxylate transporter (MCT) family: structure, function and regulation. *Biochemical Journal*, 1999. **343**(Pt 2): p. 281-299.

119. Jackson, V.N. and A.P. Halestrap, The kinetics, substrate, and inhibitor specificity of the monocarboxylate (lactate) transporter of rat liver cells determined using the fluorescent intracellular pH indicator, 2′, 7′-bis (carboxyethyl)-5 (6)-carboxyfluorescein. *Journal of Biological Chemistry*, 1996. **271**(2): p. 861-868.

120. Jensen, P.R., et al., Hyperpolarized [1,3-13C2]ethyl acetoacetate is a novel diagnostic metabolic marker of liver cancer. *International Journal of Cancer*, 2015. **136**(4): p. E117-26.

121. Zacharias, N.M., et al., Real-time molecular imaging of tricarboxylic acid cycle metabolism *in vivo* by hyperpolarized 1-13C diethyl succinate. *Journal of the American Chemical Society*, 2012. **134**(2): p. 934-943.

122. Laizure, S.C., et al., The role of human carboxylesterases in drug metabolism: have we overlooked their importance? *Pharmacotherapy*, 2013. **33**(2): p. 210-22.

123. Moreno, K.X., et al., Production of hyperpolarized (13)CO(2) from [1-(13)C]pyruvate in perfused liver does reflect total anaplerosis but is not a reliable biomarker of glucose production. *Metabolomics : Official Journal of the Metabolomic Society*, 2015. **11**(5): p. 1144-1156.

124. Hellerman, L., et al., Studies on succinate dehydrogenase. effect of monoethyl oxaloacetate, acetylene dicarboxylate, and thyroxine. *Journal of Biological Chemistry*, 1960. **235**(8): p. 2468-2474.

125. Cocivera, M., et al., Catalysis of keto-enol tautomerism of oxaloacetic acid and its ions studied by proton nuclear magnetic resonance. *The Journal of Organic Chemistry*, 1977. **42**(25): p. 4076-4080.

126. Hashami, Z., et al., Lanthanide DO3A-tropone complexes: efficient dual MR/NIR imaging probes in aqueous medium. *European Journal of Inorganic Chemistry*, 2017. **2017**(43): p. 4965-4968.

127. Jiang, W., et al., Hyperpolarized 15N-pyridine derivatives as pH-sensitive MRI agents. *Scientific Reports*, 2015. **5**.

128. Gupton, B., F., et al., Preparation of sodium diethyl oxalacetate. *US 4,902,819*, 1990.

BIOGRAPHICAL SKETCH

Zohreh Hashami was born in Iran. She obtained her bachelor’s degree in Physics from Azad University of Mashhad, Iran. She was accepted into the Physics graduate program at The University of Texas at Dallas in Fall 2009 and earned her master degree in Physics 2011. In 2013 she entered the Chemistry department to pursue a PhD in Chemistry. In 2013 she started working under the supervision of Dr. Zoltan Kovacs at UT Southwestern Medical Research center. Her research focused on development of novel magnetic resonance probes.

CURRICULUM VITAE

Zohreh Hashami

EDUCATION

PhD. in Chemistry/ Biochemistry

University of Texas at Dallas /UT Southwestern Medical Research Center, USA

M.S. in Physics
University of Texas at Dallas, USA

B.S. in Physics
Azad University of Mashhad, Iran

M.S. LAB EXPERINCE

Advance Imaging Research Center (AIRC), UT Southwestern* Medical Research Center & *Chemistry Department, University of Texas at Dallas

- Design and develop bimodal, MR/optical imaging agents, dynamic nuclear polarization (DNP), data analysis: ACD (Advanced Chemistry Development) and Igor. (Image processing).

***Physics Department, University of Texas at Dallas*:**

- Synthesized, analyzed and characterized carbon nanotubes

TEACHING EXPERIENCE

- **Adjunct faculty**
  Brookhaven Community College, Farmers Branch, TX *2012 – Present*
  University physics I& II, physical chemistry, College physics I&II and astronomy

- **Adjunct faculty** *Present*
  Collin County Community College
  University physics II, College physics II

- **Adjunct faculty**
  Richland Community College, Dallas, TX *2014-2015*
  College physics I&II

- **Teaching Assistant**
  University of Texas at Dallas *2010-2011&2013-Present*
  University physics I&II, statistical physics and General chemistry I&II

AWARDS

Recognition of Service from University of Texas at Dallas *2016*
Honor Society, Strength and Honor member *2013- Present*

PUBLICATIONS

1) **Zohreh Hashami**, Andre F. Martins, Alexander M. Funk, Veronica Clavijo Jordan,Svetlana V. Eliseeva, and Zoltan Kovacs, Lanthanide DO3A-tropolone complexes: efficient bimodal MR/NIR imaging probes in water, *Eur. J. Inorg. Chem***. 2017**, 4963.

2) Lloyd Lumata, Matthew Merritt, **Zohreh Hashami**, S. James Ratnakar, and Zoltan Kovacs, Production and NMR Characterization of Hyperpolarized 107,109Ag Complexes, *Angew. Chem. Int. Ed.* **2011**, 525–527